DISSOCIATION OF MOLECULES ON SILICON SURFACES STUDIED BY SCANNING TUNNELING MICROSCOPY

Pouya Maraghechi

B.Sc. Physics, Shahid Beheshty University, Tehran, Iran, 2004

A thesis
Submitted to the school of Graduate Studies
of the University of Lethbridge
in partial fulfillment of the
requirement for the degree

MASTER OF SCIENCE

Department of Physics
University of Lethbridge
LETHBRIDGE, ALBERTA, CANADA

Dedication

I dedicate this work to my parents, who offered me unconditional love and support throughout my studies though they were miles away.

Abstract

Dissociation of trichloroethylene (TCE) molecules on the Si(111)-7x7 and the Si(100)-2x1 surfaces was studied using STM. Though molecular adsorption may also be observed on the Si(111)-7x7 surface, dissociation is the dominant process. From the STM images acquired, products of dissociation were identified, namely chlorine atoms and dichlorovinyl groups. Dissociation of chlorine from the TCE molecule was confirmed by studying not just appearance in STM images but also from studies of tip-induced diffusion. Different binding configurations were proposed for the vinyl group on the Si (111)-7x7 and the Si(100)-2x1 surfaces. Site preference for each product of dissociation is reported on the Si(111)-7x7 surface. Dissociation of molecules such as ammonia, dimethylamine and methyl chloride on the Si(111)-7x7 and Si(100)-2x1 surfaces is reviewed. The field emission process is explained in detail. The usefulness of making field emission measurements is in evaluating the sharpness of STM tips.

Acknowledgements

I would like to acknowledge the support of the University of Lethbridge for providing funding and work while completing my program. I am eternally grateful for the support of my committee, Dr. Adriana Predoi-Cross and Dr. Peter Dibble for giving ideas, support, and listening to my progress reports. I thank my supervisor Dr. Steve Patitsas for taking me into his lab and supervising me as a graduate student. I thank him for his instruction, his ideas, support, and interesting discussions. I would also like to acknowledge Steven Horn who designed the new STM head.

I thank my Ph.D. supervisor Dr. Abdulhakem Elezzabi for supporting me although I was working on my Master's thesis while I was enrolled in his lab. I would like to thank Michael Quong for his help in correcting grammatical problems in my thesis.

I thank my peers in the lab Steven Horn and Weiming Liu for interesting discussions and making my experience more fun throughout this program. They would always lend me a hand if I asked and I am grateful for their help.

I would like to thank Mehdi Ahoonmanesh who helped me through some difficulties and made my life in Lethbridge fun. I would also thank Sahar Kolahi for her support all through my graduate studies.

Table of Contents

List of Tables

List of Figures

List of Abbreviations

AES	Auger Electron Spectroscopy
AFM	Atomic Force Microscopy
CITS	Current Imaging Tunneling Spectroscopy
CT	Charge Transfer
DAS	Dimer Adatom Stacking-Fault
DMA	Dimethylamine
EELS	Energy Electron Loss Spectroscopy
FN	Fowler Nordheim
ISS	Ion- Scattering Spectroscopy
LDS	Local Density of States
NEXAFS	Near Edge X-ray Absorption Fine Structure
PCE	Perchloroethylene
RCA	Trademark used by Thomson SA
RT	Room Temperature
STM	Scanning Tunneling Microscopy
TCE	Trichloroethylene
TDS	Temperature Desorption Spectroscopy
TSP	Titanium Sublimation Pump
UHV	Ultra High Vacuum
UPS	UV ray Photoelectron Spectroscopy

XPS	X-ray Photoelectron Spectroscopy

Chapter 1

Introduction

The Scanning Tunneling Microscope (STM) was invented in 1981 by Gerd Binnig and Heinrich Rohrer at the IBM Zurich Research Center. They obtained for the first time the real-space images of atomic structures of the surface (determining the atomic structure of Si(111)7x7) using STM in 1982 [1]. In 1986, they received the Nobel Prize for their invention of STM.

The STM is a non-optical, electron-based microscope which employs the principles of quantum mechanics. The basic principle of STM is based on the tunneling current between a sharp metallic tip and a conducting material through the vacuum barrier when a bias is applied between the tip and the sample. The distance between the tip and sample surface is about an atom diameter. The magnitude of the tunneling current is exponentially dependent on the distance between probe and the surface [2].

A representative schematic of an STM system is shown in Figure (1-1). During normal operation, the tunneling current is held constant through the use of a feedback circuit and a piezoelectric actuator. The set point value for the current is determined by the user. Once a stable tunnel junction is achieved, the tip is raster scanned over the surface by the use of the same piezoelectric actuator. In this constant-current mode it is the feedback signal that is monitored and displayed in the form of a grey-scale image, sometimes referred to as a topograph. This image contains information about the geometry and

electronic structure of the surface, revealing the real-space information about the surface of matter.

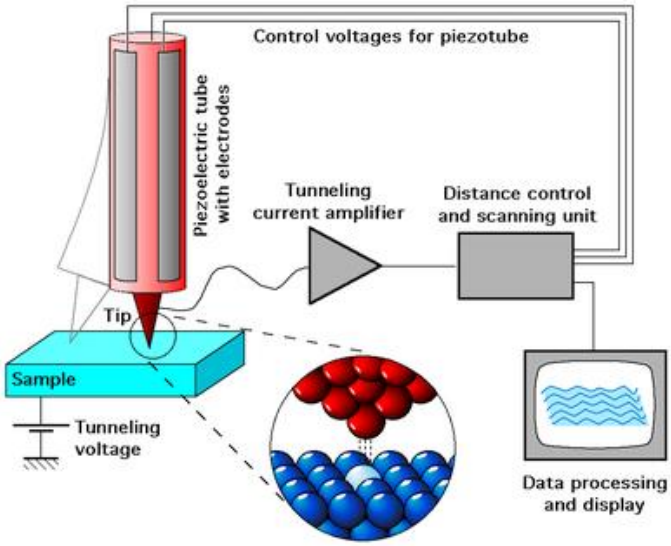

Figure 1-1 Schematic view of an STM (Figure was taken from Ref. [3])

STM can also be used as a tool to manipulate atoms and molecules on surfaces. The STM manipulations can be performed by precisely controlling the tip-sample interactions. This can be done by using tunneling electrons, or the electric field between the tip and sample. The STM-tip can be used as an engineering or analytical tool, to fabricate artificial atomic-scale structures, probe novel quantum phenomena, and study properties of single atoms and molecules at an atomic level [4].

In addition to manipulating atoms, the charge-density-wave (CDW) can be studied using STM [5, 6]. STM is a promising tool for controlling the layer-by-layer growth method for the construction of high T_c superconducting artificial lattices and super-

conducting / ferromagnetic superlattices as well. The electronic state of carrier doped strongly correlated electronic systems are also investigated (by performing Scanning Tunneling Spectroscopy) using STM [7, 8].

The study of surfaces is an important part of physics, with particular applications in semiconductor physics and microelectronics. STM imaging has greatly contributed to surface science and the semiconductor industry. Using STM, for example, atomic structure of surfaces of Si(111)-2x1 [9], Ge(111)-2x1 [10], Au(110) [11], Au(111) [12] and many others have been observed with atomic resolution.

In chemistry, surface reactions also play an important part, for example in catalysis. The STM works best with conducting materials, but it is also possible to fix organic molecules on a surface and study their structures. For example, this technique has been used in the study of DNA molecules [13].

1.1 Tunneling Current

An energy level diagram for the tunnel junction formed by the Si(111)-7x7 surface and a tungsten tip is shown in Figure (1-2). The Si(111)-7x7 surface is specifically used here to provide a concrete example. Much of what is described here can still be applied for the more general case of the surface of a semiconductor as there will still be a bulk band gap and various surface states, both below and above the Fermi level and sometimes at the Fermi level as is the case here.

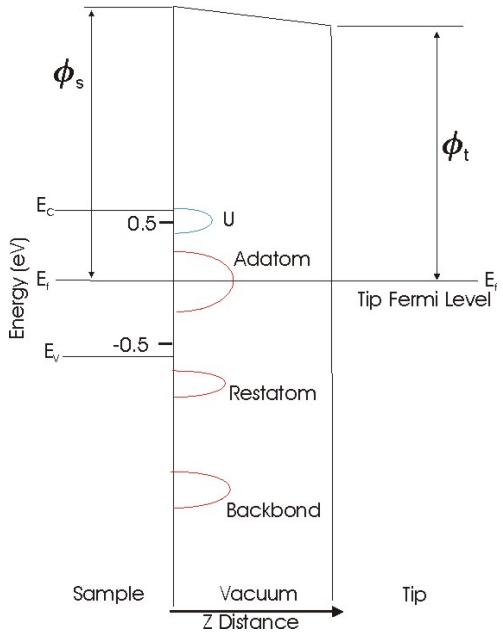

Figure 1-2 The energy level diagram for the surface states on the Si(111)-7x7 surface and tungsten tip while there is no voltage applied to the sample. The Fermi energy level E_f, Conduction band edge E_C and Valence band E_V are shown. Surface states U, adatom, restatom and backbond shown. The data used for this diagram are from[14]

As will be discussed later in chapters 3 and 5, surface electron states on Si(111)-7x7 are located on adatoms, the rest atoms and on backbonds. The energies of these states are indicated in Figure (1-2). The U-state and a part of the adatom state are in the unoccupied part of the spectrum. The other part of adatom and the restatom and backbond states are in the occupied part. In Figure (1-2), φ_s and φ_t are the silicon and the tip work functions respectively and E_c and E_v are the silicon's conduction band and valence band respectively. Figure (1-2) is shown for the condition where there is no bias

between the tip and the surface. In this case the Fermi level of the sample and the tip line up, resulting in no net tunneling current. Figure (1-3) shows the condition when the sample bias is -0.5 V.

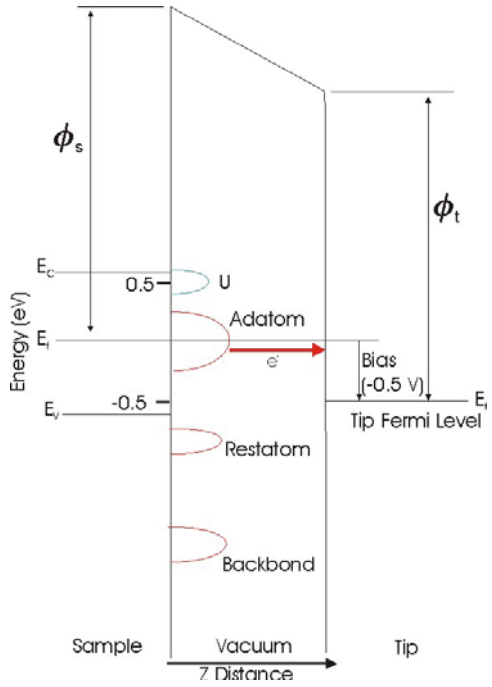

Figure 1-3 The energy level diagram for the surface states on the Si(111)-7x7 surface and tungsten tip while -0.5 V is applied to the sample. The arrow indicates the tunneling current from the filled surface states to the empty states of the tip.

The case in which the Fermi level of the sample is raised by 0.5 V relative to the tip Fermi level is shown in Figure (1-3). The electrons from the filled sample states from E_f – e|V| to E_f can now tunnel into the empty states of the tip (the red arrow indicates the tunneling current). In this case (-0.5 V sample bias) electrons from the sample contribute

to the tunneling current. Figure (1-4) shows the condition when the sample bias is +0.5 V.

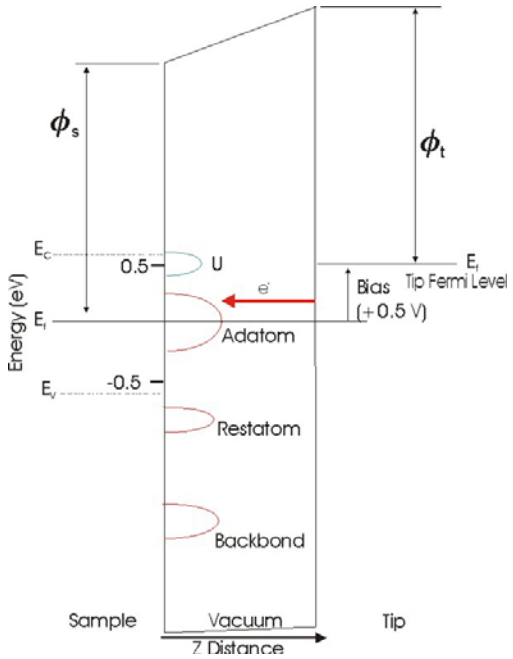

Figure 1-4 The energy level diagram for the surface states on the Si(111)-7x7 surface and tungsten tip while +0.5 V is applied to the sample. The arrow indicates the tunneling current from the filled tip states to the empty states of the surface.

The case in which the Fermi level of the sample is lowered by 0.5 V relative to the tip Fermi level is shown in Figure (1-4). The electrons from the tip from $E_f - e|V|$ to E_f can now tunnel into the empty states of the sample in the energy range from E_f to $E_f + e|V|$ (the red arrow indicates the tunneling current). In this case (+0.5 V sample bias) electrons from the tip contribute to the tunneling current.

The tunneling current can be approximated as [15]

$$I \propto \int_0^{eV} \rho_s\left(E_f - E\right) T\left(E,V\right) \rho_t\left(E_f - E + eV\right) dE \tag{1.1}$$

where V is the sample bias and T(E,V) is the barrier transmission coefficient of tunneling of electrons between the tip and the sample and ρ_s and ρ_t are the local density of states of the sample and the tip respectively. The barrier transmission coefficient can be written as

$$T\left(E,V\right) = \exp\left(-2\kappa z\right) \tag{1.2}$$

where

$$\kappa = \left[k_{\|}^{\,2} + \frac{2m\bar{\phi}}{\hbar^2} \right]^{\frac{1}{2}} \tag{1.3}$$

is the decay constant and z is the separation between the tip and sample surface and $\bar{\phi} = \left(\phi_s + \phi_t\right)/2 + E - e\,|V|\,/2$, is the averaged barrier height between the tip and the sample.

From equation (1.1) it can be seen that the tunneling current is a probe of both the sample and the tip density of states. It is assumed that the tip wave function is an s-wave (constant density of states) as discussed by Tersoff and Hamann [16, 17]. By this assumption ρ_t can be removed from the integral in equation (1.1) and one can write

$$I \propto \int_0^{eV} \rho_s\left(E_f - E\right) T\left(E,V\right) dE \tag{1.4}$$

Equation (1.4) indicates that the tunneling current probes the sample surface density of states.

In the case of $k_{\|} = 0$ and minimum E for the tunneling electrons, T(E,V), the transmission coefficient is maximum. From equation (1.2) with these conditions one will have

$$T_{\max} = \exp\left\{-2z\left[\frac{2m}{\hbar^2}\left(\left(\phi_s + \phi_t\right)/2 - \frac{e|V|}{2}\right)^{\frac{1}{2}}\right]\right\} \tag{1.5}$$

By this assumption T(E,V) in equation (1.4) can be taken out of integral and for the tunneling current one will have

$$I \propto T_{\max} \int_0^{eV} \rho_s\left(E_f - E\right) dE \tag{1.6}$$

STM images are formed by the contours of constant current. Equation (1.6) indicates that these contours of constant current are the contours of constant integrated density of states between E_f and $E_f - e|V|$ at the surface of the sample [14].

At negative sample bias the STM images will show high points at the location of the occupied surface states of the sample between E_f and $E_f - e|V|$ (see Figure (1-3)). At positive sample bias the STM images will show high points at the location of the unoccupied surface states of the sample between E_f and $E_f + e|V|$ (see Figure (1-4)).

1.2 UHV Chamber and STM System

The STM is placed in an ultra high vacuum (UHV) vacuum chamber with the base pressure better than $3x10^{-11}$ Torr. The UHV chamber in the Surface Science Laboratory in the Physics Department at the University of Lethbridge is shown in Figure (1-5). The turbo pump and ionization pump are indicated in this figure.

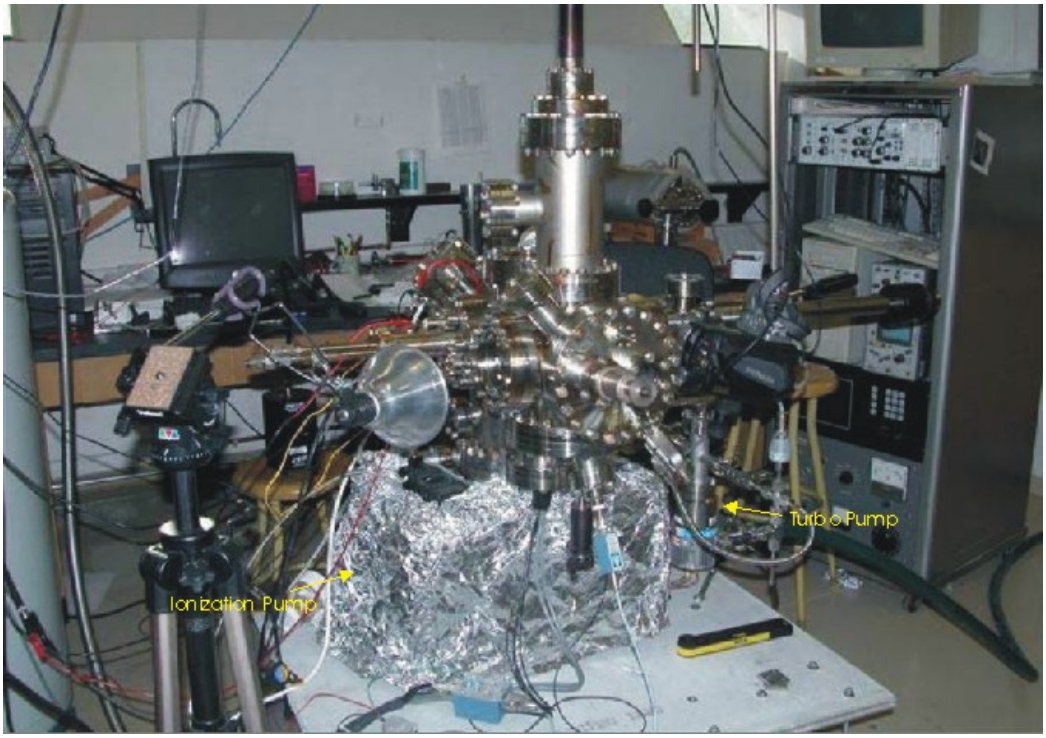

Figure 1-5 The UHV chamber at Surface Science Laboratory at University of Lethbridge

A detailed discussion on the UHV system is given in section 5.1. The chamber rests on a vibration isolation platform which in turns sits on a bed of sand. The STM head used to produce the images is suspended with a magnetically damped spring system inside the

vacuum chamber. The head is a home built unit based on the Besocke-style design for the coarse approach mechanism. More detail on the STM head can be found in Ref. [18].

1.3 Thesis Project

The main goal of this thesis was to study the basic physical process of dissociation of molecules at surfaces. For a given molecule one can ask many basic questions: Will the molecule dissociate?, What will the products be?, How reactive are the products?, How is energy distributed among the products? How does temperature affect all of the previous questions?, etc.

Some more particular questions concerning dissociation on surfaces that can be answered only by STM (or its sister technique Atomic Force Microscopy, AFM) are: i) How far apart do dissociation products wind up from each other? ii) Do different products have different site preferences? iii) Do some products leave the surface? iv) What role do defects play in surface catalysis? v) Does an adsorption/dissociation process affect subsequent nearby events?

The clean silicon (111) and (100) surfaces were chosen as substrates for these studies because they are very well understood. It makes perfect sense to study the dissociation of a molecule not previously studied on a well-understood substrate.

In the second chapter, the preparation and cleaning procedure for STM tips and the field emission phenomenon is explained. Using field emission, a procedure for testing the sharpness of the tip is explained.

In the third chapter the atomic and electronic structure of the Si(111)-7x7 surface is explained. The interaction of chlorine with this surface is reviewed.

In the fourth chapter the dissociation of ammonia, dimethylamine and trichloroethylene on the Si(111)-7x7 surface using different surface science techniques is reviewed.

In the fifth chapter, a detailed experimental procedure that has resulted in producing low defect Si(111)-7x7 surfaces is discussed. The dissociation of trichloroethylene on Si(111)-7x7 studied by STM at the Surface Science Laboratory at the University of Lethbridge is discussed. The products of dissociation are identified. Different types of binding configurations for the dissociated group and molecular adsorption are proposed.

In the sixth chapter the atomic and electronic structure of Si(100)-2x1 is explained. The dissociation of ammonia, methyl chloride and perchloroethylene on this surface using different surface science techniques is reviewed.

In the seventh chapter a detailed procedure that resulted in producing low defect Si(100)-2x1 surfaces is explained. The dissociation of TCE on the Si(100)-2x1 surface studied by STM which was performed at the Surface Science Laboratory at the University of Lethbridge is discussed. The products of dissociation are identified. From the STM images, different models for the various types of binding configurations are proposed.

The eighth chapter is the conclusion, summary and future plans.

Appendix A explains the Fermi-Dirac distribution.

Appendix B provides a brief summary of selected surface science measurement techniques (and acronyms).

Chapter 2

STM Tip Preparation

Scanning Tunneling Microscopy (STM) experiments require very sharp and clean tips to obtain high quality images, in order to resolve features at the atomic scale on surfaces. Sometimes the tips that are prepared are not sharp enough to provide an acceptable resolution for conducting surface studies. STM experiments are a time consuming process and generally it is good practice to assess the sharpness of the tips that are produced before performing experiments. In this chapter the procedure of fabricating STM tips from tungsten wire is explained. For testing the tip sharpness, the field emission technique is used. With careful monitoring of field emission currents the sharpness of a tip can be determined approximately. The relationship between the field emission current and tip sharpness is discussed in this chapter.

2.1 Preparing STM Tips

The STM tips are prepared from a 0.001 inch diameter polycrystalline tungsten wire by electrochemical etching. For the tip to form, the wire was shielded with Teflon tubing except for a small slit (~2 mm) that was exposed to the etching solution. The tip is formed at this spot after the wire is submerged in a 5 M solution of NaOH and connected to a +6.2 V potential (anode). For the cathode, a stainless steel wire is submerged in the solution near the tungsten wire. The reactions at anode and cathode are as follows [19]:

cathode: $6H_2O + 6e^- \rightarrow 3H_{2(g)} + 6OH^-$

anode: $W_{(s)} + 8OH^- \rightarrow WO_4^{2-} + 4H_2O + 6e^-$

It can be seen that at the anode, tungsten undergoes an oxidative dissolution of W to WO_4^2, which is soluble in water. Because of this the wire is etched at the contact areas with the solution. By the etching process the wire gets thinner and thinner until the neck can not support the weight and the bottom part drops off. This process results in sharp tips suitable for STM experiments.

After the tip is dropped at the bottom of the beaker, it is cleaned with purified water and mounted in the tip holder as shown in Figure (2-1). After mounting, the tips are transferred into the UHV chamber through a load lock.

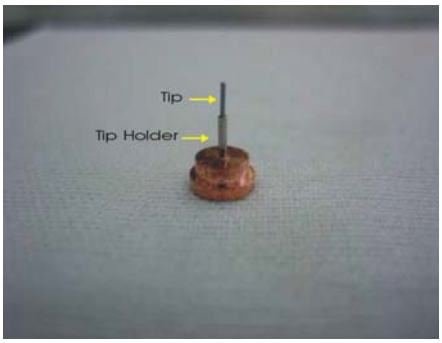

Figure 2-1 Tip and the tip holder

The tips that are prepared have an oxide layer on them that has to be removed as will be explained later in this chapter. The field emission theory and technique will be explained in the following sections as a test for sharpness of the tips that are prepared.

2.2 Field Emission Theory

Field emission is defined as the emission of electrons from a metal to vacuum under high electrostatic fields. This phenomenon can be compared to thermionic emission and photo electric emission but there is a fundamental difference between field emission and the above mentioned emissions. In field emission those electrons get emitted from the surface that can tunnel through the surface potential barrier in contrast to thermionic emission and photoelectric emission in which only the electrons having enough energy to overcome the potential barrier will be emitted. Because the electrons produced by field emission tunnel through the surface potential barrier, the configuration and changes in this potential (surface potential) can affect the field emission current. Due to this property, field emission can be used for surface science studies.

Following the development of Sommerfeld's quantum theory for electrons in metals [20], Fowler and Nordheim in 1928 first described the field emission mechanism using Sommerfeld's theory [21].

2.2.1 Electron Gas Statistics

Fowler and Nordheim, in their theory of field emission, assumed that the electrons in the metal are a gas of free particles which obey Fermi-Dirac statistics (Sommerfeld model). A complete discussion of Fermi-Dirac statistics is given in Appendix A.

2.2.2 Potential Barrier

The potential which is used for field emission process is a one dimensional potential. This potential was used by Schottky [22] on his first attempt to solve field emission theory. Later this potential was used by Nordheim [23] on his work to modify the original Fowler-Nordheim theory.

This potential is originated by the following [24]:

1. Inside a metal there is a constant potential $-W_a$ relative to zero potential where zero potential is chosen when the electron and the metal surface are separated (electron is outside of the metal).
2. The potential caused by the external electric field, F. By having the origin on the surface of the metal and the coordinate x measured perpendicular to the surface, the potential energy due to the field is $-eFx$. This potential energy is zero inside the metal (free charges inside the metal neutralize the external field).
3. When an electron comes out of metal, it feels an image potential (attractive) caused by the surface of the metal. For an electron with charge $-e$ this potential energy is $-\frac{e^2}{16\pi\varepsilon_0 x}$. The potential goes to zero when the electron is far away from the surface.

The net potential energy is

$$\psi(x) = \begin{cases} -W_a & x < 0 \\ -eFx - \dfrac{e^2}{16\pi\varepsilon_0 x} & x > 0 \end{cases} \qquad (2.\ 1)$$

A rough sketch of the net potential energy outside the metal is drawn in Figure (2-2). The electrons which tunnel through the potential barrier have been shown in this Figure. The tip Fermi level is indicated by ζ.

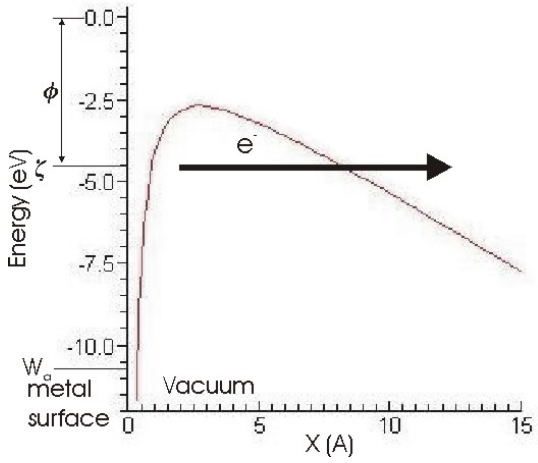

Figure 2-2 Potential energy ψ(x) from equation (2. 24) for tungsten surface (φ is the work function). For tungsten W_a = -10.3 eV, ζ =- 4.5 eV (Fermi energy level) and the applied field is $F = 5\times10^9 volt/m$. The arrow shows the tunneling phenomena of the metal electrons through the potential barrier.

The maximum point of this potential occurs at

$$x_0 = \frac{1}{4}\sqrt{\frac{e}{\pi\varepsilon_0 F}} \tag{2. 2}$$

And the maximum potential at this point is

$$\psi_{\max} = -\frac{1}{2}\sqrt{\frac{e^3 F}{\pi\varepsilon_0}} \tag{2. 3}$$

2.2.3 Quantum Mechanical Field Emission Formula

Fowler and Nordheim, in their theory of field emission, used the electron gas model for the conduction electrons in the metal and applied a one dimensional potential for the metal emitter, as discussed in section (2.2.2). Furthermore, they assumed that the electrons in the metal are in equilibrium with a small flux of electrons escaping from the surface.

The field emission current will arise from the flux of electrons hitting the surface of the metal multiplied by the probability that the electrons penetrate through the potential barrier. This current will involve an integration over all electron energies.

Assigning the total energy of an electron to ε, the x-part of the energy W of the electrons will be

$$\begin{aligned} W &= \varepsilon - \frac{{p_y}^2}{2m} - \frac{{p_z}^2}{2m} \\ &= \frac{{p_x}^2}{2m} + \psi(x) \end{aligned} \tag{2. 3}$$

Let's define $P(W)dW$ as the number of electrons having energies in the range between W and $W + dW$ that emerge from metal surface per unit time per unit area.

Throughout this chapter, $N(W)dW$ is defined as the number of electrons having energies between W and W+dW in the x direction and hitting the metal-vacuum surface (from inside of the metal) per unit area per unit time and $D(W)$ as the probability of penetration of electrons.

One then has:

$$P(W)dW = N(W)D(W)dW \tag{2. 4}$$

and the field emission current will be (per unit area)

$$j = e\int_{-W_a}^{\infty} P(W)dW \tag{2. 5}$$

One can call $N(W)$ the supply function and $D(W)$ the transmission coefficient.

First N(W) is calculated. The number of states for particles (fermions) having momentum in range of $dp_x dp_y dp_z$ is

$$dg_i = \frac{2\upsilon}{h^3} dp_x dp_y dp_z \tag{2. 6}$$

The factor 2 is there because in each phase space volume of h^3 there are 2 states for a free spin ½ fermion. Making use of the Fermi-Dirac distribution (see Appendix A), the number of electrons per unit volume having momenta in the range of $dp_x dp_y dp_z$ is then

$$dn = \frac{2\upsilon}{h^3} \frac{dp_x dp_y dp_z}{e^{\frac{\varepsilon-\zeta}{kT}} + 1} \tag{2. 7}$$

By using equation (2.8) the supply function can be calculated.

Multiplying dn by the x component (normal to the metal surface) of velocity and integrating over all p_y and p_z, N(W) is resulted. By writing ε in term of W using equation (2.4) one will obtain:

$$N(W)dW = \frac{2}{h^3} dW \int_{-\infty}^{+\infty} \int_{-\infty}^{+\infty} \frac{dp_y dp_z}{e^{\frac{W-\zeta}{kT} + \frac{{p_y}^2 + {p_z}^2}{2mkT}} + 1} \tag{2. 8}$$

In order to solve for the integral in equation (2.9) we will use polar coordinates:

$$\begin{aligned} p_y &= \rho \cos\theta \\ p_z &= \rho \sin\theta \end{aligned} \tag{2. 9}$$

With this change of parameter

$$N(W) = \frac{2}{h^3} \int_{\rho=0}^{\infty} \int_{\theta=0}^{2\pi} \frac{\rho d\rho d\theta}{e^{\frac{W-\zeta}{kT} + \frac{\rho^2}{2mkT}} + 1} \tag{2. 10}$$

Evaluating this integral gives the following result:

$$N(W) = \frac{4\pi mkT}{h^3} \ln\left(1 + e^{-\frac{W-\zeta}{kT}}\right) \tag{2. 11}$$

Now to find the transmission coefficient, $D(W)$, the time independent Schrödinger equation will be used:

$$Hu(x) = Eu(x) \tag{2. 12}$$

$$\frac{d^2u}{dx^2} + \frac{2m}{\hbar^2}\left(W - \psi(x)\right)u = 0 \tag{2. 13}$$

The transmission coefficient using Wentzel-Kramers-Brillouin (WKB) approximation will be:

$$D(W) = \exp(-\int_{x_1}^{x_2} \sqrt{\frac{8m}{\hbar^2}\left[\psi(x) - W\right]}dx) \tag{2. 14}$$

where x_1 and x_2 ($x_1 < x_2$) are the zeroes of equation

$$\psi(W) = W \tag{2. 15}$$

These classical turning points are given by:

$$\begin{matrix} x_1 \\ = \\ x_2 \end{matrix} \frac{|W|}{2eF}\left(1 \mp \sqrt{1 - \frac{e^3F}{4\pi\varepsilon_0 W^2}}\right) \tag{2. 16}$$

The WKB approximation is valid for the conditions that W is appreciably less than ψ_{max} which is the range required for field emission.

Taking the logarithm of equation (2. 15) and substituting for ψ(x) from equation (2.1), results in:

$$-\ln D = \int_{x_1}^{x_2} \sqrt{\frac{8m}{\hbar^2}\left(-eFx + |W| - \frac{e^2}{16\pi\varepsilon_0 x}\right)}dx \tag{2. 17}$$

Using these new parameters by looking at the x_1 and x_2, one can define:

$$y = \sqrt{\frac{e^3 F}{4\pi\varepsilon_0}} \frac{1}{|W|}$$
$$\xi = \frac{2eF}{|W|} x \tag{2. 18}$$

Equation (2.18) can be rewritten as

$$-\ln D = \frac{\sqrt{m|W|^3}}{\hbar eF} \int_{1-\sqrt{1-y^2}}^{1+\sqrt{1-y^2}} \sqrt{-\xi^2 + 2\xi - y^2}\, \frac{d\xi}{\sqrt{\xi}} \tag{2. 19}$$

Now by introducing $\eta = \sqrt{\xi}$, one can write:

$$2d\eta = \frac{d\xi}{\sqrt{\xi}}$$
$$-\xi^2 + 2\xi - y^2 = \left(\left(1+\sqrt{1-y^2}\right) - \eta^2\right)\left(\eta^2 - \left(1+\sqrt{1-y^2}\right)\right) \tag{2. 20}$$
$$= \left(a^2 - \eta^2\right)\left(\eta^2 - b^2\right)$$

where a and b are defined as:

$$a = \sqrt{1+\sqrt{1-y^2}}$$
$$b = \sqrt{1-\sqrt{1-y^2}} \tag{2. 21}$$

Using these new parameters, equation (2. 20) becomes:

$$-\ln D = \frac{2\sqrt{m|W|^3}}{\hbar eF} \int_b^a \sqrt{\left(a^2 - \eta^2\right)\left(\eta^2 - b^2\right)}\, d\eta \tag{2. 22}$$

This integral is a standard form of an elliptic integral.

$$-\ln D = \frac{4\sqrt{m|W|^3}\,a}{3\hbar eF}\left[\frac{\left(a^2+b^2\right)}{2}E\left(k\right)-b^2K(k)\right] \tag{2. 23}$$

where k is defined as:

$$k^2 = \frac{a^2-b^2}{a^2} \tag{2. 24}$$

The integrals E(k) and K(k) are the complete elliptic integrals of first and second kinds

$$\begin{aligned} K(k) &= \int_0^{2\pi} \frac{d\varphi}{\sqrt{1-k^2\sin^2\varphi}} \\ E(k) &= \int_0^{2\pi} \sqrt{1-k^2\sin^2\varphi}\,d\varphi \end{aligned} \tag{2. 25}$$

Writing a and b in term of *y* and using equation (2.25) and equation (2.19), and defining v(y) as:

$$v\left(y\right) = \frac{1}{\sqrt{2}}\sqrt{1+\sqrt{1-y^2}}\left[E\left(k\right)-\left(1-\sqrt{1-y^2}\right)K(k)\right] \tag{2. 26}$$

equation (2. 24) can be rewritten as:

$$D(W) = \exp\left(-\frac{4\sqrt{2m|W|^3}}{3\hbar eF}v\left(\sqrt{\frac{e^3F}{4\pi\varepsilon_0}}\frac{1}{|W|}\right)\right) \tag{2. 27}$$

Expressions for $N\left(W\right)$ and $D\left(W\right)$ have been found by equation (2. 12) and (2. 28) respectively. Substituting $N\left(W\right)$ and $D\left(W\right)$ back to $P\left(W\right)dW$, will result in:

$$P(W)\,dW = N(W)\,D(W)\,dW \tag{2.28}$$

$$P(W)\,dW = \frac{4\pi mkT}{h^3}\exp\left(-\frac{4\sqrt{2m|W|^3}}{3\hbar eF}v\left(\sqrt{\frac{e^3F}{4\pi\varepsilon_0}}\frac{1}{|W|}\right)\right)\ln\left(1+e^{-\frac{W-\zeta}{kT}}\right)dW \tag{2.29}$$

The majority of the electrons undergoing field emission are those that have their energy near the Fermi level, so we can write $W \approx \zeta$. With this condition the exponent in the transmission coefficient can be approximated by the first two terms of its Taylor series:

$$\begin{aligned}-\frac{4\sqrt{2m|W|^3}}{3\hbar eF}v\left(\sqrt{\frac{e^3F}{4\pi\varepsilon_0}}\frac{1}{|W|}\right) \approx & \\ -\frac{4\sqrt{2m\varphi^3}}{3\hbar eF}v\left(\sqrt{\frac{e^3F}{4\pi\varepsilon_0}}\frac{1}{\varphi}\right) - 2\frac{\sqrt{2m|W|}}{\hbar eF}\left(v(y)-\frac{2}{3}y\frac{dv(y)}{dy}\right)(W-\zeta) & \\ \approx -c+(W-\zeta)\frac{1}{d} &\end{aligned} \tag{2.30}$$

where c and d are defined by:

$$\begin{aligned} c &= 4\frac{\sqrt{2m\varphi^3}}{3\hbar eF}v\left(\sqrt{\frac{e^3F}{4\pi\varepsilon_0}}\frac{1}{\varphi}\right) \\ d &= \frac{\hbar eF}{2\sqrt{2m\varphi}t\left(\sqrt{\frac{e^3F}{4\pi\varepsilon_0}}\frac{1}{\varphi}\right)} \end{aligned} \tag{2.31}$$

and t is defined as:

$$t(y) = v(y) - \frac{2}{3}y\frac{dv(y)}{dy} \tag{2.32}$$

In the above equations $\varphi = -\zeta$ have been used, where φ is the work function.

For low enough temperatures (kT ≈ 0) the logarithm in $N(W)$ can be approximated as follows:

$$kT\ln\left(1+e^{-\frac{W-\zeta}{kT}}\right)=\begin{cases}0 & W>\zeta\\ \zeta-W & W<\zeta\end{cases} \tag{2. 33}$$

Using equation (2.31) and (2. 34) in equation (2. 30) will result in:

$$P(W)=\begin{cases}0 & W>\zeta\\ \dfrac{4\pi m}{h^3}e^{-c+\frac{W-\zeta}{d}}(\zeta-W) & W<\zeta\end{cases} \tag{2. 34}$$

which is the low temperature approach for $P(W)$ [24].

The maximum for the function $P(W)$ occurs at:

$$W=\zeta-d \tag{2. 35}$$

and the value of $P(W)$ at this point is

$$P_{\max}=\frac{4\pi md}{h^3}e^{-(c+1)} \tag{2. 36}$$

The field emission current density is found by integrating $P(W)$ over all energies

$$j=e\int_{-W_a}^{\infty}P(W)\,dW \tag{2. 37}$$

Usually $-W_a$ is far lower than the Fermi energy (ζ) so we can change the lower bound to $-\infty$, using equation (2. 35) for $P(W)$

$$j = e\int_{-\infty}^{\zeta} \frac{4\pi m}{h^3} e^{\left(-c+\frac{W-\zeta}{d}\right)} (\zeta - W)\, dW$$
$$= \frac{4\pi med^2}{h^3} e^{-c} \tag{2. 38}$$

After substituting for c and d from equation (2.32) we have

$$j = \frac{e^3 F^2}{8\pi h\varphi t^2\left(\sqrt{\frac{e^3F}{4\pi\varepsilon_0}}\frac{1}{\varphi}\right)} e^{-\frac{4\sqrt{2m\varphi^3}}{3\hbar eF} v\left(\sqrt{\frac{e^3F}{4\pi\varepsilon_0}}\frac{1}{\varphi}\right)} \tag{2. 39}$$

2.2.4 Field Emission at Higher Temperatures

The formula for the field emission current, equation (2.40), was derived using the low temperature approximation of the $kT \ln\left(1+e^{-\frac{W-\zeta}{kT}}\right)$ part of N(W). At finite temperatures some electrons have energies above the Fermi energy. These electrons have a higher probability of penetrating through the potential barrier (as transmission coefficient increases as electrons have higher energy). Around room temperature the correction for the current is very small but for higher temperatures, the character of emission changes, which results in a large correction. This is due to the reason that at higher temperature the electrons having energies higher than the Fermi energy contribute to the current rather than the electrons having energies lower than Fermi energy as in the field emission process.

For high temperatures, the process is called thermionic emission and the source of current is the electrons having energies higher than the maximum of the potential barrier ($\psi_{\max}$) so they do not tunnel through the potential barrier.

In order to determine the change in $P(W)dW$ at higher temperatures, equation (2. 30) (where the approximation for low temperature is not applied) is used.

$$P(W)dW = \frac{4\pi mkT}{h^3}\exp(-\frac{4\sqrt{2m|W|^3}}{3\hbar eF}v\left(\sqrt{\frac{e^3F}{4\pi\varepsilon_0}}\frac{1}{|W|}\right))\ln\left(1+e^{-\frac{W-\zeta}{kT}}\right)dW \qquad (2.\ 40)$$

This formula is valid for $W << \psi_{\max}$, as this condition is the assumption in the WKB approximation for the transmission coefficient. Dolan and Dyke [25] have plotted the distribution in W, energy of the electrons emerging from the metal surface, for a few values of temperatures and fields and for a tungsten emitter (Figure (2-3)).

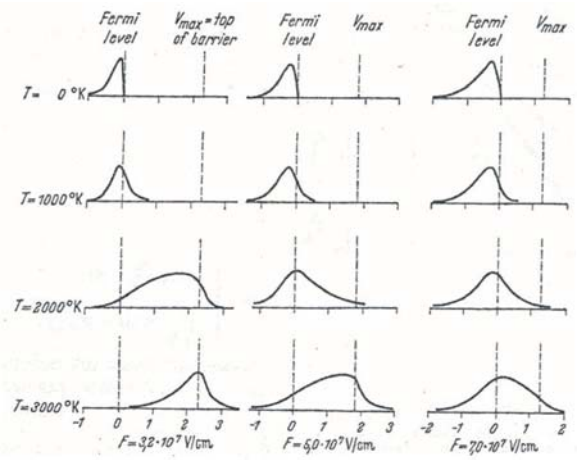

Figure 2-3 Plots of P(W) at various temperatures and fields for tungsten tip [Data taken from Ref. [25]]

In this section, the approach of Dolan and Dyke is followed closely. For electrons having energies below $\psi_{\max}$, Dolan et al [25] used equation (2. 12) as the supply function and equation (2. 28) as the transmission coefficient of electrons with energies below $\psi_{\max}$. The transmission coefficient for electrons with energies above $\psi_{\max}$ was unity. This assumption is not completely correct as the transmission coefficient will be about $\frac{1}{2}$ when $W = \psi_{\max}$ and gradually increases to unity as W increases [24].

As done earlier, the transmission coefficient is approximated by expanding the exponent at $W = \zeta$, as expressed in equation (2. 31). The expression for $P(W)$ will be:

$$P(W) = \frac{4\pi mkT}{h^3} e^{-c+\frac{W-\zeta}{d}} \ln\left(1+e^{-\frac{W-\zeta}{kT}}\right) \tag{2. 41}$$

For $W > \zeta$ we can approximate the logarithm

$$\ln\left(1+e^{-\frac{W-\zeta}{kT}}\right) \approx e^{-\frac{W-\zeta}{kT}} \tag{2. 42}$$

Plugging this expression in equation (2. 42) results in:

$$P(W) = \frac{4\pi m}{h^3} e^{-c+(W-\zeta)\left(\frac{1}{d}-\frac{1}{kT}\right)} \tag{2. 43}$$

This equation is quite useful since it shows us a range for the temperature and the field, so that the emitting current originates from the field emission process (where W is less

than $\varphi_{\max}$, in other words electrons tunnel through the potential barrier). For this to happen the exponential part should make $P(W)$ small as W approaches $\psi_{\max}$ and it can written as:

$$(\psi_{\max} - \zeta)\left(\frac{1}{d} - \frac{1}{kT}\right) < -1 \tag{2. 44}$$

From equation (2. 3) one has:

$$\psi_{\max} = -\frac{1}{2}\sqrt{\frac{e^3 F}{\pi\varepsilon_0}} \tag{2. 45}$$

and $\zeta = \varphi$. Substituting for $\psi_{\max}$ and ζ in equation (2. 45) results in:

$$\frac{1}{kT} > \frac{1}{d} + \frac{1}{\varphi - \frac{1}{2}\sqrt{\frac{e^3 F}{\pi\varepsilon_0}}} \tag{2. 46}$$

For typical values of φ and F the second term is small compared to the first term so:

$$\frac{1}{kT} > \frac{1}{d} \rightarrow d > kT \tag{2. 47}$$

and substituting for d from equation (2. 32) results in:

$$\frac{\hbar e F}{2\sqrt{2m\varphi}\, t(y)} > kT \tag{2. 48}$$

and

$$F > \frac{2\sqrt{2m\varphi}t\left(\sqrt{\frac{e^3F}{4\pi\varepsilon_0}}\frac{1}{\varphi}\right)kT}{\hbar e} \tag{2. 49}$$

The parameter t(y) is a slowly varying function, ranging only between 1.00 and 1.11 [24].

Equation (2.50) shows a threshold for the applied electric field, above which the field emission process is the main emission process. Below this threshold, the electrons that contribute to the current will mainly be from electrons with energies higher than the Fermi level and the dominant process is no longer field emission, but rather thermionic emission.

Assuming that the condition (equation (2. 50)) is valid, then we are only concerned about the field emission process. From equation (2. 42) the total current per unit time per unit area is resulted by integrating $P(W)$ over all energies.

$$j(T) = e\int_{-\infty}^{\infty} P(W)\,dW = \frac{4\pi emkT}{h^3}e^{-c}\int_{-\infty}^{\infty} e^{\frac{W-\zeta}{d}}\ln\left(1+e^{-\frac{W-\zeta}{kT}}\right)dW \tag{2. 50}$$

By defining $\xi = e^{\frac{W-\zeta}{kT}}$, and integrating by parts the following is obtained:

$$\begin{aligned} j(T) &= \frac{4\pi emkTd}{h^3}e^{-c}\int_0^{\infty}\frac{\xi^{\left(\frac{kT}{d}-1\right)}}{1+\xi}d\xi \\ &= \frac{4\pi emkTd}{h^3}e^{-c}\frac{\pi}{\sin\left(\frac{\pi kT}{d}\right)} \end{aligned} \tag{2. 51}$$

This expression can be written as:

$$j(T) = j(0)\frac{\frac{\pi kT}{d}}{\sin\left(\frac{\pi kT}{d}\right)} \tag{2. 52}$$

where j(0) is the current density for zero temperature as equation (2. 40).

$$j(0) = \frac{e^3 F^2}{8\pi h\varphi t^2(y)} e^{-c} \tag{2. 53}$$

For low temperatures we can expand and approximate the term $\frac{\frac{\pi kT}{d}}{\sin\left(\frac{\pi kT}{d}\right)}$ in equation (2. 53). By defining $x \equiv \frac{\pi kT}{d}$, j(T) can be written as :

$$j(T) = j(0)\left(1 + \frac{1}{6}\left(\frac{\pi kT}{d}\right)^2 + \cdots\right) \tag{2. 54}$$

By plugging in some typical numbers for field value on a tungsten tip, at room temperature, equation (2. 55) one will obtain $j(T) = 1.03\, j(0)$. As mentioned before, the correction around room temperature is small. For T = 1000 K, this correction is $j(T) = 1.5\, j(0)$ which is more significant.

2.3 Numerical Results for Field Emission

In the previous section the field emission current formula was derived analytically by approximating the energies of all electrons to be near the Fermi energy. One can avoid making this approximation by resorting to numerical calculation. Since these numerical calculations are not computationally intensive one can easily check the analytic results and also calculate the emission current under more general conditions. For example numerical code can be written that incorporates both field emission and thermionic emission. Also, a more realistic density of states function than what is obtained from the free electron approximation could be used in the future. The transmission coefficient for each energy, W, was calculated numerically and the result was inserted in equation (2. 41). The result, P(W), was integrated over an acceptable energy range at room temperature.

2.3.1 Field Emission Current Calculation

Numerically the transmission coefficient was calculated in two approaches, first using equation (2. 20):

$$D(W) = \exp\left(-\frac{\sqrt{m|W|^3}}{\hbar eF}\int_{1-\sqrt{1-y^2}}^{1+\sqrt{1-y^2}} \sqrt{-\xi^2+2\xi-y^2}\,\frac{d\xi}{\sqrt{\xi}}\right) \qquad (2.\ 55)$$

Second, using equation (2. 28):

$$D(W) = \exp\left[-\frac{4\sqrt{2m|W|^3}}{3\hbar eF}\left(\frac{1}{\sqrt{2}}\sqrt{1+\sqrt{1-y^2}}\left[E(k) - \left(1-\sqrt{1-y^2}\right)K(k) \right] \right) \right] \qquad (2.\ 56)$$

In both ways Simpson's rule was used for integration. It should be mentioned that the calculations were not computationally intensive. By plugging the transmission coefficient in equation (2. 30)

$$P(W)\,dW = \frac{4\pi mkT}{h^3} D(W) \ln\left(1 + e^{-\frac{W-\zeta}{kT}} \right) dW \qquad (2.\ 57)$$

and integrating $P(W)$ from 1.6*ζ to 0.85* ζ, where ζ is the Fermi energy for tungsten. The interval was chosen this way because of the following reasons:

1. By plotting equation (2. 12) there is no use in integrating over ($0.85 \cdot \zeta$) energy since $N(W)$ will be zero around ζ at room temperature, as can be seen in Figure (2-4). The reason is that not many states are filled by electrons above the Fermi level at room temperature. A graph of $N(W)$ over a range of -11.5 eV ($3 \cdot \zeta$) to -2.25 eV ($0.5 \cdot \zeta$) is plotted in Figure (2-4).

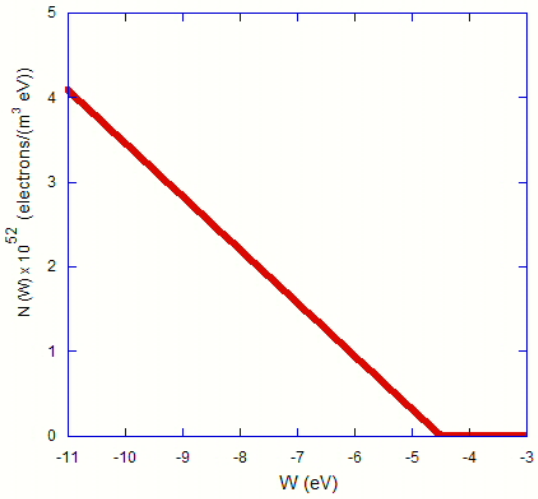

Figure 2-4 Supply function, $N(W)$, from equation (2. 12) for $3.0 \cdot \zeta \le W \le 0.5 \cdot \zeta$, for a tungsten tip with $F = 5 \cdot 10^9 \, volt/m$

2. Figure (2-5) is the transmission function $D(W)$ using equation (2. 56).

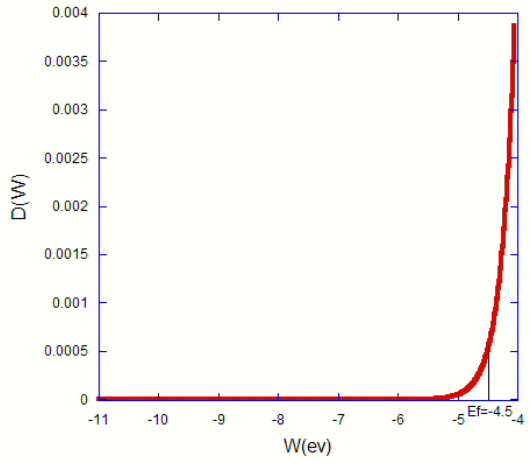

Figure 2-5 Transmission coefficient, $D(W)$, from equation (2. 56) for $3.0 \cdot \zeta \le W \le 0.9 \cdot \zeta$, for a tungsten tip with $F = 5 \cdot 10^9 \, volt/m$

It can be seen that below -7.2 eV ($1.6 \cdot \zeta$) the transmission coefficient is nearly zero, hence, integrating over energies less than $1.6 \cdot \zeta$ is also zero.

The plot of $P(W)$ from equation (2. 29) versus W is shown in Figure (2-6).

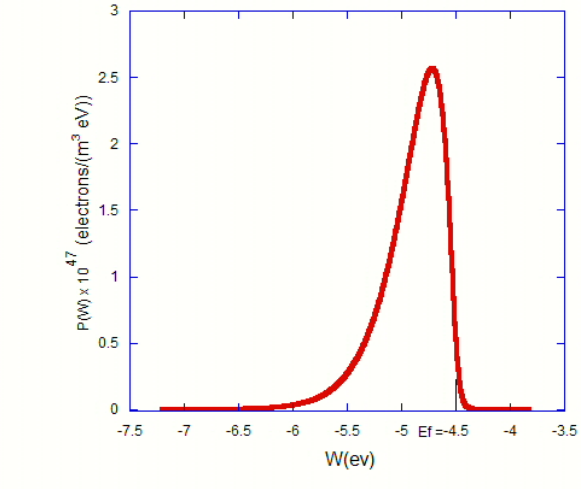

Figure 2-6 Plot of $P(W)$ for $1.6 \cdot \zeta \le W \le 0.85 \cdot \zeta$, for a tungsten tip with $F = 5 \cdot 10^9 volt/m$

Calculating the integral of $P(W)$ over the energy interval mentioned, the current density can be calculated by multiplying the result by electron charge.

$$j = e \int_{0.85 \cdot \zeta}^{1.6 \cdot \zeta} P(W) dW \qquad (2.\ 58)$$

In Table (2.1) the numerical results for the calculated current density (for room and zero temperature) are compared to numerical results from Dolan [26]. Dolan calculated j using equation (2. 40), setting t equal to unity.

Table 2-1 Calculated Log(j) for different fields for tungsten at zero and room temperature, using the numerical code and Doland's calculation [26]

F(volt/m) $\times 10^9$	Numerical Calculation Log(j) x10^4 (j in $\frac{amps}{m^2}$) T = 300 K	Numerical Calculation Log(j) x10^4 (j in $\frac{amps}{m^2}$) T = 0 K	Dolan's Calculation Log(j) x10^4 (j in $\frac{amps}{m^2}$) T = 0 K
2.0	-3.29	-3.33	-3.32
3.0	1.59	1.56	1.61
4.0	4.07	4.06	4.11
5.0	5.58	5.57	5.64
6.0	6.61	6.60	6.68
7.0	7.35	7.34	7.43
8.0	7.91	7.91	8.01
9.0	8.36	8.36	8.46
10.0	8.72	8.72	8.83

At zero temperature our result differs by Dolan's result by ~1%. By looking at the results for T = 300 K and T = 0 K it can be seen that, as mentioned earlier in section (2.1.4), the correction for room temperature is small.

Taking the logarithm of equation (2.40) results in:

$$\ln(j) = \ln\left(\frac{e^3F^2}{8\pi h\varphi t^2\left(\sqrt{\frac{e^3F}{4\pi\varepsilon_0}}\frac{1}{\varphi}\right)}\right) - \frac{4\sqrt{2m\varphi^3}}{3\hbar eF}v\left(\sqrt{\frac{e^3F}{4\pi\varepsilon_0}}\frac{1}{\varphi}\right) \qquad (2.59)$$

The logarithm of j versus $\frac{1}{F}$ was plotted for a tungsten tip with work function of φ = -4.5 eV [27] as shown in Figure (2-7).

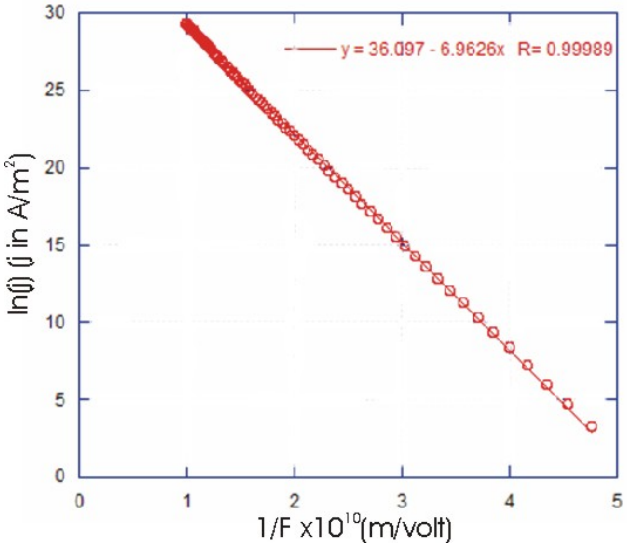

Figure 2-7 Plot of $\ln(j)$ versus $\frac{1}{F}$ from numerical calculation of j for a tungsten tip. A straight line fit is also included.

Though the plot results in a fairly straight line, as one can see by comparison to the straight-line fit, the relationship is not perfectly linear. This can be understood by looking at equation (2.60), where the function $v\left(\sqrt{\frac{e^3F}{4\pi\varepsilon_0}}\frac{1}{\varphi}\right)$ has some dependence on the field strength F.

2.3.2 Numerical Results for Fowler-Nordheim Plots

Using equation (2. 40), dividing it by F^2 and taking the logarithm of both sides results in:

$$\ln\left(\frac{j}{F^2}\right) = \ln\left(\frac{e^3}{8\pi h\varphi t^2\left(\sqrt{\frac{e^3F}{4\pi\varepsilon_0}}\frac{1}{\varphi}\right)}\right) - \frac{4\sqrt{2m\varphi^3}}{3\hbar eF}v\left(\sqrt{\frac{e^3F}{4\pi\varepsilon_0}}\frac{1}{\varphi}\right) \qquad (2.\ 60)$$

From the equation (2.61), the plot of $\ln\left(\frac{j}{F^2}\right)$ vs. $\frac{1}{F}$ will be close to a straight line (if the function $v\left(\sqrt{\frac{e^3F}{4\pi\varepsilon_0}}\frac{1}{\varphi}\right)$ is a slowly varying function of F) with a slope of $-\frac{4\sqrt{2m\varphi^3}}{3\hbar e}v\left(\sqrt{\frac{e^3F}{4\pi\varepsilon_0}}\frac{1}{\varphi}\right)$. Such a plot is called a Fowler-Nordheim plot (F-N plot) [24].

Figure (2-8) is a F-N plot, using the numerical results as mentioned earlier for a tungsten tip. It can be seen the graph is approximately a straight line.

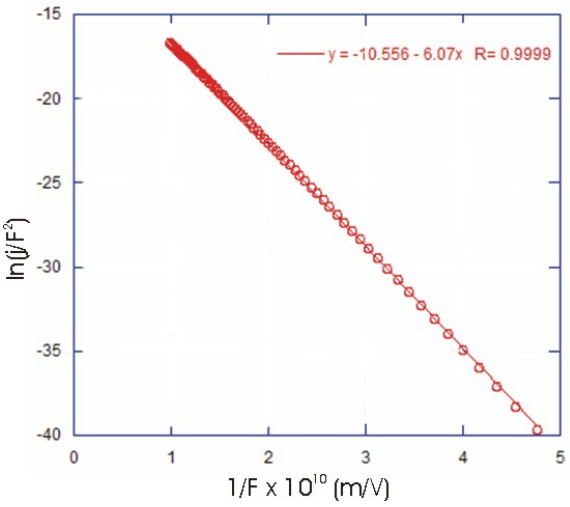

Figure 2-8 Fowler-Nordheim plot from numerical calculation of j for tungsten tip. A straight line fit is also included.

2.4 Experimental Results for Field Emission

The field emission experiment is performed by applying high voltage between a sharp emitter and an anode. As mentioned earlier, field emission can be used to test or assess a given tip's sharpness before use in STM experiments. In the following section this test is explained.

2.4.1 Experimental Setup

The field emission (FE) experiments are conducted in the STM chamber. In the field emission setup, the tip holder was placed in a stage which was connected to a high voltage supply by an electrical feedthrough and was isolated from the chamber. Above

the tip, a tantalum filament was used as an anode which was grounded in this setup. Instead of connecting the high voltage supply directly to the tip, the current was passed through a 1.0 MΩ resistor which was connected to a voltmeter. During the field emission process the voltage across the resistor changes, from which we obtain the current. The electrical schematic of the field emission is shown in Figure (2-9).

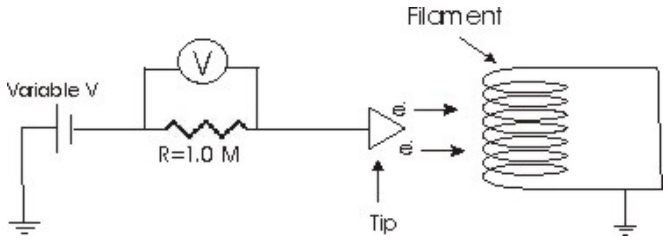

Figure 2-9 Electrical schematic of the field emission setup

The base pressure of the chamber was maintained to lower than $4 \cdot 10^{-11} Torr$, which is in the ultra high vacuum (UHV) range. The field emission experiments require high vacuum for two reasons [28]. First, there is a need for uncontaminated tips for a long duration of time. As pressure increases, the flux of the residual gases hitting the surface increases. Second, gas discharges at high voltages must be prevented since ion bombardment damages (blunts) the tip by pitting the surface of the tip.

2.4.2 A Simple Test for Tip Sharpness (FE Test)

As mentioned earlier the typical electric field required for field emission is around $5 \cdot 10^{9} Volt/m$. Producing this field requires a high voltage. There is a trick for

producing this field by an acceptable voltage. The electric field is stronger at surfaces with high curvature. In other words, near sharp points the electric field is much stronger than above flat surfaces. In the field emission process very sharp tips with a radius on the order of 100 nm are used, which results in very high electric fields around the tip.

If a voltage V is applied to a conductive sphere with a radius r the electric field around the sphere will be [29]

$$F = \frac{V}{r} \tag{2. 61}$$

In practice, since the surfaces of the tips are usually not perfectly spherical, the electric field (F) is reduced because of the presence of a cylindrical or conical shank. This reduction will change F by a factor k

$$F = \frac{V}{kr} \tag{2. 62}$$

where $k \approx 5$ gives an acceptable result for most tips [28].

Rewriting equation (2. 40) and substituting equation (2. 63) for F will result in:

$$j = \frac{e^3 V^2}{8\pi h \varphi k^2 r^2 t^2 \left(\sqrt{\frac{e^3 F}{4\pi\varepsilon_0}} \frac{1}{\varphi} \right)} e^{-\frac{4\sqrt{2m\varphi^3}}{3\hbar eF} v\left(\sqrt{\frac{e^3 F}{4\pi\varepsilon_0}} \frac{1}{\varphi} \right)} \tag{2. 63}$$

Setting $t \approx 1$ (as mentioned that t is very slowly varying function) and by multiplying both sides of this equation by "a", the field emitting area, one obtains

$$I = \frac{ae^3}{8\pi h\varphi}\left(\frac{V}{kr}\right)^2 e^{-\frac{4\sqrt{2m\varphi^3}}{3\hbar eF}v(y)} \qquad (2.\ 64)$$

By looking at equation (2. 65) it can be seen that for a certain applied voltage a sharper tip will result in higher field emission current. In other words a sharper tip will show a certain current at a lower threshold voltage compared to a blunt tip, and this is our simple test for checking the sharpness of the tips.

Experimentally we found that the tips that produce a current of about 1.0 nA at around 320 V bias and that are also stable at this voltage are usually good tips for STM experiments and result in good quality images. By stable it is meant that the field emission current is constant for an acceptable duration of time (about 40 sec).

2.4.3 Estimating Tip Radius using Fowler-Nordheim Plots

Equation (2.66) is the original Fowler-Nordheim equation, where Schottky's image potential was not taken into account [21].

$$j = \frac{4\sqrt{\mu\varphi}}{\mu+\varphi}\frac{e^3F^2}{8\pi h\varphi}e^{-\frac{4\sqrt{2m\varphi^3}}{3\hbar eF}} \qquad (2.\ 65)$$

Taking the logarithm of this equation after dividing both sides by F^2 one obtains:

$$\ln\left(\frac{j}{F^2}\right) = \ln\left(\frac{4\sqrt{\mu\varphi}}{\mu+\varphi}\frac{e^3}{8\pi h\varphi}\right) - \frac{4\sqrt{2m\varphi^3}}{3\hbar eF} \qquad (2.\ 66)$$

The field emission current density, j, when taking the image potential into account is defined as:

$$j = \frac{e^3 F^2}{8\pi h\varphi} e^{-\frac{4\sqrt{2m\varphi^3}}{3\hbar eF} v\left(\sqrt{\frac{e^3 F}{4\pi\varepsilon_0}}\frac{1}{\varphi}\right)} \tag{2. 67}$$

This is after taking $t \approx 1$ [24]. Taking the logarithm of this function after dividing both sides by F^2 results in:

$$\ln\left(\frac{j}{F^2}\right) = \ln\left(\frac{e^3}{8\pi h\varphi}\right) - \frac{4\sqrt{2m\varphi^3}}{3\hbar eF} v\left(\sqrt{\frac{e^3 F}{4\pi\varepsilon_0}}\frac{1}{\varphi}\right) \tag{2. 68}$$

Comparing equation (2. 67) and (2. 69) we will notice that $v\left(\sqrt{\frac{e^3 F}{4\pi\varepsilon_0}}\frac{1}{\varphi}\right)$ is the factor corresponding to the image potential. This image potential correction increases (by lowering the potential barrier) the field emission current predicted by the original Fowler-Nordheim equation. For a certain field emission current, by considering the image potential correction, 10%-20% lower electric field is required, compared to the condition where the image potential is not taken into account [28].

Taking the logarithm of equation (2. 65) after dividing both sides by V^2 and substituting for F from equation (2. 63), one obtains:

$$\ln\left(\frac{I}{V^2}\right) = \ln\left(\frac{ae^3}{8\pi h\varphi}\left(\frac{1}{kr}\right)^2\right) - \frac{4\sqrt{2m\varphi^3}kr}{3\hbar eV} v(y) \tag{2. 69}$$

This equation can be written as

$$\ln\left(\frac{I}{V^2}\right) = b + \frac{c}{V} \tag{2. 70}$$

where b and c are defined as

$$\begin{aligned} b &= \ln\left(\frac{ae^3}{8\pi h\varphi}\left(\frac{1}{kr}\right)^2\right) \\ c &= -\frac{4\sqrt{2m\varphi^3}kr}{3\hbar e}v(y) \end{aligned} \tag{2. 71}$$

By looking at equation (2. 71), one can see that if one plots $\ln\left(\frac{I}{V^2}\right)$ versus $\frac{1}{V}$ the slope will be c.

In Figure (2-10) an experimental F-N plot for a tungsten tip is shown.

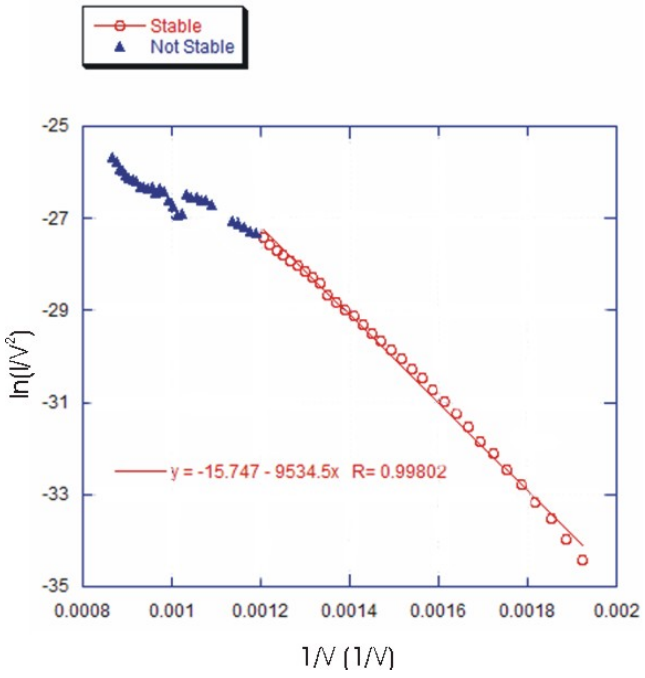

Figure 2-10 F-N plot for a polycrystalline tungsten tip. Stable and unstable conditions are shown and curve fit has been performed for the stable part.

By looking at Figure (2-10) one can see that the tip is not stable at high voltages (above -830 V). It is believed that this unstable situation happened because of the following reason: at high voltages, high field emission currents densities are produced at the tip causing the tip to heat up. At these high temperatures different processes can occur. First, the tip might get cleaner because the tungsten oxide layer (left from the preparing process) can be evaporated (vanish) to a greater degree. Second, at high temperatures caused by the high current density and in presence of high electric field atoms can rearrange on the top of the tip [30, 31].

For tips that are not field emitting properly (that is, the test that was mentioned in section (2.3.2) shows that the tip is not sharp enough), by taking the tip to high voltages and keeping it there for a short time, the tip might field emit better afterwards. This process is used for shaping the blunt tips, and will be explained more in section 2.5.2.

By looking at the stable part of the graph it can be seen that $\ln\left(\frac{I}{V^2}\right)$ vs $\frac{1}{V}$ is almost a straight line (the line of best fit is drawn on the graph), as was predicted by equation (2. 71). By knowing the slope of this line, c, which is defined by equation (2. 72) and knowing φ, k and $v(y)$ one can find r, the radius of the tip.

The value of k depends on the shape of the emitter and apex radius. The shape of the tip-shank can be simulated and using this simulated shape one can find a value for k [28]. For example if the shape of the tip-shank is approximated by a paraboloid of revolution, the k related to this shape is

$$k = \frac{1}{2}\ln\left(\frac{x}{r}\right) \qquad (2.\ 72)$$

where r is the tip radius and x is the distance between tip and the anode.

For a hyperboloid, k will be:

$$k = \frac{1}{2}\ln\left(\frac{4x}{r}\right) \qquad (2.\ 73)$$

Charbonnier in Dyke's group [28] found an empirical formula:

$$k = 0.59\varepsilon^{\frac{1}{2}}\left(\frac{x}{r}\right)^{0.13} \tag{2. 74}$$

where x and r are as defined above (in cm) and ε (deg) is the emitter-cone half angle. This result was achieved by using electron microscope examinations of the I-V characteristics of a large number of tips. A value of $k \approx 5$ was obtained for most of the tips that were studied by this group.

Knowing the work function of the tip (emitter) which is -4.5 eV for tungsten [27] and setting $v(y) \approx 1$ and $k \approx 5$ in equation (2. 72) the radius of the tip can be estimated within 20% error [28]. For the tip in Figure (2-10):

$$\begin{aligned} c &= -9534.5 \\ -\frac{4\sqrt{2m\varphi^3}\,5r}{3\hbar e} &= -9534.5 \end{aligned} \tag{2. 75}$$

This results in $r = 29.3nm$. By taking to account the 20% error, $r = (29 \pm 6)nm$.

The tunneling area, a, of the tip can be calculated using the intercept of the F-N plot using equation (2.72). Knowing the work function of tungsten and setting k = 5, one will obtain ~8.9x10^3(nm^2) for the tunneling area of this tip. Given that this area is close to the surface area of a sphere with radius 29 nm, this area seems consistent with what one might expect for the area of that part of the tip that contributes significantly to field emission.

A recent study [32, 33] suggests that the value of k can be between 3 and 35 as lower and upper limits. The k drops from 5 to 3 because annealing the tip at high temperatures

causes a blunting effect. Using $3 \le k \le 35$ for the tip in Figure (2-10) one will obtain a value for the radius of the tip between 49 and 4 nm.

The right value for k can be found once the tip is observed with electron microscopy [33] by finding the tip-shank shape, but once the tip is observed by electron microscope, one can estimate the exact radius of the tip (no need for estimating it using F-N plot)!

Figure (2-11) shows the F-N plots of two tips. Tip A is the tip used in Figure (2-10) (the stable part) and tip B is a different tip.

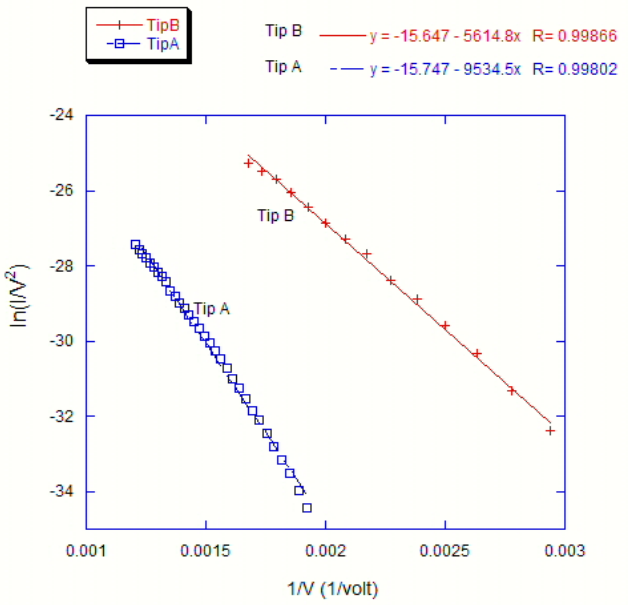

Figure 2-11 F-N plots for two different tungsten tips. Both tips were prepared the same way using the chemical etching procedure and the same EB cleaning procedure explained in section 2.5.

From equation (2. 72), $c = -\frac{4\sqrt{2m\varphi^3}kr}{3\hbar e}$, one can see that the slope of the F-N plot is proportional to the radius of the tip. That means a tip with a larger radius should have a larger slope. The slope for tip A is $9.5\text{x}10^3$ (A/V) and for tip B is $5.6\text{x}10^3$ (A/V). So tip A should have a larger radius compared to tip B. As before, taking $k \approx 5, \alpha \approx 1$ and using equation (2. 72) for tip A will result in $r_A = 29nm$ and for tip B, $r_B = 17nm$.

The field emission test, explained in section (2.3.2), was done on both tips. For a field emission current of 1.0 nA, tip A was set to $V_A \approx 570V$ and tip B was set to $V_B \approx 340V$. This shows that tip B reached 1.0 nA at a lower voltage, indicating that the tip B is sharper than tip A. This can be seen in the Figure (2-11), by noticing that the F-N plot for tip B starts at lower voltages; in other words the F-N plot of the sharp tip is shifted to the right of the x axis. A smaller slope in Fowler-Nordheim plot is an indication of a sharper tip.

It has been shown that for ultra sharp tips of radius around 1-3nm there is a deviation from the Fowler-Nordheim formula [34]. The reason is that the apex radius of these tips is closer to or even less than the barrier width. This means that approximating the barrier on the metal-vacuum boundary as planar is no longer valid. This makes the electrostatic field at the apex surface not uniform and thus the potential barrier is asymmetric. For the tips that are being prepared (by the method explained earlier), the radius is not on the order of a few nm, so one is not be dealing with such a case.

2.5 Procedures for Cleaning and Improving Tips (Electron Bombardment)

When the tips have been prepared by electrochemical etching process, there remains a tungsten oxide layer on the tip. If the FE test is performed on these tips it will be noticed that these new tips usually field emit only at high voltages and/or the FE current is not stable. In another case, if the tip is field emitting at high voltages there is a chance to improve the tip. In this section electron bombardment is described, which is a very useful method for cleaning and improving tips.

2.5.1 Principal of Operation and Experimental Setup

In electron bombardment (EB) the surface of the tip is being bombarded by energetic electrons. For this to happen the tip is held at a high positive voltage. An electrical schematic of the EB setup is shown in Figure (2-12).

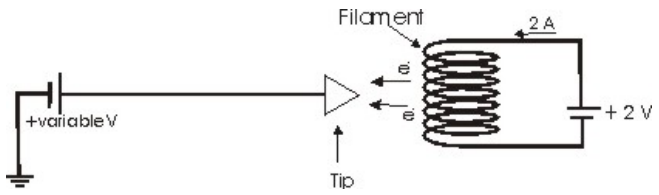

Figure 2-12 Electrical schematic of EB setup. The high voltage supply used to provide the variable potential has a built in ammeter to monitor the EB current.

A current is passed through the filament above the tip causing the filament to heat up and through the thermionic process electrons are produced from the filament. Electrons being produced by the filament accelerate towards the tip since the tip is held at high

positive voltage and they hit the surface and diffuse. As the electrons diffuse they lose their kinetic energy and this energy is transformed into thermal energy. When the tip is heated the oxide layer and/or any contaminants on the tip evaporates. This is concluded from the fact that the pressure of the chamber rises during the EB process. One can easily show that this pressure rise is not due to the heating of the filament. For a given EB cycle the maximum chamber pressure is always noted. Initially this maximum pressure can be as high as 10^{-8} Torr. It is generally found that this maximum pressure decreases from cycle to cycle, evidence that the tip is getter cleaner and cleaner.

The electron bombardment is performed in the same stage as the field emission is. Using a UHV compatible electrical feed-through and a high voltage supply the tip is held at +400 V. The maximum pressure of the chamber and the current produced in the EB process is being monitored as well. The EB current is usually held at 5 mA for 5 seconds. It has been determined from experience that holding the EB process for longer time intervals, such as 10 seconds, results in the tip dropping copious amounts of material while scanning the surface during STM studies. After each EB process the FE test is performed on the tip in order to check the improvement. The EB process is repeated for 3- 4 times to see if the tip passes the FE test. If not, the tip will not be used and we proceed to use another tip. Each time the EB process is performed on a tip, the tip is mechanically rotated by ~ 45 degrees so that all sides of the tip get bombarded and the cleaning is uniform.

It should be noticed that repeating the EB process too many times results in a blunting of the tip. The reason is that when the tip heats up by the electrons the atomic arrangement on the top of the tip can change resulting in making the tip dull rather than sharpening the tip.

2.5.2 Sharpening Tips by Electric Field

There is an alternative to electron bombardment for tip sharpening, which uses high electric fields around 2-3 kV. This method was not used to sharpen STM tips. The theory behind this method, is as follows [30, 31]; when high voltage is applied to a tip, the high field emission current heats the tip and atoms can rearrange. In the presence of high electric field, there will be a strong field gradient along the surface of the tip. This strong field gradient makes the atoms diffuse from low electric field areas to high electric field areas. Because of the curvature of the top of the tip, the end of the tip has the maximum electric field. Because of this atoms will diffuse from surface of the tip to its apex causing a sharp protrusion at the apex. This method works very well in sharpening tungsten tips with (111) orientation [30, 31].

2.6 Summary

In this chapter the preparation of STM tips was explained. A detailed discussion of the field emission current process (Fowler-Nordheim formula) for low and room temperature was explained. The field emission current density was calculated numerically and was compared to the results by Dolan [26]. Fowler-Nordheim plots were made using tips that

were electrochemically prepared. From the F-N plots the radius of each tip was estimated. A simple test (FE test) was explained to test the sharpness of the tips before being used in the STM experiments. The procedure for cleaning the fresh tips that have an oxide layer was explained. Using sharp tips, high quality images will be analyzed for studying dissociation of molecules on silicon surfaces using STM in the proceeding chapters.

Chapter 3

Si(111)-7x7 Surface and Atomic Chlorine Adsorption

In this chapter the atomic and electronic structure of the Si(111)-7x7 surface is first explained. Then the adsorption of atomic chlorine is reviewed. A detailed review of the appearance in STM images and the tip-induced diffusion of atomic chlorine is given. Atomic chlorine on Si(111)-7x7 is a simple system as compared to a molecule on this surface.

3.1 Atomic and Electronic Structure

The accepted model for the reconstructed Si(111)-7x7 surface is the dimer-adatom-stacking fault (DAS) model, which was proposed by Takayanagi et al [35] as shown in Figure (3-1).

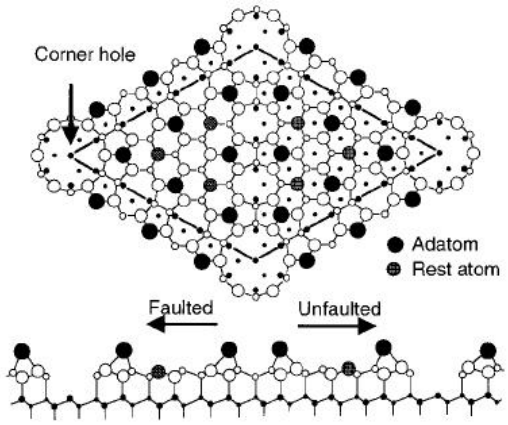

Figure 3-1 Atomic structure model for Si(111)-7x7 "dimer-adatom-stacking fault" top and side view (Diagram taken from Ref. [35])

In Figure (3-2) a layer by layer buildup of this structure is shown [36].

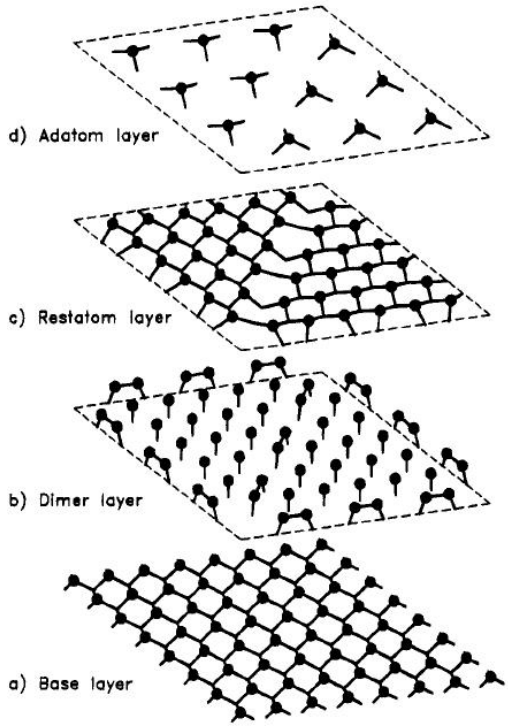

Figure 3-2 Layer by layer construction of Si(111)-7x7 structure. a) (1x1) unreconstructed (bulked terminated) surface b) first layer, the dimer layer; c) second layer, the restatom layer; d) top layer, the adatom layer (Diagram taken from Ref. [36])

The DAS structure is formed on a bulk terminated Si(111)-7x7 surface ('base layer') which has one dangling bond per atom. This layer is shown in Figure (3-2 a). The first layer in this structure is the 'dimer layer'. This layer is formed by atoms saturating the dangling bonds on the base layer. Between the two halves of the unit cell as well as

along the boundary of the unit cell, dimers form, connecting the missing atoms, Figure (3-2 b). It can be seen that on the corners of the 7x7 unit cell on this layer there are atoms missing, which are called “corner holes”. These corner holes can be seen in a typical topography STM image and can be used to easily identify the unit cell. The distance between corner holes is 2.69 nm. Each dimer atom has two dangling bonds, and the other atoms on this layer have three dangling bonds. The atoms on the next layer, in order to saturate these dangling bonds, must form a stacking fault within one half of the unit cell. This layer is called the ‘restatom’ layer as depicted in Figure (3-2 c). This fault has two important consequences as far as the adatoms go. One is that they are on average physically higher by about 0.04 angstroms than the adatoms on the unfaulted half of the unit cell [37, 38].

The other is that there is charge transfer from the unfaulted to the faulted half of the unit cell, resulting in a difference in electronic structure. In particular the local density of states on faulted adatoms is higher (lower) for occupied (unoccupied) states than for unfaulted adatoms [39]. This difference in electronic structure of two sides of the unit cell causes the STM contrast between the two halves in occupied states images (faulted half of the unit cell is imaged ~0.04Å above the unfaulted half of the unit cell at -2.0 V [14, 37, 38]).

On the rest atom layer there are 21 dangling bonds perpendicular to the surface. The best way to saturate these dangling bonds in order to minimize the surface energy is by using 12 adatoms on top of this layer, ‘adatom layer’, as shown in Figure (3-2 d). In this

configuration three dangling bonds are left intact on the rest atom layer in each half of the unit cell. On the adatom layer six adatom dangling bonds are present in each half of the unit cell.

The DAS model reduces the number of dangling bonds in the 7x7 unit cell from 49 to 19. The number of atoms in the 7x7 unit cell after the reconstruction is 4% more than the unreconstructed surface. In this reconstruction, atoms moved considerably compared to their unreconstructed configuration which causes the surface to be highly strained. Since the 7x7 reconstructed surface is the stable surface after annealing to high temperatures as proved experimentally, it can be concluded that minimizing dangling bonds is more effective at reducing surface energy than reducing strain.

The adatoms are divided into two separate types with respect to their position in the unit cell. The first type of adatom is located in the corner of the unit cell, next to corner holes, and these are called corner adatoms. The second type is located in the center of the edges of the unit cell, and these are called center adatoms.

The position of the restatoms, center adatoms and corner adatoms in a unit cell is shown in Figure (3-3).

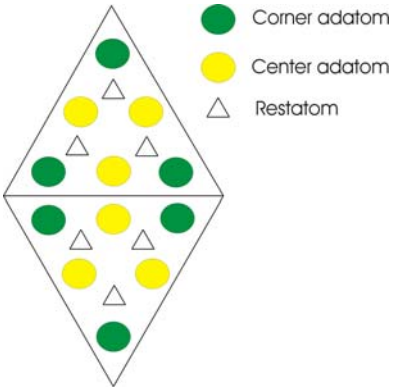

Figure 3-3 The 7x7 unit cell showing locations of corner adatoms, center adatoms and restatoms

It can be seen that the corner adatoms are adjacent to one rest adatom, and center adatoms are adjacent to two restatoms.

Due to the presence of these surface dangling bonds there are electron states localized at the surface of the silicon. These electron states are called surface states. Using Angle Resolved Ultraviolet Photoemission Spectroscopy (ARUPS) and k-resolved inverse photoemission spectroscopy four bands of surface states have been found [14]. These bands are shown in the Figure (3-4).

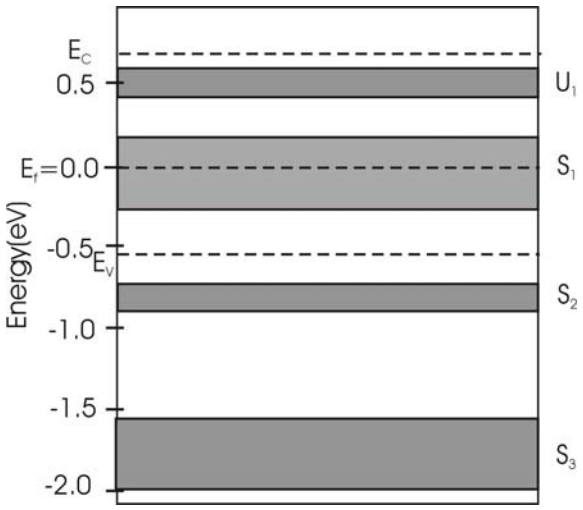

Figure 3-4 The energy level diagram for the surface states on the Si(111)-7x7 surface. The Fermi energy level E_f, Conduction band edge E_C and Valence band E_V are shown. Surface states U_1 and S_1 are located on the adatoms, S_2 is located on the restatoms and S_3 is located on the adatom backbond. The values used for this diagram are from Ref. [14]

From electronic structure calculations and experimental results, the surface state S_1 is assigned to the adatom dangling bonds, S_2 is assigned to the restatom dangling bonds and S_3 to adatom back bonds. When the surface is scanned at -0.5 V sample bias, the partially filled S_1 band is probed (occupied states). In other words the tunneling current is provided by the electrons in this state. This results in imaging of the adatoms on the surface.

When the surface is scanned at -0.8 V, the electrons in the S_2 surface state (rest atoms) are contributing to the tunneling current as well. In Figure (3-5) STM image of occupied states at -0.8 V sample bias is shown.

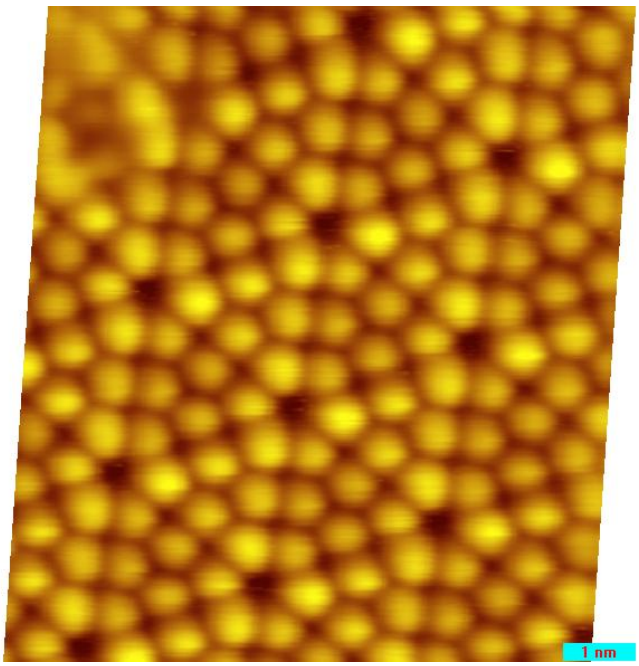

Figure 3-5 STM topographic image of Si(111)-7x7 surface of occupied states at sample bias -0.8 V and 1.0 nA tunneling current

The contribution from the S_1 electrons is more than from the S_2 electrons which causes the adatoms to dominate the image. In other words the tunneling current from the adatom dangling bonds saturate the tunneling current, hiding the restatom features. This is because tunneling through the adatoms has a larger tunneling coefficient (since they are nearer to the Fermi level energy) as compared to restatoms.

At positive sample bias the unoccupied surface states are being probed. The tunneling current in this case is contributed by the empty states. In Figure (3-6) an STM image of unoccupied states at sample bias +1.5 V is shown. In this case all adatoms appear to have

the same height. The lack of contrast between faulted and unfaulted half-cells is a result of near cancellation of topographic and electronic structure effects.

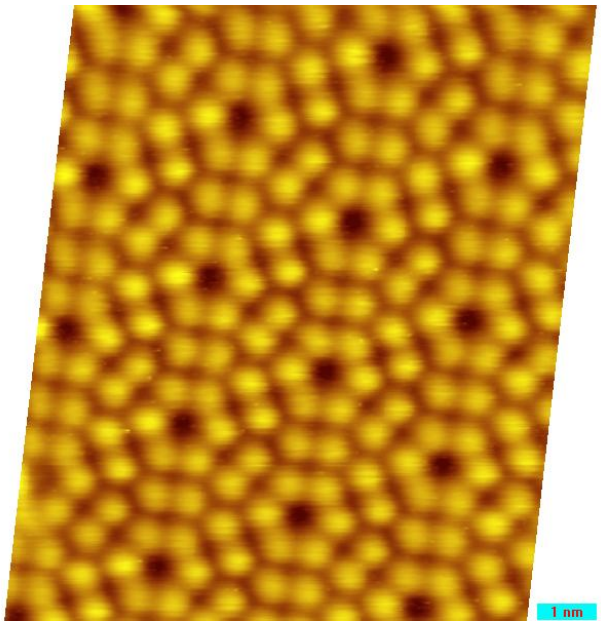

Figure 3-6 STM topographic image of Si(111)-7x7 surface of unoccupied states at sample bias +1.5 V and 1.0 nA tunneling current

From occupied states STM images, not only is there significant contrast between faulted and unfaulted half-cells, but it can also be seen that the corner adatoms appear higher than center adatoms. This is commonly interpreted as charge transfer from adatom dangling bonds to restatom dangling bonds [40, 41]. Since center adatoms are directly adjacent to two restatoms, as opposed to one for corner adatoms, there is more charge transfer to restatoms from center adatoms and therefore center adatoms appear lower in occupied state images.

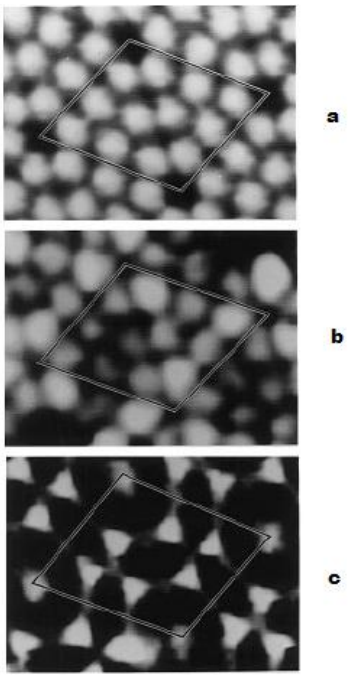

Figure 3-7 STM topography and current imaging tunneling spectroscopy (CITS) on Si(111)-7x7. a) topographic image at bias +2.0 V; b) dI/dV image at bias -0.35 V; c) dI/dV image at bias -0.8 V. The 7x7 unit cell is outlined in each image. (Figures taken from Ref. [42])

Figure (3-7a) is a normal topographic image with sample bias +2.0 V. In Figures (3-7b and c) spectroscopic images are shown. In this technique (CITS) the feedback loop is interrupted repeatedly for short durations (~0.2 ms) during the raster scan. With the feedback loop off, the sample bias is scanned over a prescribed range while the tunnel current is measured. This allows one to obtain both current maps and dI/dV maps of the surface. The dI/dV map is a very direct image of the spatial distribution of electronic

states of the surface. The dI/dV map at -0.35 V of the same area as shown in Figure (3-7 a) is displayed in Figure (3-7 b). It can be seen that the six corner adatoms are brighter than the center adatoms (as discussed earlier). The six adatoms on the faulted half of the unit cell are brighter than the six adatoms on the unfaulted half. This is due to charge transfer from unfaulted half to faulted half of the unit cell [41]. In Figure (3-7 c) the restatoms are imaged at -0.8 V as expected since this bias matches the restatom energy level. Since the bias level is well below the adatom energy levels, the adatoms do not contribute and are in fact the darkest features in the image.

Similar results have been obtained at the Surface Science Laboratory at the University of Lethbridge as shown in Figure (3-8). The technique used to measure this data is slightly different from CITS: the feedback loop is always on but a ~5kHz AC ripple is added to the sample bias and a lock-in amplifier is used to measure dI/dV. See Ref. [18] for further details. The result is similar: at -0.8 V the restatoms are prominent.

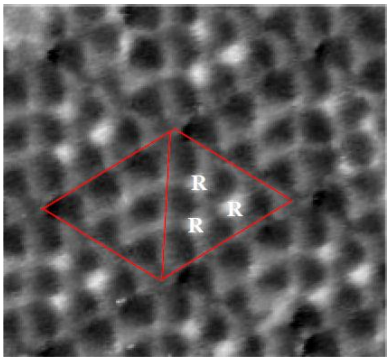

Figure 3-8 dI/dV map showing the restatom state at -0.8 eV. Three of the six restatoms in a unit cell are marked. This data was measured by Steven Horn. (Figure taken from Ref. [18])

In summary, there are four distinct adatoms with dangling bonds in the 7x7 unit cell, listed in order of decreasing electron density: faulted corner, unfaulted corner, faulted center and unfaulted center adatoms.

3.2 Chlorine Adsorption

It has been established that chlorine atoms bind directly on top of adatoms when adsorbing onto the Si(111)-7x7 surface. This can be seen directly from STM topography. Adatoms with chlorine adsorbed to them become dim relative to unreacted adatoms. This result is consistent with the loss of the dangling bond state located approximately -0.5 eV below the Fermi level. After binding two electrons are left filling a sigma bonding level located ~5 eV below the Fermi energy [43]. Since this energy lies well below what is

accessible during typical STM imaging, this level is not imaged. It is noted that the binding energy of chlorine on Si(111)-7x7 is reported as 4.76 eV [44].

The bias dependency of the brightness of the adsorbed halogen sites has also been well studied. On Si(111)-7x7 the adsorbed chlorines are imaged bright (dim) at above (below) ~+1.5 V sample bias compared to unreacted silicon adatom [45-48]. This can be seen in Figure (3-9).

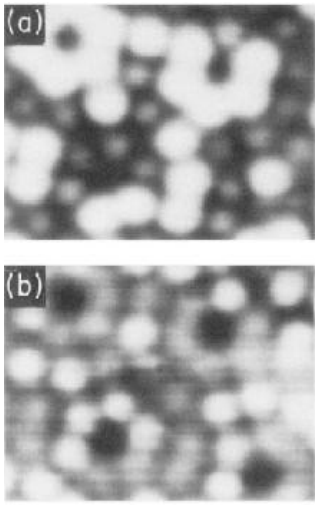

Figure 3-9 Topographic STM image of the same area of a reacted Si(111)-7x7 surface to atomic chlorine at sample bias a) +1.5 V; b) +3.0 V. The adatoms that appear dark in (a) appear bright in (b). (Figure taken from Ref. [48])

The accepted reason for this has to do with the σ^* anti-bonding of chlorine which lies near the Fermi energy level [49] . Above +1.5 eV sample bias the tip receives tunneling electrons from the tail of this anti-bonding state. When added to the topographic effect

(i.e. the sigma star states are located further out from the surface than an adatom dangling bond), the result is a bright feature in STM.

It is also known that under certain conditions the STM tip can induce diffusion of adsorbed halogen atoms on the surface. This tip-induced diffusion is known to occur at both positive and negative bias [50-52]. This diffusion of chlorine atoms on the Si(111)-7x7 surface is highly bias dependent for occupied and unoccupied states as reported by Nakamura et al [50, 51]. The bias dependency of diffusion rates of chlorine atoms at negative sample bias (hole injection) with the tunneling current of 80pA is shown in Figure (3-10).

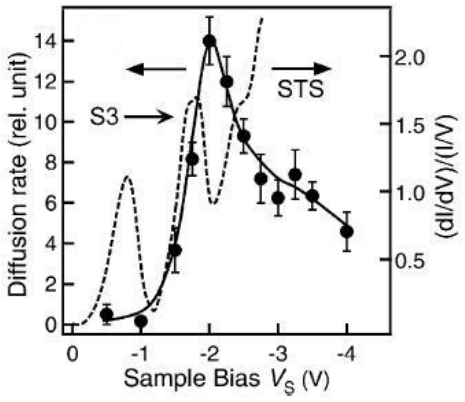

Figure 3-10 Bias dependency of diffusion rate for chlorine in negative sample bias (hole injection). The dashed line is the LDOS measured on the surface.(Figure taken from Ref. [51])

It can be seen that there is a peak at -2.0 V for the diffusion rate of chlorine and that this peak is near the S3 feature of the LDOS. The S3 surface state is derived from Si adatom backbonds. It was also reported that the diffusion rate is linearly current dependent. From this observation it is concluded that the breaking of an adatom-chlorine bond is a single-electron excitation process i.e. not a multi-excitation (ladder) type process. The other interesting fact about the diffusion of chlorine on Si(111)-7x7 is that the diffusion can occur even though the tip is not on top of the chlorine atom. This unique type of tip-induced diffusion has a range of about 10 nm or more. Most of the known tip induced manipulations of atoms and molecules reported are highly localized tip-induced diffusion/desorption/dissociation [53-56], with only one known example of non-localized diffusion, and this with a much smaller range of ~3nm [57]. The mechanism for the diffusion process of chlorines on Si(111)-7x7 surface at negative sample bias (hole injection) is explained as follows. Holes are injected into the S3 band from the tip. The holes propagate in the extended band states until they become localized at Cl bonded sites, causing instability of Si-Cl bonds. This then results in diffusion of chlorine atoms on the surface [51].

The bias dependency of diffusion rates of chlorine atoms at positive sample bias (electron injection) with the tunneling current of 80pA is shown in Figure (3-11).

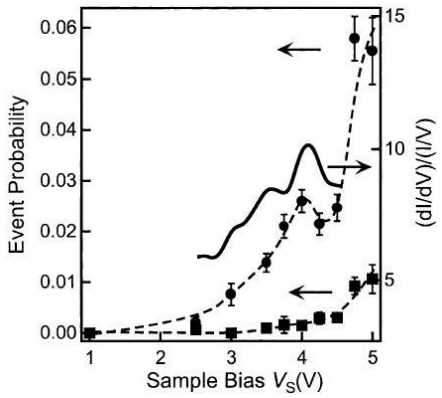

Figure 3-11 Bias dependency of diffusion (circles) and desorption (squares) event probability for chlorine at positive sample bias (electron injection). The solid line is the LDOS measured at Cl adsorbed sites.(Figure taken from Ref. [50])

It can be seen that the maximum event probability for diffusion occurs at ~+4.0 V. The peak at +4.1 V is absent in the LDOS on the clean Si(111)-7x7 surface, indicating that this peak corresponds to the Si-Cl anti-bonding feature. The diffusion probability of the chlorine atoms is linearly dependent at positive sample bias as in the case of negative sample bias. The mechanism for the diffusion process of chlorines on Si(111)-7x7 surface at positive sample bias (electron injection) is explained as follows. Electrons are injected into backbond anti-bonding states of the Si(111)-7x7 surface from the tip. The electrons in the band state diffuse along the surface without losing energy until they are localized resonantly at the Si-Cl antibonding σ* state (located at +3.7 eV). The Si-Cl

bond becomes destabilized and this leads to Cl diffusion or desorption from the surface [50].

3.3 Summary

In this chapter a detailed discussion on the atomic and electronic structure of the Si(111)-7x7 reconstructed surface was given. The chemical and electronic properties of atomic chlorine on this surface were reviewed. Atomic chlorine bonded to an adatom has a brightness dependency with sample bias when imaged with STM. The tip-induced diffusion process of atomic chlorine was also reviewed. Now that this simple system was explained, in the next chapter more complex systems are reviewed, i.e. the adsorption and dissociation of molecules on the Si(111)-7x7 surface.

Chapter 4

Review of Dissociation of Molecules on the Silicon (111)-7x7 Surface

Although most of the silicon based microelectronics are being implemented on Si(100), the Si(111) surface has attracted lots of attention from surface science researchers. This is because: (1) It has the most thermodynamically stable crystal surface, (2) the large unit cell and unusually large corrugations make STM imaging easier, (3) the well known reconstructed surface provides a rich surface (binding sites with variety of electron charge densities) for studying chemical reactions [42].

In this chapter a review is given on the interaction of ammonia, dimethylamine and trichloroethylene on this surface using different surface analysis techniques (Appendix B provides a brief summary of selected surface science measurement techniques).

4.1 Dissociation of Molecules

The dissociation of molecules on surfaces is one of the important aspects of surface science studies. The studies in this area will aid our understanding of bond cleavage barriers in molecules (which are not always thermodynamically favorable). STM has a big advantage over other surface analysis methods since it provides information on the atomic scale on both geometric and electronic structure. As discussed previously, binding sites on the Si(111)7x7 surface have different structures and electronic properties

(charge density). This difference in binding sites may result in preference for the products of molecules that dissociate on the surface. At this scale STM is the best candidate for probing each binding site and understanding how these dissociated parts spatially distribute on an atomic scale.

Using STM in constant current mode (topography) the local electronic structure on the surface near the Fermi level ~ ±4 eV can be probed [58]. At higher biases the tunneling current will not be from the surface states only, but bulk states will contribute as well. One can not simply identify the atoms attached to the surface since, from the photoemission data, the binding energies of the adsorbates are usually further than the STM tunneling range. For this reason STM images should be accompanied by other indirect measurements of the surface, such as vibrational spectroscopy (electron-energy loss (EELS)) and photoemission spectroscopy, to give a better view of the dissociation process. For example, the EELS data will indicate what kinds of adsorbates are present at the surface and approximately with what ratio. The rest relies on the researcher to distinguish from STM images the products of the dissociation, how they bind to the surface, what is their preference for binding sites on the surface, etc.

4.1.1 Dissociation of Ammonia

One of the earliest STM works on the dissociation of molecules was the study of ammonia on Si(111)7x7 by Wolkow and Avouris [58, 59]. The ammonia molecule is shown in Figure (4-1).

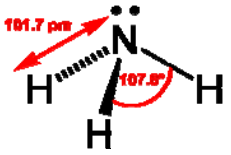

Figure 4-1 Ammonia molecule

The earlier works using EELS [60] and photoemission [61] spectroscopy reported that NH_3 reacts with the surface through a dissociation process, with Si-H and Si- NH_2 species being present on the surface. Figure (4-2) is the STM topography image of the Si(111)7x7 surface after the ammonia exposure (~2L) at two different biases. The dose delivered onto a surface is measured in units of Langmuirs. One Langmuir is 10^{-6} $Torr \cdot sec$.

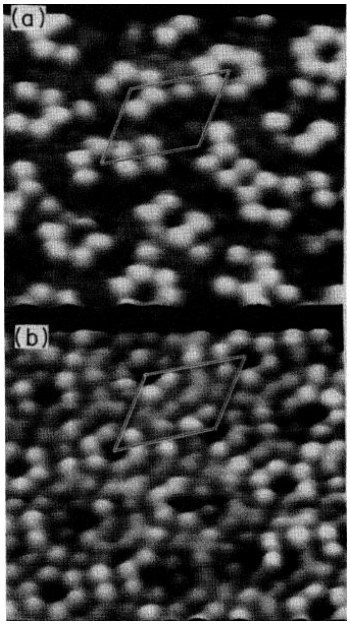

Figure 4-2 STM topographic image after ~2L exposure to NH_3 a) bias +0.8 V; b) bias +3.0 V. (Figure taken from Ref. [59])

Figure (4-2a) is the topography at the sample bias of +0.8 V. Almost half of the adatoms have vanished. It appears as though the surface has been etched by the NH_3, but from the EELS data this interaction is a dissociative process. By increasing the bias to +3.0V it is observed as in Figure (4-2 b) that the vanished adatoms become bright again. This indicates that there is no etching reaction. The vanishing of adatoms at +0.8V is an indication of a change in electronic structure of the adatoms which is caused by the interaction of the dissociated parts of NH_3. With this information it is known that the vanished adatoms must be the ones that interacted either with NH_2 or H. The binding energy of these parts with adatoms are about 4 eV[61] and ~6eV[62] on Si(111)7x7 respectively, which is higher than $E_f \pm 4$ eV, so it is not possible to identify them using STM. The center adatoms are more reactive than corner adatoms by a ratio of ~3.5 for ~1 L exposure.

Restatoms are physically lower than adatoms which makes them difficult to image. Tunneling spectroscopy, which is measuring $(dI/dV)/(I/V)$ at binding sites, gives more information about electronic structure of restatoms. This quantity is approximately proportional to the local density of states (LDS) [9]. Figure (4-3) shows the topography and tunneling spectra of a clean and exposed surface.

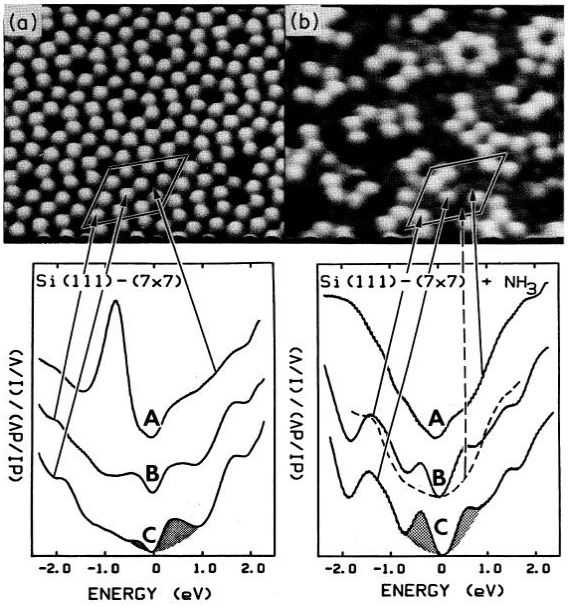

Figure 4-3 STM topography of unoccupied states and atom resolved tunneling spectra (below) of a) clean Silicon surface; b) exposed to NH_3; curve A is the spectrum of restatom, curve B is for corner adatom and C is for center adatom (Data taken from Ref. [59])

The spectrum A is on a restatom, B on a corner adatom and C on a center adatom. By looking at the intensity of the spectrum A, one can see that the restatom is almost fully occupied and has a characteristic feature at ~-0.8 eV. Spectrum B for the corner adatom shows an occupied band at ~0.4 eV below the Fermi energy and one unoccupied band at ~0.5 eV above the Fermi energy. Spectrum C for the center adatom is different from the

corner adatom. The intensity of the occupied dangling bond is reduced relative to the corner adatom.

Considering the restatom bond to be filled, one can think of charge transfer (CT) occurring from center adatom to restatom. As explained in section 2.2, center adatoms are adjacent to two restatoms while corner adatoms are adjacent to one restatom. There is more charge transfer from a center adatom to restatoms than there is from a corner adatom.

Looking at Figure (4-3b) it is obvious that the peak at -0.8 eV for the restatom disappears for a reacted restatom. Using this method it is found that the restatoms are completely occupied (reacted). This is surprising because the restatom dangling bond is full and NH_3 has a lone pair of electron. For the spectrum B in Figure (4-3b) the dashed line is when the center adatom is reacted. It is seen that the characteristic features at occupied and unoccupied states are gone. This is the reason for not seeing them in topography after interacting with NH_3. The solid lines in Figure (4-3b) are for a condition that the restatom is reacted, and the corner and center adatoms are unreacted. It can be seen that the center adatom spectrum becomes similar to the corner adatom spectrum as if the charge that had been transferred from center adatom to restatom is transferred back. This suggests that during the interaction of the restatom a reverse charge transfer from restatom to corner adatom occurs, which decreases the charge density on the restatom and now the restatom is ready to react with the NH_3.

The reason for center adatom preference might be in the difference in electronic structure between corner and center adatom. But as shown earlier, after the interaction of restatom with NH_3 and reverse CT process, the electronic charge distribution of the adatoms become similar. Another reason can be based on statistics. The products of dissociation of NH_3 require two binding sites: one for H and another for NH_2. Since the restatoms are completely reacted and there are two center adatoms near each restatom, the ratio of 2:1 is expected between center adatom to corner adatom. This ratio is actually about 4:1. This high site selectivity towards the center adatom is assigned to the lower strain produced in the dimer bonds in the DAS model. This is because reaction of a corner adatom will strain two dimer bonds, while reaction of a center adatom will involve only one dimer bond.

More recent photoemission studies have confirmed the dissociation of the NH_3 molecule [63]. In addition the results of Wolkow and Avouris [58, 59] were confirmed by the recent STM and STS study by Wu et al [64].

4.1.2 Dissociation of Dimethylamine

As discussed earlier about the reconstruction of the Si(111)7x7, the driving force for this complex reconstruction is minimizing the dangling bonds on the surface. This reconstruction leaves 19 dangling bonds on the surface. The chemistry of the surface because of the existence of dangling bonds is derived by making the silicon atoms on the surface achieve 4-fold coordination.

The chemistry of the N-containing molecules is controlled by the lone pair on the nitrogen. Like the NH_3 molecule, these kinds of molecules make a dative bond to the binding site. The dative bond requires a binding site with a low charge (electron) density since the dative bond is formed when the lone pair is donated to the binding site with lower charge density. As in the case of the NH_3 molecule the restatom would get rid of the extra charge by an inverse CT process to the corner adatom before accepting the dative bond (binding).

Figure (4-5) is the topography STM image [65] at -1.6 V sample bias of the surface after 0.01L exposure to dimethylamine (C_2H_7N). The dimethylamine molecule is shown in Figure (4-4).

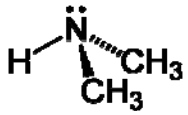

Figure 4-4 Dimethylamine molecule

The 7x7 structure of the surface is preserved after the exposure. It can be seen that there are two features on the surface 'A' which are bright and 'B' which are dark. Both features are reported to prefer binding to center adatoms. Again from the STM image it is difficult to identify the species on the surface.

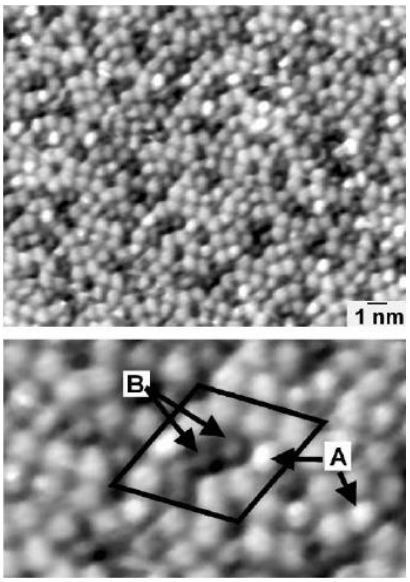

Figure 4-5 STM topographic images of dimethylamine (DMA) exposed (0.01L) surface at -1.6 V bias (Figure taken from Ref. [65])

To identify the chemical species on the surface, photoemission spectroscopy (XPS) was performed on the exposed surface. The N(1s) spectrum was characterized by a large narrow peak at 399.1 eV, with a tiny peak near 401.2 eV, on a 10L exposed surface. This binding energy of the N(1s) peak is close to the binding energies of dissociatively adsorbed ammonia, pyrrolidine, aniline and DMA on Si(100)-2x1. In all the above mentioned molecules ammonia reacts with the surface after the N-H bond had cleaved, leaving the N atom with 3-fold coordination. It can be concluded that the peak present in the N(1s) spectrum is for the N from the DMA molecule having 3-fold coordination, but it is not known whether H or CH_3 dissociates from the molecule. The XPS spectrum for C(1s) does not show any peak near 284.1 eV, caused by Si-CH_3 species as previously

reported [66]. This indicates that the H dissociates from the DMA molecule. From STM images it is known that the preference for binding is center adatoms. This suggests that before the dissociation of the DMA molecule, the molecule forms a dative bond to the center adatom and then the cleavage of N-H happens. Since the center adatoms are more positive relative to the corner adatoms by having less electron charge due to CT to restatoms, they are the preferred site for the initial dative bond by DMA molecule. Although cleavage of the N-C bond results in more favorable products (thermodynamically), the N-H bond cleaves. The preference of N-H being cleaved compared to N-C is because after the DMA molecule forms the dative bond to the surface (because of the nature of the dative bond) electrons are withdrawn from the N (lone pair). This makes the barrier for the cleavage of N-H lower than the cleavage barrier for N-C [66]. Similar results have been reported for organic amines as well.

The result of reaction can be seen on adatoms using STM topography, but as we know restatoms play an important role in the reaction as well. An example is the reaction of ammonia with the Si(111)-7x7 surface. The imaging of restatoms is challenging because of their location (one layer under the adatom layer). Cao et al [65] used UPS to analyze the surface after exposure to see how the adatoms and restatoms react with the DMA molecule. This is because with UPS experiment one can determine which electronic states of the surface are involved. On the clean Si(111)-7x7 surface the surface states at 0.2 and 0.8 eV in UPS spectrum are assigned to adatom and rest atom states [67]

respectively. The state at 1.8 eV is assigned to the adatom backbonds [68]. Figure(4-6) is the UPS spectrum of the clean and exposed surface [65].

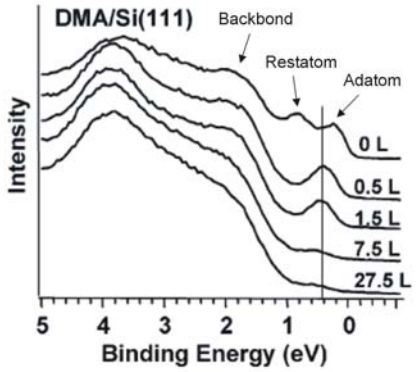

Figure 4-6 UPS spectrum of clean and exposed Si(111)-7x7 surface (Data taken from Ref. [65])

It can be seen that after the 0.5L exposure the intensity of adatoms as well as restatoms decreases. The interesting thing is that the intensity of restatoms decrease quicker than the adatoms, indicating that the restatoms react quicker than the adatoms. The reasons for this can be the CT processes similar to the interaction of ammonia on this surface [58, 59]. A second reason can be based on statistical reasons, as there is half the number of restatoms as adatoms in a unit cell. When dissociation happens, the dissociated parts need two binding sites so the restatom dangling bonds will be completely quenched while there are still adatom dangling bonds left.

Furthermore it is seen that the peak for the adatoms shifts from 0.2 eV to 0.4 eV after dosing. A high resolution UPS study [69] on Si(111)-7x7 surface showed that there are two states at 0.15 and 0.5 eV for center adatom and corner adatom respectively, so it is concluded that the adatom sites involved in this reaction are the center adatoms. This result is consistent with the STM results which indicated that the preference for the binding sites is for center adatoms.

Using the XPS and UPS information, the STM images can be analyzed better. The overall interaction of the dimethylamine with Si(111)7x7 surface is of dissociative form with a dative bond as an intermediate stage. One species on the surface is Si-$N(CH_3)_2$, which is an N containing molecule with N having 3-fold coordination, bonded to the center adatoms. The other species is Si-H, where H is dissociated from the DMA molecule and binds to either restatom or adatom. This behavior is very similar to the behavior of the same molecule on Si(100) surface [66]. Now going back to the STM images the B features which are dark can be assigned to adatoms that have interacted with hydrogen. This is because from previous studies we know that hydrogen terminated adatoms are dark in this range of bias [70, 71]. Since the preference of binding sites for bright features (A) are center adatoms, they can be assigned to the $N(CH_3)_2$ species (UPS results show strong interaction of center adatoms).

In conclusion it is understood how the dative bond formation controls the interaction of the DMA molecule on Si(111)7x7 (which includes the delocalization of the lone pair

electron of N to the silicon surface). The studies show a similar interaction process for amines on the Si(111)7x7 [65] surface as for the Si(100)-2x1 [66] surface.

4.1.3 Dissociation of Trichloroethylene

Simple chlorinated hydrocarbons such as monochloroethylene (C_2H_3Cl) are ideal samples because of their simplicity. By studying their reactions with surfaces, information about their reaction processes and the surface structures that are built after adsorption can be understood. In the semiconductor industry halogenated hydrocarbons are used extensively. For example, in order to reduce the hydrogen content and to improve the microstructure of silicon carbide films, perchloroethylene (C_2Cl_4) and trichloroethylene (C_2HCl_3) are used as precursor gasses in SiC alloy formation by electron cyclotron resonance chemical vapor deposition [72]. As another example, trans-dichloroethylene and trichloroethylene (TCE) are used as Cl sources to reduce metal contamination during Si oxidation[73, 74].

The reaction of such molecules has been investigated considerably on metal surfaces [75-77] using near edge X-ray absorption fine structure (NEXAFS), thermal desorption spectroscopy (TDS), photoemission (UPS) and vibrational electron energy loss spectroscopy (EELS). The interaction of chlorinated unsaturated hydrocarbons with silicon surfaces has been studied recently using EELS, XPS and TDS by Leung's group[78-83].

The trichloroethylene molecule is shown in Figure (4-7).

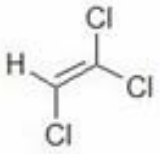

Figure 4-7 Trichloroethylene molecule

Figure (4-8) is the EELS spectrum of trichloroethylene for different exposures at room temperature (RT) [83].

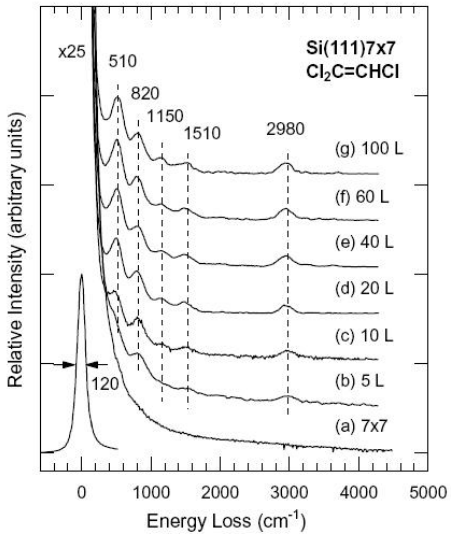

Figure 4-8 EELS spectrum for Si(111)-7x7 surface for clean and TCE exposed surface (Figure taken from Ref. [83])

The features at 1510 cm^{-1}, 820 cm^{-1} and 510 cm^{-1} are assigned to C=C, C-Cl and Si-Cl stretching modes respectively. It can be seen that C=C is intact after exposure. The Si-Cl

feature indicates the dissociation of chlorine from the TCE molecule in the adsorption process. The absence of a Si-H stretching mode near 2100 cm^{-1} indicates that the cleavage of C-Cl is a more favorable pathway for the RT adsorption of TCE on the Si(111)-7x7 surface. This is consistent with the stronger bond strength of Si-Cl (377 kJ mol^{-1}) as compared to

C-Cl (339 kJ mol^{-1}). The stronger bond strength for C-H (414 kJ mol^{-1}) compared to Si-H (314 kJ mol^{-1}) further supports the preference of the C-Cl cleavage for the TCE molecule. From the above mentioned information, the overall picture that can be concluded is that the adsorption is of dissociative form. Chlorine dissociates from the molecule and binds to the surface. With the C=C double bond intact, the rest of the molecule which is 2,2-dichlorovinyl ($H\dot{C}=CCl_2$) and 1,2-dichlorovinyl ($Cl\dot{C}=CHCl$), forms a mono σ bond on the surface as shown in Figure (4-10 b I,II).

Figure (4-9) is a TDS spectrum of a 100L TCE exposed silicon surface [83] for mass 130 ($C_2HCl_3^+$) which is the parent mass, mass 98 ($SiCl_2^+$), mass 63 ($SiCl^+$), mass 60 (C_2HCl^+) and mass 35 (Cl^+).

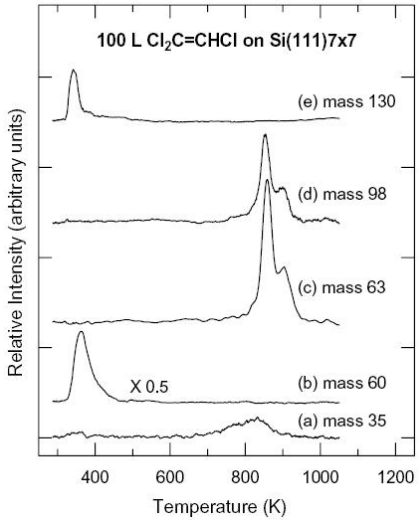

Figure 4-9 TDS spectrum of Si(111)-7x7 surface exposed to 100L of TCE for specific masses (Figure taken from Ref. [83])

One interesting issue about this spectrum is the desorption of the parent mass at low temperatures (340 K). This low temperature desorption of the parent mass suggests a molecular adsorption process where the desorbed molecule is from the intact TCE molecule and not from the recombination of adsorbed species on the surface since for this process to happen a higher temperature is required. A reasonable binding configuration for the molecular adsorption can be explained by a dative covalent binding between the chlorines of the TCE molecule and the Si dangling bonds. This is because of chlorine's inductive effect. This binding is shown in Figure (4-10 a).

From the EELS and TDS studies the interaction of the TCE molecule with Si(111)-7x7 occurs within two pathways. The *minor pathway*, which is the molecular adsorption of

TCE, which involves dative bonding from the chlorines to the silicon dangling bonds (adatom and restatom) is shown in Figure (4-10a). The *major pathway* involves dechlorination of the TCE molecule causing a mono σ bond between 2,2-dichlorovinyl (Figure 4-10 bII) or 1,2-dichlorovinyl (Figure 4-10 bI) with silicon adatom dangling bond.

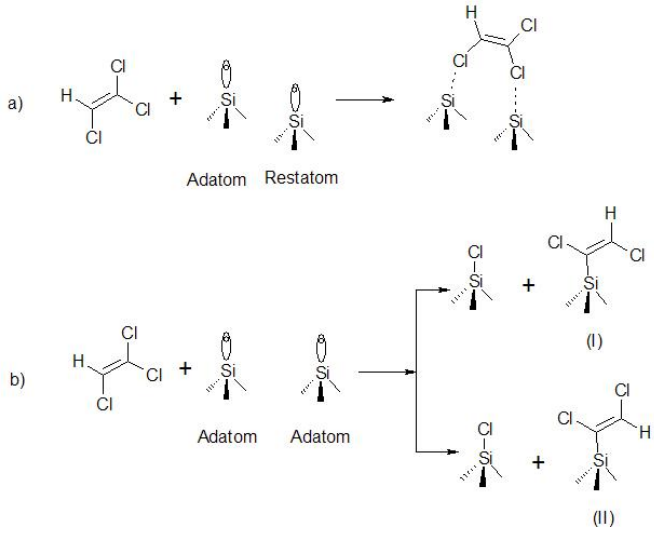

Figure 4-10 Schematic diagram of plausible adsorption structures a) minor pathway; b) major pathway

4.2 Summary

The interaction of ammonia, dimethylamine and trichloroethylene on the Si(111)7x7 surface was reviewed. Using different surface analysis methods such as XPS, UPS, EELS, TDS and STM it was shown that these interactions were of dissociative form on

the Si(111)-7x7 surface. In the following chapter, STM work on the dissociation of TCE will be presented.

Chapter 5

STM Study of Trichloroethylene on Si(111)-7x7

As discussed in section 4.1.3, previous EELS and TDS studies of molecules on Si(111)-7x7 have revealed valuable information about the chemical bonds formed on this surface. However, the information obtained by these experiments is indirect, is averaged over large surface areas, and can be complicated by adsorbate-adsorbate interactions as these studies are commonly performed at high coverage. To obtain direct and atomic-level information about the reacted sites, such as preference for particular binding sites, changes in reconstruction, changes in the local density of states (LDS) of the reacted sites etc. on this complicated and unique Si(111)-7x7 surface, the atomic resolution property of STM was used. In particular, one can use STM to ask questions related to how the various types of adatoms, restatoms, corner holes etc. can affect the dissociation of a molecule and the way that the products bind to the surface.

After introducing the ultra high vacuum (UHV) system, a detailed procedure used to prepare a clean Si(111)-7x7 surface is explained. This is followed by a report of STM studies of the interaction of TCE with the Si(111)-7x7 surface [84]. Techniques used to characterize the dissociation products will be explained in detail. Coupled with previous work on this system [83] a fairly complete picture of the dissociation process will be presented.

5.1 UHV System

The base pressure of the STM chamber is better than $3x10^{-11}$ Torr. A 300 L/sec ionization pump and two titanium sublimation pumps (TSP) have been installed in the chamber to obtain and maintain UHV. STM tips and samples are transferred into the chamber through a load-lock (to prevent contamination of the main chamber) which can reach high vacuum when pumped down by a 60 L/s turbo molecular pump. When the valve between the load lock and the main chamber is opened for brief periods of time the pressure of the main chamber reaches $\sim 5.0x10^{-8}$ Torr.

The procedure of obtaining UHV (from a vented chamber to atmosphere) in the main chamber is through stages. The turbo pump is used to pump down the chamber to $\sim 10^{-7}$ Torr. At this pressure range the ion pump is turned on and the valve between the main chamber and load-lock is closed. TSP pumps are also fired to lower the pressure. The TSP pump operates by coating the walls of the chamber by titanium which is very reactive. The gas molecules inside the vacuum chamber react with the titanium and condense into the solid state. The advantage of the ion pump is the capability of pumping out noble gases. The TSP is capable of pumping hydrogen which is difficult for an ion pump to ionize. The combination of TSP and ion pump makes a very efficient pumping system.

After these steps are taken the pressure of the chamber will reach $\sim 10^{-9}$ Torr. The pressure is still rather high because molecules (mainly water and some other molecules such as nitrogen, propane, methane and oxygen) remain adsorbed to the inner walls of the

chamber and are still outgassing. To remove these molecules from the inner walls (outgas) and getter them with the ion pump and the TSP pump, the chamber walls are heated to ~130 °C for two days. The walls of the chamber are heated using heat tapes and it is covered by aluminum foil so that the heat is distributed evenly. After the chamber is cooled down, the pressure is in the ~10^{-11} Torr range.

It should be noted that the base pressure of the chamber was ~1.3×10^{-10} Torr when there was both an ion pump and just one TSP pump operating. To further lower the base pressure the second TSP pump was designed and installed in the chamber. After the installation of the second TSP the base pressure was better than 3×10^{-11} Torr (the limit of the ion gauge in the chamber). This was because the second TSP would coat more surface area of the chamber with titanium thus pumping much more residual gas.

For determining the molecules present in the chamber, the residual gas analysis using a VG mass spectrometer was performed at a pressure of 8.1×10^{-11} Torr. Figure (5-1) shows the mass spectrum of the residual gases in the chamber.

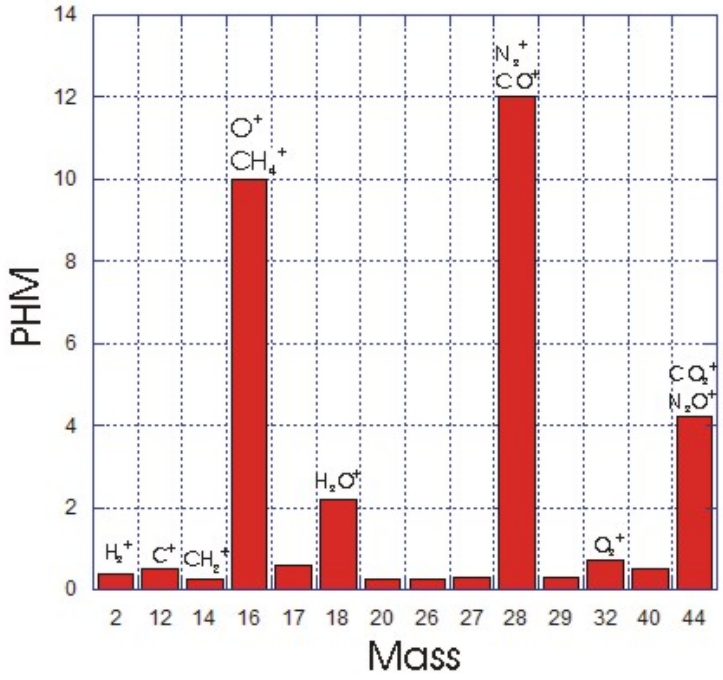

Figure 5-1 Mass spectrum of residual gases in the chamber at 8.1×10^{-11} Torr. The mass scale is in units of amu. The y-axis was Peak Height Maximum (PHM). Masses left off the x-axis had readings at the noise limit.

The data from the mass spectrometer was interpreted using RGA version 3.005 of Stanford Research Systems (SRS). From Figure (5-1) it can be seen that N_2, CO, CO_2, O_2 and CH_3 are the main residual gases present in the chamber.

5.2 Preparing the Clean Si(111)-7x7 Surface

In order to perform STM studies on surfaces before and after dosing, the surfaces should be as clean as possible, as defects or disorder on the surface makes it harder to understand the behavior of the molecules on surfaces. In particular it is important to find a reproducible method for cleaning a surface. For this reason, different procedures have been tested. In each procedure the parameters of the procedure have been adjusted, mainly by trial and error, until a desirable result was obtained. In this section the procedure that was used in order to prepare clean surfaces of Si(111)-7x7 is discussed.

5.2.1 Cleaning Procedure

Silicon wafers with 75 mm diameter, 356-406 um thickness, (111)-orientation, n-type doping, 0.02-0.05 ohm·cm conductivity, were purchased from Montco Silicon Technology. Samples with dimensions of 1.5 mm x 12 mm were cut from the wafer and mounted in the sample holder. During cutting and mounting procedures, the silicon sample is not touched by any nickel-containing materials (in particular stainless steel) since it has been reported that the presence of even trace amounts of nickel leads to disorder of the atoms on the surface [85]. The cleaning procedure consists of two stages. First is the ‘wet chemical process’ and the second is a ‘heating process’.

5.2.1.1 Wet Chemical Process

For this stage the well known RCA clean procedure [86] was used, which was proposed by Werner Kern of RCA Laboratories. This process eliminates the organic

contaminations (especially carbon) from the surface of the silicon and leaves a thin oxide layer on the sample.

The recipe for the RCA clean is 5-1-1 parts by volume, of water (H_2O)-hydrogen peroxide (H_2O_2)-ammonium hydroxide (NH_4OH). The procedure is as follows.

A bath of water at a temperature of ~75 °C is prepared. The solution as mentioned above is prepared in a clean Pyrex beaker and the beaker is placed in the bath until bubbles are produced in the beaker. At this point the silicon samples are placed in the solution and kept in the solution for 10 minutes and every 2-3 minutes the solution is swished. During the process a lot of bubbles are produced near the silicon samples. After this the solution is diluted with clean water 10 times while keeping the silicon sample in the solution so that it is not exposed to air. The samples are kept in water and are blown dry with dry N_2 before being mounted in the sample holder and transferred to the loadlock of the UHV chamber.

This solution was prepared because the organic contaminations are attacked by the powerful solvating property of ammonium hydroxide and the powerful oxidizing property of the hydrogen peroxide. Hydrogen peroxide solutions at high pH (caused by ammonium hydroxide here) are especially effective at oxidizing organic contaminations [86]. A bare silicon surface is attacked by even a weak base, such as ammonium hydroxide. Hydrogen peroxide on the other hand immediately passivates the surface with a thin layer of hydrous oxide so the surface of the silicon will not be continuously attacked by ammonium hydroxide. This is because the hydrous oxide layer is very

resistant to chemical reaction at the temperature and the concentration of the solution in our cleaning procedure [87]. This oxide layer serves as a protective layer against the carbon and other molecules present in the air while mounting the sample and transferring it to the UHV chamber.

5.2.1.2 Heating Process

After transferring the sample to UHV, the sample and the sample holder were outgassed and the protective oxide layer which was formed in the wet chemical process was removed using direct current resistive heating. The sample was heated at 630 °C for 12 hours overnight. During this period the sample outgasses and the temperature of the sample holder reaches 120 °C. This temperature is not sufficient to remove the oxide layer. The required temperature for the oxide layer to be removed is around 850 °C [14]. To eliminate the carbon remaining on the sample surface the sample must be heated to 1230 °C or higher. It has been reported that carbon atoms diffuse into the bulk at this temperature [14, 88]. The sample is typically held at 1250 °C for 10 seconds while monitoring the pressure of the UHV chamber to be less than $3\times10^{-10}\,Torr$ during the heating process. The sample might need 3-6 trials so that the pressure stays below the mentioned range. In this case after each flash the block that the sample holder is on gets hotter. In order to cool down the annealing block to ~10 °C, liquid nitrogen is used.

The 7x7 reconstruction forms after the sample is heated to 860 °C. This reconstruction happens very quickly [89]. The rate of cooling is an important aspect since quick cool

down will cause quenching and missing adatom defects and mis-reconstruction. Because of the missing adatom defects and mis-reconstruction, after the high temperature process, the sample is heated to 920 °C and the temperature is decreased at the rate of 0.5 °C/s to 600 °C while monitoring the pressure. This process is done when the annealing stage was cooled down to ~ 12 °C. The maximum pressure of the chamber during the slow cool would reach ~1.5×10^{-10} Torr usually. If the maximum pressure exceeded this value, the high temperature step and slow cool were performed again.

Examples of clean surfaces resulting from the above mentioned procedure are shown in Figure (5-2).

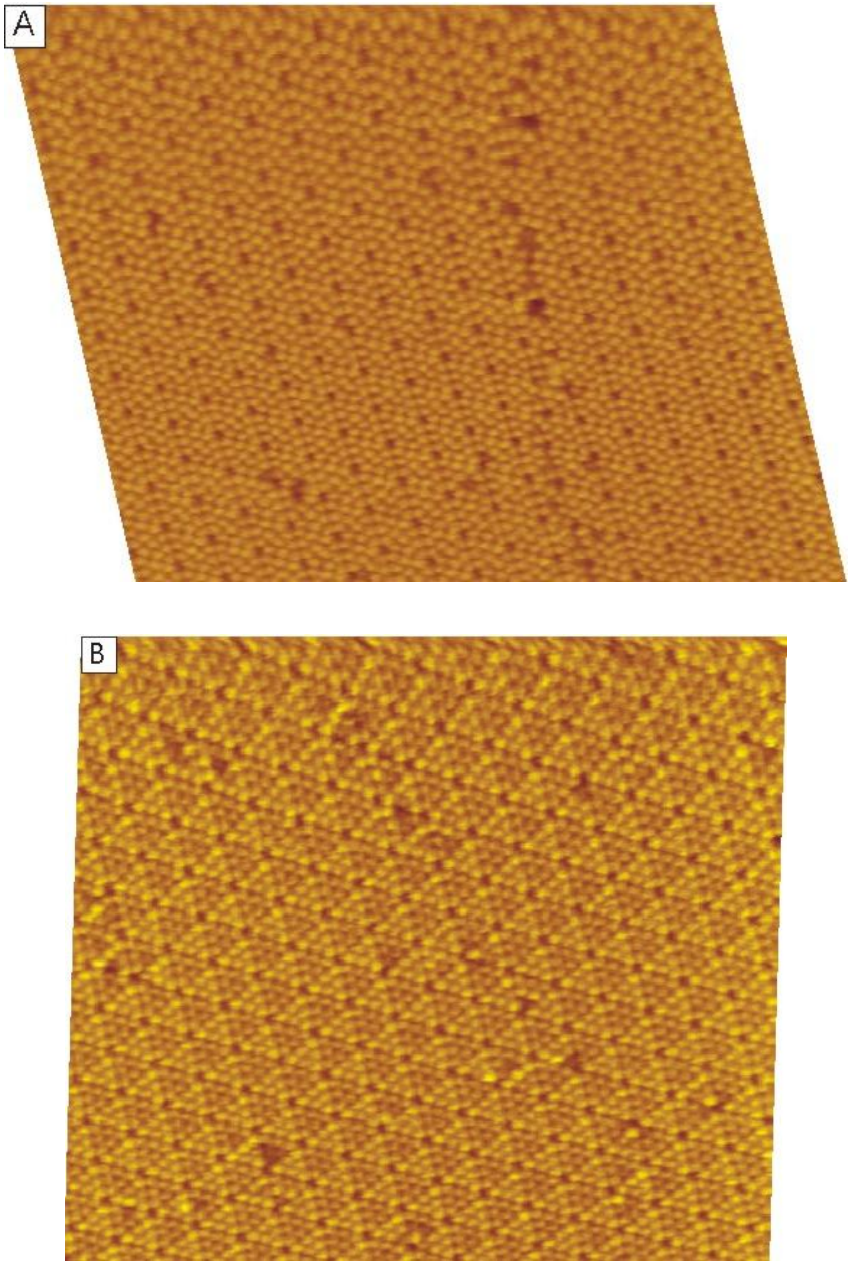

Figure 5-2 STM topography images of clean Si(111)-7x7 surface at a) sample bias +1.0 V; b) sample bias -2.0 V and 100 pA tunneling current. The corner hole to corner hole distance of 2.69 nm provides a scale.

One can see in both of these images that, even though the surface is not completely free of defects, there are nevertheless defect free areas large enough to be suitable for STM study. Adsorption of a molecule into one of these areas should give results that are virtually free from any effects that could be caused by surface defects. This allows for reproducible results for the study of that adsorbate on the Si(111)-7x7 surface that can be corroborated by other researchers. The number of defects per area is usually ~$5x10^{-3}$ defects/nm^2 for surfaces resulting from the above mentioned procedure. It was found that the critical parameter in this procedure was the high temperature that the sample is heated at, before the slow cool. Annealing temperatures below 1250 °C do not typically result in acceptable surfaces even with the same slow cool rate of 0.5 °C/Sec. As an example, Figure (5-3) shows an STM image of a sample annealed to just 1235 °C and slow cooled at a rate of 0.5 °C/s (the sample was RCA cleaned). As can be seen this surface is not as free from defects as the one shown in Figure (5-2). The defect density on this surface is $3.8x10^{-2}$ defects/nm^2. This surface has ~7 times the level of contamination that is commonly found on the surface that is annealed to 1250 °C.

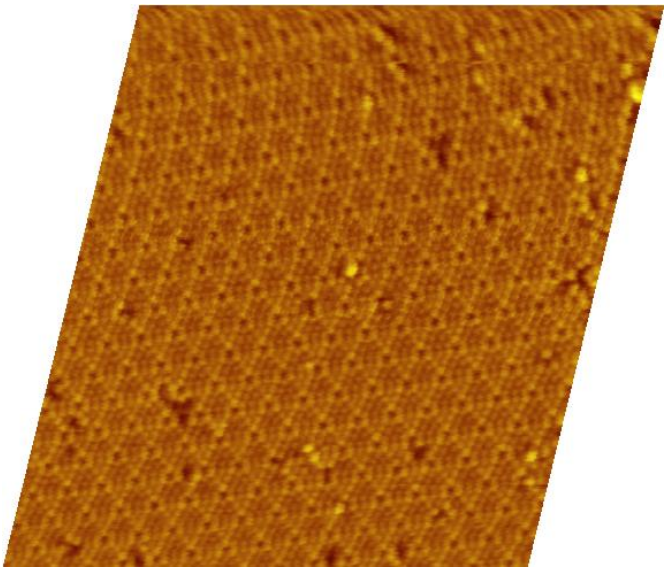

Figure 5-3 STM topography images of clean Si(111)-7x7 surface by flashing it to 1235 °C at -1.5 V sample bias

5.3 STM Study of Trichloroethylene

Reagent grade (Merck) trichloroethylene (99.5% purity) was placed in a quartz glass tube connected to a stainless steel gas line and was repeatedly degassed by freeze-pump-thaw cycles. The clean silicon sample was exposed by passing trichloroethylene (TCE) vapour into the main chamber from the gas line via a variable leak valve.

5.3.1 Identifying Chlorine

In Figure (5-4 a,b,c) the empty state STM images of the surface after exposure are presented. Figure (5-4 a and c) are images after TCE exposure of 1.1 L and Figure (5-4 b) is an image after 0.72 L (60 sec at 1.2×10^{-9} Torr) exposure. The pressure readings from

our ionization gauge were not corrected for the ionization factor of TCE molecules. Observations show that at biases in the range of +1.4 - +2.1 V the surface consists of bright features (higher than unreacted adatoms) and dark features which resemble missing adatoms (Figure (5-4 a and c)). The apparent height for the bright features in Figure (5-4 a) is 1.2 Å higher than the unreacted adatoms.

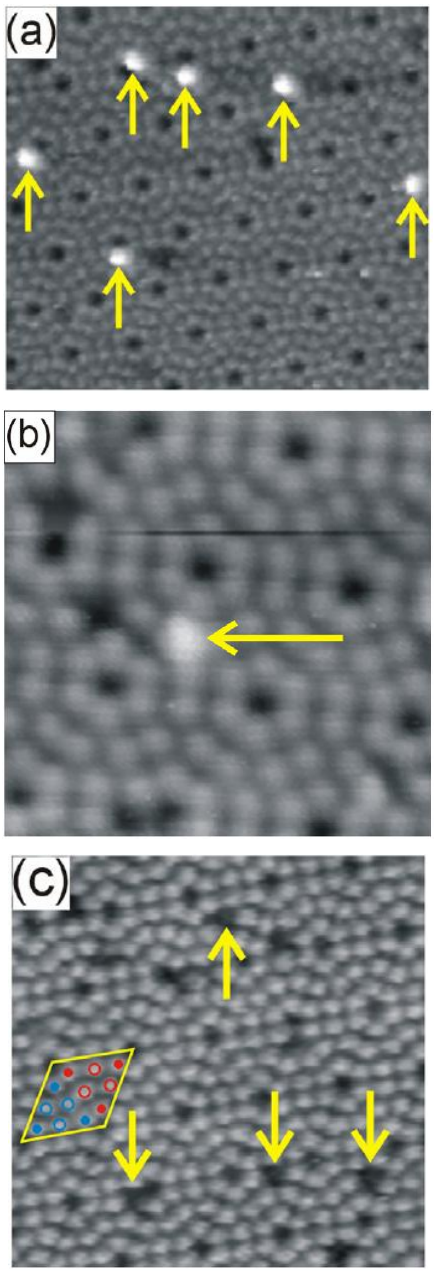

Figure 5-4 STM topographic images of the Si(111)-7x7 dosed surface, unoccupied states, at bias a) +2.0 V; b)+1.7 V; c)+1.0 V sample bias. Arrows indicate the chlorine chemisorption site. Chlorines are bright in (a) and (b) and grey in (c). A unit cell is

outlined in (c) with the open circles indicating center adatoms and red indicating the faulted side of the unit cell.

In Figure (5-4 c) it can be seen that there is no bright feature (brighter than adatoms) at +1.0 V and the bright features imaged at > +1.4 V appeared slightly lower than unreacted adatoms, i.e. as grey. In Figure (5-4 b) a single chlorine is indicated. In this image one can see clearly that the chlorine atom binds right on top of a silicon adatom.

Figure (5-5) shows a tip-induced diffusion experiment on the TCE dissociation products. The procedure is very simple: (i) Take a "before" scan under conditions that are known to almost never lead to any tip-induced alterations of the surface. (ii) Then conduct the tip-induced alteration experiment *on the same area*; in this case a test of tip-induced diffusion of chlorine species. iii) Take an "after" image under benign conditions, again over the same area. It should be noted that these STM scans typically take about 15 minutes each. During this time some lateral drift in the relative tip to sample position is inevitable. With a well-designed instrument, specifically designed to limit thermal gradients and expansions, taking subsequent images over essentially the same area is possible.

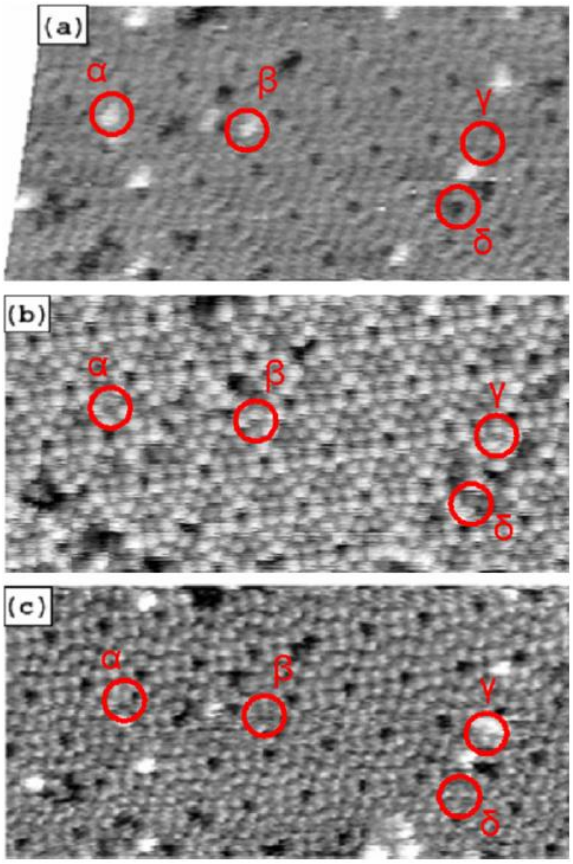

Figure 5-5 Successive STM topographic images of the same area at bias a) +1.5 V; b) -2.0 V; c) +1.5 V sample bias. Rings have been labeled to indicate the same adatom in the images.

Figures (5-5 a) and Figure (5-5 c) are topography images taken at +1.5 V sample bias at which scanning the surface does not cause any diffusion of adsorbates. Scanning the surface with bias -2.0 V causes the bright species (chlorines) to diffuse to either nearby adatoms or to desorb from the surface. The rings labeled α show the same adatom. It can be seen that a chlorine is initially bond on this adatom and after the -2.0 V scan the

adatom is unreacted again (free of chlorine). The same process happens for the ring labeled β. However, in the case of the rings labeled γ, initially the adatom is unreacted and after the -2.0 V scan it has a chlorine bonded to the adatom. It is noted that -2.0 V sample bias coincides with the peak rate of tip-induced diffusion of chlorine as shown in Figure 3.9 [51].

During the scans at -2.0 V the telltale sign of extremely localized tip-induced desorption/diffusion was rarely seen, i.e., truncation of the diffusing feature during the topography scan [56]. This observation is consistent with the rare form of diffusion explained in section (3.2).

At positive bias diffusion of chlorine atoms was also observed. Very active tip-induced diffusion at +2.4 V and +2.7 V was observed. This is consistent with the report on diffusion of chlorine by electron injection from the tip (explained in section (3.2)), with the bias threshold of diffusion ~+2.0 V [50, 52].

The bright features in Figure (5-4 a and b) look like chlorine atoms and move like chlorine atoms (as explained in section (3.2)). With these pieces of evidence we are confident that these bright features have been properly identified as chlorine atoms bonded on adatoms. This confirms the previous reports [82, 83] that the TCE molecule dissociates by losing a chlorine. The rest of the molecule, a dichlorovinyl radical, stays intact and binds to another binding site. It is believed that the dark features in Figures (5-4 a and b) are caused by the chlorovinyl group, bonded to the adatoms. This is supported

by the observation of approximately the same number of bright features as dark features at biases > +1.4 V.

5.3.2 Site Selectivity of Chlorine

As explained earlier, the charge density on corner and center adatoms differs because of the charge transfer to restatoms. There is also charge transfer from the unfaulted to the faulted half of the unit cell as well. In particular restatom dangling bonds contain approximately 1.5-2.0 electrons, while corner adatom dangling bonds contain approximately 0.75 electrons and center adatoms contain approximately 0.5 electrons [90]. Due to the high electronegativity of halogens, a reasonable hypothesis is that there would be a preference for the binding of these atoms to adatoms with a local charge value near 1.0 electrons so the chlorine atoms would prefer corner adatom more frequently than center adatoms. This hypothesis is supported by a firm theoretical foundation established through the density functional based considerations of the Joanopoulos group [39].

For finding the site preference of the dissociated chlorines the surface was scanned at sample bias values in the range of +1.7 to +2.0 V. This bias range is below the threshold for diffusion of chlorines so the diffusion of chlorine will not disturb the statistics. Chlorines bonded to center or corner adatoms as well as bonded on faulted or unfaulted halves of the unit cell were clearly distinguished in STM images. The results are displayed in Table (5-1):

Table 5-1 Binding preference for chlorine atoms after dissociation from TCE molecule.

Adatom binding site	Chemisorbed chlorine atom fraction (%):	Counts:
Faulted corner	42±3	119
Unfaulted corner	32±2	92
Faulted center	15±2	41
Unfaulted center	10±1	29

These results are from counting three hundred chlorines. It can be clearly seen that the preference is with corner adatoms. The error in Table (5-1), in the case of chlorines bonded on Faulted corner adatom for example, was calculated as follows: the ratio of the number of chlorines bonded to the faulted corner adatoms to the total number of chlorines in each image was calculated. This ratio was averaged over all the images obtained (exposed surfaces). The standard devotion of the mean was calculated and assigned to the error indicated in the table. It was found that overall, chlorines chemisorb on corner

adatoms 2.9±0.3 times more frequently than on center adatoms. Comparing the preference for the two halves of the unit cell, the chlorines bind to the faulted half 1.35±0.10 times more than unfaulted half of the unit cell. These statistics were obtained by using the number of counts on different images. The error was calculated by calculating the standard deviation of the mean value of all the images that where analyzed. These results confirm our hypothesis that the chlorines prefer binding on adatoms with higher charge density.

5.3.3 Discussion

This site selectivity of chlorines is at odds with the results reported for atomic chlorine and molecular chlorine. For atomic chlorine there is no site selectivity [48]. The reason is because the chlorine atoms are very reactive and symmetric. For this reason they do not have the opportunity to migrate laterally, so as soon as they reach the surface they most likely bind to the first available binding site. The same scenario holds for atomic hydrogen [91, 92]. The high reactive property of atomic chlorine was reported to control the binding configuration for molecular chlorine [90]. The Cl_2 molecule dissociates as it reaches the Si(111)-7x7 surface and the dissociated atomic chlorines do not migrate more than ~7Å until they bind on an adatom. In their studies Kummel's group reported that the chlorine molecule dissociates more frequently above center adatoms. This is because of the relatively empty dangling bond of the center adatom interacting strongly with a filled pair of doubly-degenerate molecular π^* states (lone pair). Furthermore they observed that the dissociated chlorine atoms most frequently chemisorb with neighboring

adatoms, which are the two adjacent center adatoms in the middle of the unit cell. In the dissociated chlorine from the TCE molecule it appears that the chlorine atoms have more opportunity to be site selective and bind to adatoms with higher electron charge.

Thinking that the chlorine atoms dissociated from the TCE would migrate on the surface approximately 30Å (the separation between the vinyl group and the chlorine) is not reasonable considering the reactive property of chlorine atoms. A reasonable explanation can be obtained by considering a mobile precursor state [93]. After reaching the surface the TCE molecule will bond to the surface with a relatively weak physical bond (physisorption). In this physisorbed state the molecule can readily diffuse across the surface sampling various possibilities for making a transition to either a lower energy chemisorbed state or to dissociation (and the products could then chemisorb to the surface). While in the mobile precursor state a TCE molecule would find an increased likelihood of dissociation above a corner adatom (and more probably when the TCE molecule is on the faulted half of the unit cell). Note that this scenario implies that the dichlorovinyl radical would travel ~30Å after the spontaneous dissociation.

This site selectivity of chlorine atoms can be explained by any combination of the following two scenarios: the first scenario is that, while in the precursor state, the probability of dissociation of the TCE molecule is higher above the corner adatom as compared to the center adatom. The relatively high electron charge of a faulted corner adatom, for example, could lower the activation barrier for dissociative adsorption [94]. The second scenario is that while the TCE diffuses on the surface in a mobile precursor

state it spends more time over corner adatoms as compared to center adatoms. This second scenario could be justified by using low-temperature STM. For example, a low-temperature STM study on benzene [95] showed that the benzene molecule spends more time above center adatoms, diffusing in a honeycomb-shaped region, than above corner adatoms. The benzene molecule, when chemisorbing, binds on center adatoms three times more frequently than on corner adatoms, i.e. it prefers the binding site with lower electron charge (opposite to chlorines from TCE). As Wolkow's group pointed out, there is a considerable corrugation in the van der Waals interaction potential for a semiconductor surface such as Si(111)7x7 with the benzene molecule, as this interaction would be affected strongly by the local charge density. In the case of a TCE molecule, this van der Waals interaction may be stronger on top of the corner adatom than elsewhere.

5.3.4 Dichlorovinyl Group on Si(111)-7x7

As the EELS studies show, chlorine dissociates upon reaction of TCE on the Si(111)-7x7 surface. Since the C=C double bond stays intact, the species on the surface will be 1,2 dichlorovinyl and 2,2 dichlorovinyl. In our STM experiment the chlorines were identified with a high level of confidence, and the dark features are assigned to the rest of the molecule, a dichlorovinyl. This conclusion is supported by the observation of approximately the same number of bright features as dark features at biases > +1.4 V.

After counting 350 dark features among many STM images there was no site preference observed on the corner or center adatoms nor on the faulted or unfaulted half

of the unit cell. The ratio of the vinyl group binding of corner adatoms to center adatoms was 0.9±0.2 and the ratio of the vinyl group binding on faulted half to unfaulted half of the unit cell was 1.1±0.1.

The dark features were inspected at a sample bias of ~+1.7 V in high quality images for low dose (0.073L) for their apparent height relative to corner adatoms. As shown in Figure (5-6), T1 and T2 indicate two types of dark features. T1 is the type in which the adatom is dimmer than an unreacted adatom but not as dark as T2 type. T2 type are features as dark as corner holes. The average depth for the T1 type is ~0.6 Å and for type T2 is ~1.0 Å, both compared to corner adatoms.

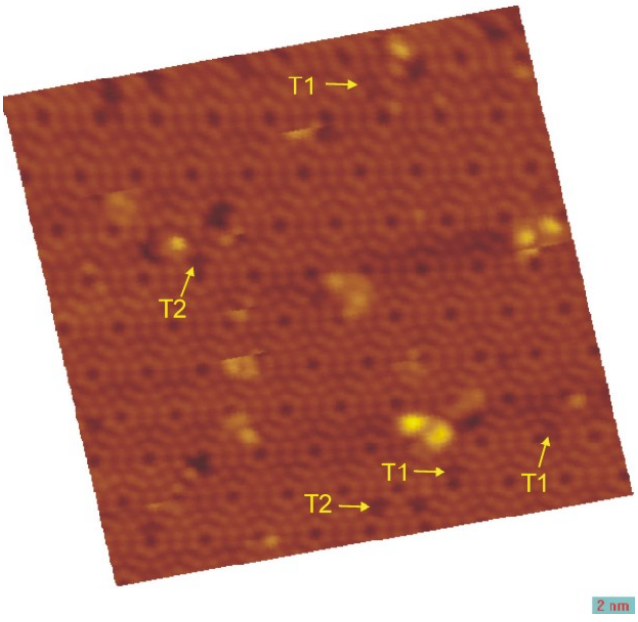

Figure 5-6 STM topographic image of Si(111)-7x7 after 0.073L TCE exposure. T1 and T2 are the two types of dark features that are observed. The bias was +1.7 V and the tunnel current was 0.1 nA.

The apparent depth of these sites relative to corner adatoms was measured from cross-sections of the STM images. These statistics are histogrammed in the Figure (5-7).

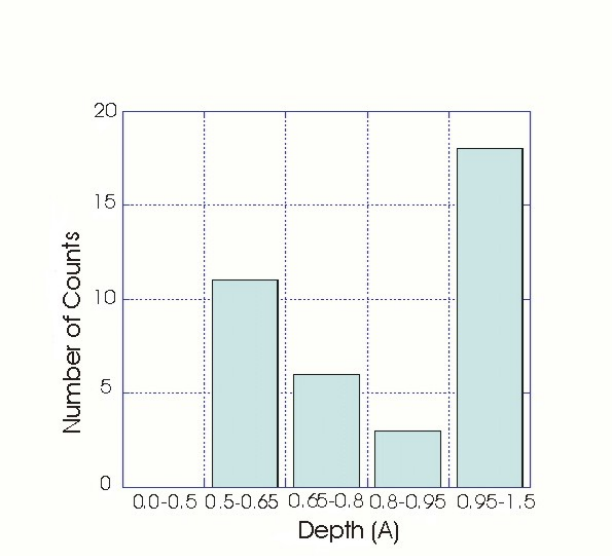

Figure 5-7 Graph of depth distribution of dark features at +1.7 V bias. A total of 39 features were counted over several STM images.

Of course, some of these dark features are defects present on the surface before the TCE dose. From the measured density of defects on the clean surface one can estimate that 11 defects were included in the histogram. Clearly the total number of 39 dark features cannot all be defects. It should be mentioned that usually defects observed on the Si(111)-7x7 surface are of the dark, deep defects at +1.7 V bias. It can be concluded that the defects fall in the 0.95-1.5 Å category mostly. This would leave 7 counts in the

0.95-1.5 Å bin that would be considered as not being defects. Given the small number of counts in this study one is left with two conclusions: 1) the number of vinyl group features of depth greater than 0.8 Å is not statistically significant, implying that there is only one type of feature i.e. the grey T1 feature, and 2) there are two main types of dark features: one with depth of 0.5-0.65 Å and the other with depth of 0.95-1.5 Å. In either case the T1 feature is the most common and should correspond to the situation where the 1,2 dichlorovinyl or 2,2 dichlorovinyl binds to an adatom (Figure (4-7 I or II)) i.e. Leung's major pathway configuration. This configuration seems to be the lowest energy one available at room temperature. Double dechlorination is possible but only above 450 K.

Schematics for this major pathway are shown in Figure (5-8). It is noted that one would not expect STM to be capable of distinguishing the two cases (I) and (II) displayed in Figure (5-8).

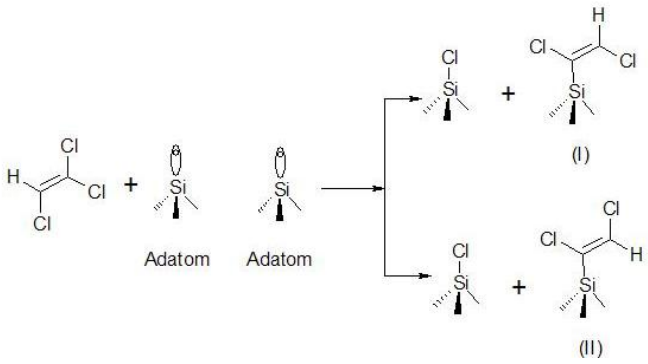

Figure 5-8 Schematic diagram of the major path way for interaction of TCE on Si(111)-7x7 at room temperature

That an adsorbed species containing a C=C double bond would be imaged as a grey feature and not a very dark feature makes good sense. The double bond on this product should contribute more tunnel current than a single bond. It is well known that after benzene reacts with Si(100)-2x1 it forms a cyclohexadiene-like structure with two C=C double bonds that make the adsorbate very bright at -2.0 V bias [96-98]. The extreme brightness of this structure is attributed to the strain likely to be present in these C=C bonds. Of course the case of the chlorovinyl group on Si(111)-7x7 is quite different. Nevertheless, as shown in Figure (5-9 B), the T1s are indeed imaged as bright features at -2.0 V. Figures (5-9A) and (5-6) are from the same area of the surface. The yellow rings in the Figure (5-9 A and B) indicate T1 type and blue squares indicate T2 type. The ring labeled α in Figure (5-9 A and B) indicates the same adatom. This adatom is of type T1 as shown before (Figure 5-6). It can be seen that this adatom turns bright when we scan the surface at -2.0V (Ring α in Figure (5-9 B)). The same change in brightness occurs for β and γ rings. It can be seen that for the δ and ε squares of type T2 the reacted adatom remains dark at -2.0V.

The simplest scenario then is that the T1 features represent the only significant type of vinyl group bonding i.e. the major pathway configuration. This implies that the T2 features are defects that were present before dosing.

If on the other hand one considers the possibility there is another bonding configuration i.e. T2 is actually a configuration of a vinyl group then it is not clear how to

model this state. One might think that the T2 corresponds to the minor pathway configuration i.e. to the case where the TCE adsorbs molecularly on the surface. This bonding configuration is caused by the dative covalent bonding between Cl and the substrate Si adatom and restatom. The biggest difficulty with assigning the T2 feature to this pathway is that the configuration disappears at 340 K in the TDS experiments. That this temperature is only slightly higher than room temperature indicates a short residence time on the surface at room temperature before desorbing. It seems very unlikely that this species would stay on the surface long enough to be imaged by STM. One is left with only speculation. The T2 state may be a chlorine atom bound to an adatom with the chlorovinyl group bound to an adjacent rest atom. The charge transfer may be complex and result in the dark feature even at -2.0 V bias. This hypothesis could in principle be tested by using STS at -0.8 V where restatoms are prominent. Or perhaps the TCE does not dissociate but rather binds to an adatom and an adjacent rest atom. This type of Diels-Alder reaction is believed to occur for ethylene and involves the loss of the C=C double bond. The loss of the double bond may explain the apparent depth of the T2 feature in STM.

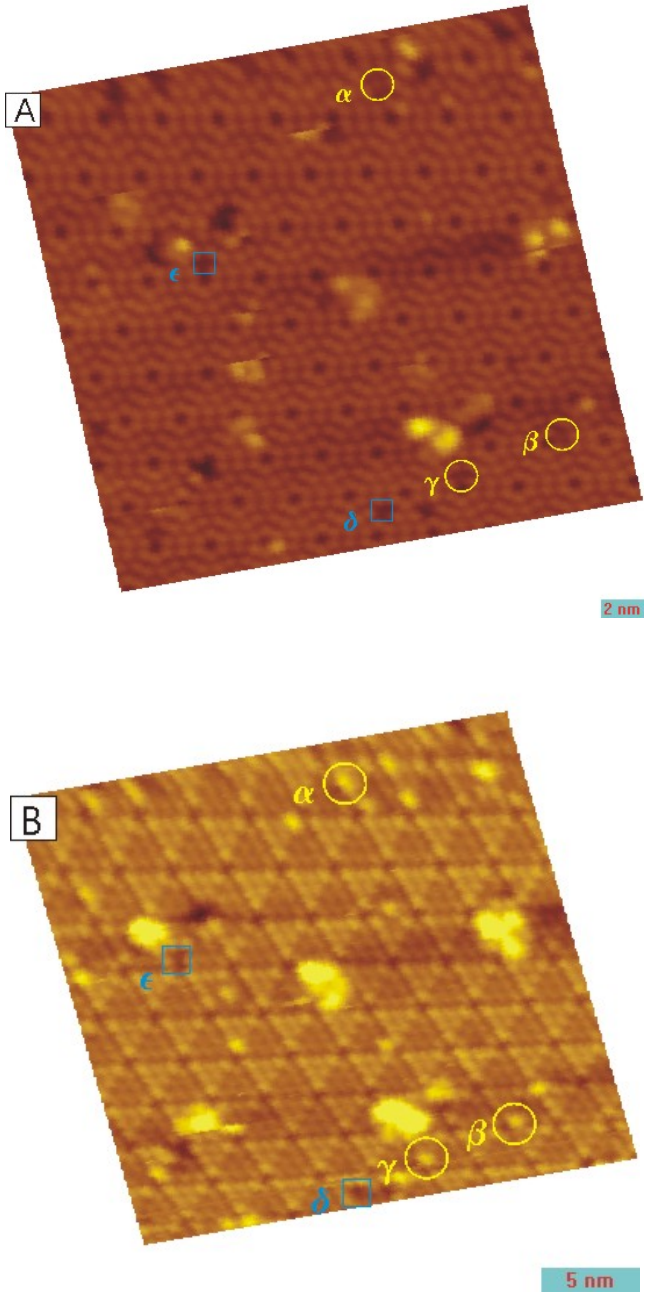

Figure 5-9 STM topographic images of the same area on the Si(111)-7x7 surface with 0.073L TCE dosed. At bias (A)+1.7 V; (B)-2.0 V. The yellow rings indicate T1 type features and blue squares indicate T2 type.

5.3.5 Summary

The procedure for cleaning Si(111)-7x7 surface was explained. The atomic resolution advantage of STM was used to identify the products of dissociation of TCE on the surface. The dissociation of chlorine was confirmed and a site preference at corner adatoms and on the faulted half of the unit cell was observed. Different types of binding configurations for the vinyl group and molecular adsorption were suggested as a result of the observations done on the surface at the atomic level. No specific binding preference was observed for the grey/dark features.

One may now ask the question: How much generality is there in these TCE results? In particular how would the interaction of TCE with silicon change if allowed to interact with another surface of crystalline silicon? These questions will be addressed in the following two chapters.

Chapter 6

Review of Dissociation of Molecules on the Si(100)-2x1 Surface

In comparison with the Si(111)-7x7 surface, the Si(100)-2x1 surface undergoes a simpler reconstruction. The 2x1 surface is one of the most important surfaces in the microelectronic technology. This surface currently provides one of the most important platforms in the development of molecular electronics and nano-scale devices. Good candidates for molecular electronics are organic molecules. This is because their tunable properties such as size, shape, flexibility and conductance can be used to make them functional for molecular devices. For this we need to have a microscopic picture of structures and bindings of organic molecules on silicon surfaces. Furthermore, the property of these molecules in their migration, affects their binding to surfaces.

For studying the binding of organic molecules on surfaces, one important category is to study the types of molecules that dissociate while binding. For this to happen the atomic-scale probing property of STM can be used to identify the interaction of these types of molecules and to identify the products of dissociation.

In this chapter the atomic and electronic structure of the Si(100)-2x1 surface is explained. Studies of the interaction of ammonia, methyl chloride and perchloroethylene on this surface using different surface analysis instruments are reviewed.

6.1 Atomic and Electronic Structure

The chemistry of the Si(100)-2x1 surface is related to the geometry and electronic structure of the surface atoms [42]. The chemistry of the surface is driven by the fact that the surface silicon atoms have a tendency to reach a coordination number of 4. To better understand the chemistry of the surface it is necessary to understand the reconstruction of the Si(100)-2x1 surface.

By cleaving bulk silicon in the (100) direction the bulk terminated surface will be a (1x1) structure as shown in Figure (6-1) [42]. It can be seen that the atoms on the surface are connected to the bulk by two bonds. In addition they have two bonds unoccupied (dangling bonds). By lateral translation of the surface atoms, one of the dangling bonds on each silicon atom forms a σ bond and the remaining bond on each atom form a weak π bond forming dimers, causing a (2x1) structure as shown in Figure (6-1). The reconstruction of the surface by lateral translation of the surface atoms was proposed first by Schlier and Farnsworth in 1959 [99]. Alternative structures have been proposed for the reconstruction of Si(100) [100, 101] but the electronic structure calculations have shown that the lowest energy is achieved by the dimer structure [102-104] (as shown in Figure (6-1)).

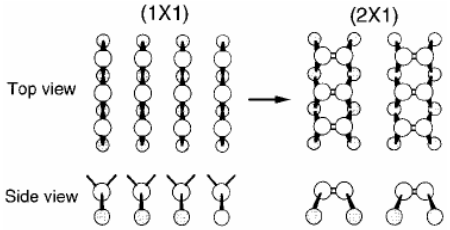

Figure 6-1 Structure of unreconstructed (1x1) and reconstructed (2x1) Si(100) surface top and side view (Figure taken from Ref. [42])

The surface electronic energy states of the Si(100)-2x1 are the π, π*, σ and σ* states and these states are indicated in Figure (6-2).

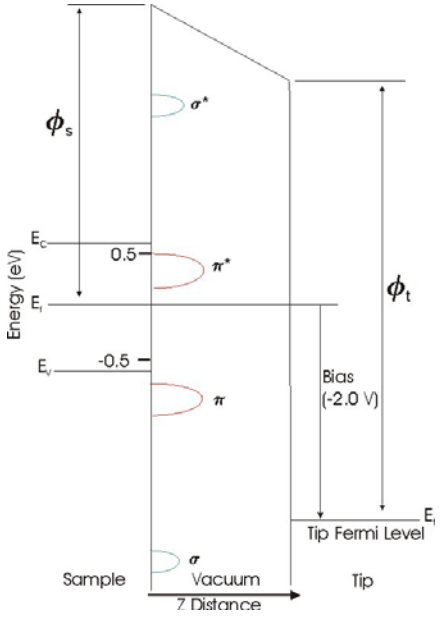

Figure 6-2 One dimensional energy level diagram of the Si(100)-2x1 surface at -2.0 V sample bias. In this diagram, φ_t and φ_s are work functions for the tungsten tip and silicon surface respectively. The z axis is perpendicular to the sample surface. Surface states π,

π*, σ and σ* are located at -0.7, 0.35, -2.0 and 2.0 eV relative to the Fermi level. The data for this diagram is from Refs. [14, 94, 105, 106]

As discussed in Chapter 1, the tunneling current, for example under occupied states conditions, is provided by the electrons in the occupied state bands from the Fermi level to the bias level that tunnel through vacuum. When scanning the surface at -2.0 V sample bias, the π state electrons are being probed. In Figure (6-3) an occupied state image at -2.0 V bias is shown.

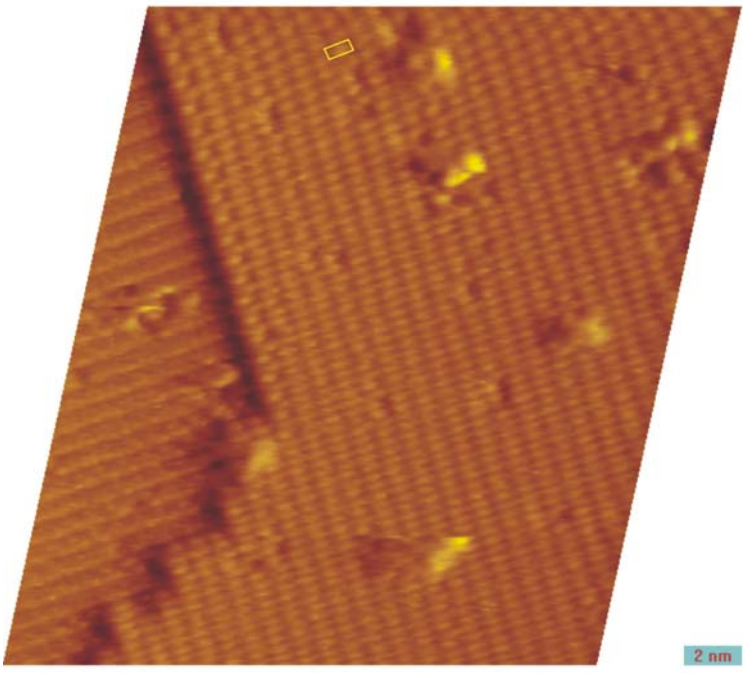

Figure 6-3 STM image of the Si(100)-2x1 surface probing occupied states. The π bond has a bean shape form as can be seen in the rectangle. This image was taken at sample bias at -2.0 V and tunneling current of 0.2 nA.

The π molecular orbital has a maximum at the center of the silicon dimer [107], giving it a bean shape as shown in the rectangle in Figure (6-3). By looking at the Figure (6-3) it can be seen that the dimers are located such that they form dimer rows. In addition the steps on the Si(100)-2x1 surface are such that for a single atomic step the dimers on a terrace are perpendicular to the dimers on the other terrace.

At positive sample bias the unoccupied states are probed. The π* provides most of the tunneling electrons as it is nearer to the Fermi level in energy. This can be seen in Figure (6-2) as the π* surface state energy lies near the Fermi level. In Figure (6-4) the STM image at bias +2.0 V is shown.

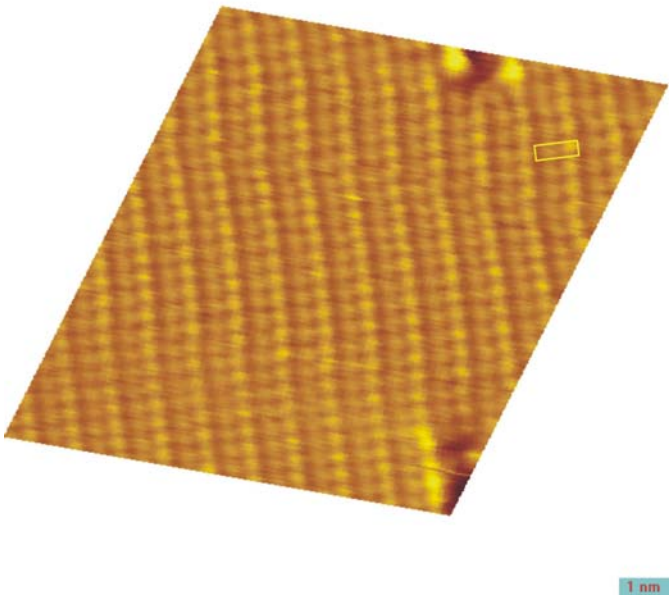

Figure 6-4 STM image of the Si(100)-2x1 surface probing unoccupied states. The π* state has a node in the middle of it as can be seen in the rectangle. Sample bias +2.0 V and tunneling current of 0.5 nA

The π* antibond has a minimum (node) at the center of the dimer [107] as shown in the rectangle in Figure (6-4). It was found that the dimers on the Si(100)-2x1 surface are not symmetric as can be seen in Figure (6-4). That is one side of the dimer is higher than the other side. To the best of our knowledge there has been no report of the asymmetry of Si(100)-2x1 dimers at positive sample bias. It should be mentioned that this asymmetry was observed by several different tips which may indicate that this is not a tip effect.

Formally the dimers have both a σ bond and a π bond. The π overlap is poor in the silicon dimer which is caused by the strained geometry at the surface preventing the spatial overlap of the orbitals needed for a strong π bond. The pairing energy for the dimer π bond for Si(100) surface is ~5 kcal/mol which is much weaker than the silicon σ bond of 78 kcal/mol in the silicon dimer [108, 109]. Comparing Si dimer π bond to the C=C π bond in ethylene which is 65 kcal/mol [110], the weakness of this bond becomes more obvious. The weakness of this π bond in the silicon dimer controls the interaction of the Si(100)-2x1 surface with other molecules. This is because the π bond easily breaks when a molecule interacts with this surface and by the π bond having been broken between the two atoms, two dangling bonds become available on the dimer.

There are still some facts about the Si(100)-2x1 surface left unknown. Early theoretical studies suggested that in order to lower the energy, the axis of the dimers should not be parallel to the surface; therefore, the dimers should be tilted [104, 111]. STM images at room temperature show mostly symmetric dimers, and tilted dimers are

only present near step edges and defects. These observed tilted dimers alternate from dimer to dimer along a row, making a zigzag structure which is called “buckled dimers”. The c(4x2) and p(2x2) symmetry is formed if the dimers on the two neighboring rows buckle in the opposite direction and same direction respectively [40, 112, 113]. In order for the theory and experiments to be consistent, Hamers proposed that the appearance of symmetric dimers in STM occurs, because the tilted dimers flip back and forth due to thermal excitation [112]. At room temperature the time-averaged (compared to the STM measurement time) configuration for the dimers is symmetric although they are buckling about this equilibrium configuration. Low temperature studies on the Si(100) surface showed that the surface mainly consisted of buckled dimers (alternating from dimer to dimer) producing c(4x2) symmetry [114]. This shows that at low temperature, the flipping action of dimers freezes, causing asymmetric dimers.

The buckling of the dimers causes charge transfer from the low atom to the top atom (from one side of the dimer to the other). This process makes the tilted dimer (asymmetric) richer in electron charge compared to a non-tilted dimer (symmetric). It has been reported that adsorption of strongly electronegative and/or electropositive adsorbates on Si(100) causes more buckling than for more neutral adsorbates [115].

6.2 Dissociation of Molecules

The Si(100)-2x1 surface is a simpler surface as compared to the Si(111)-7x7 surface. As discussed previously STM makes the atomic scale observation of the interaction of molecules on the surfaces possible. One can observe how individual molecules bind to

the surface at the atomic level. It should be mentioned that the limitation in imaging of the silicon surface is limited to ~ $E_f \pm 4$ eV as higher biases tend to result in uncontrolled damage to the sample and tip. This makes the identification of adsorbates on the surface difficult since the binding energy states of adsorbates are usually far away from the STM tunneling range [58]. The solution as shown in the case of Si(111)-7x7 is to use other surface analysis methods, such as photoemission spectroscopy and ion scattering, when analyzing the STM images.

Compared to the Si(111)-7x7 surface, binding sites on the Si(100)-2x1 surface do not have the same variety of electron charge (caused by charge transfer). As mentioned before the chemistry of the interaction of molecules on this surface is controlled by the weak π bond present in the dimer. The dissociation of ammonia, methyl chloride, perchloroethylene and trichloroethylene is discussed in the following sections.

6.2.1 Dissociation of Ammonia

Hamers et al used STM to probe the interaction of molecules on surfaces for the first time by studying the interaction of NH_3 on the Si(100)-2x1 surface [105]. In Figure (6-5 a,b) STM topographic images of the clean Si(100) surfaces are shown at -2.0 V and +1.2 V respectively. The Si(100) surface after dosing the surface with ammonia is shown in Figure (6-5 c,d) at -2.0 V sample bias.

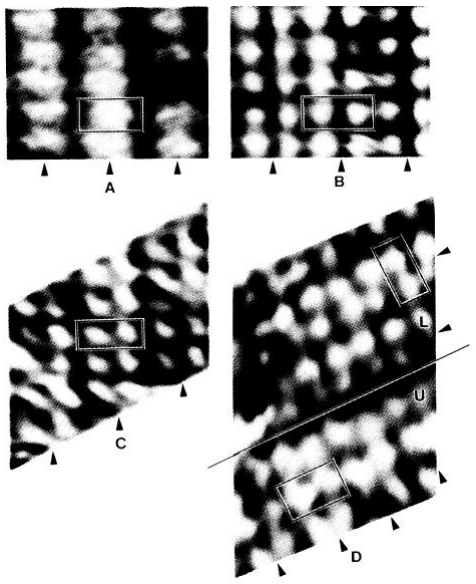

Figure 6-5 STM topographic images of Si(100)-2x1 surface. Each rectangle shows the 2x1 unit cell. A) clean surface at -2.0 V; B) clean surface at +1.2 V; C) dosed with NH_3 at -2.0 V; D) dosed NH_3 at -2.0V. Each arrow points in the <011>direction and directly at the center of a dimer row. (Figures taken from Ref. [105])

Just by analyzing the STM topography alone, the adsorbates on the surface can not be properly identified. Comparing Figure (6-5 a) to Figure (6-5 c,d) it can be seen that the bean-shaped dimers have changed into two individual protrusions in each dimer after dosing the surface. Earlier x-ray photoemission (XPS) and ion-scattering spectroscopy (ISS) reported that NH_3 dissociates on the Si(100)-2x1 surface even at low temperatures (~90K). Later HREELS [116] and XPS [117] studies also reported that the dissociation

products are NH_2 and H. It was reported that the N atoms (of the NH_2 products) occupy the subsurface sites while H atoms occupy the surface sites [118, 119].

Using these pieces of information from the XPS and ISS it can be understood that the adsorbates on the surface of Si(100)-2x1 as observed by STM, (Figure (6-6 c,d)), must be hydrogen atoms. Figure (6-6), spectrum A, shows the tunneling spectra ($(V/I)\,dI/dV$) on the clean Si(100) surface. The peaks at 0.8 eV below and 0.35 eV above the Fermi level are assigned to π_b bonding level and π_a antibonding respectively.

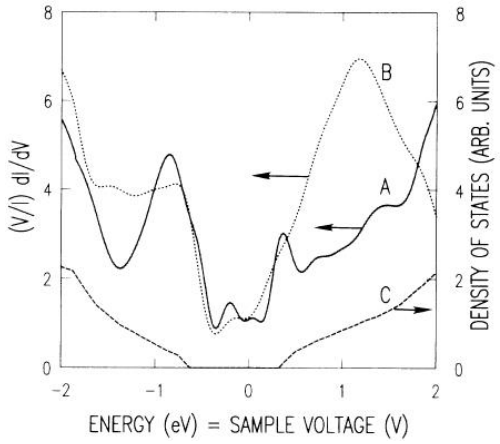

Figure 6-6 Tunneling spectroscopy measurements on the Si(100)-2x1 surface on A) clean surface B) dosed surface C) calculated silicon bulk density of states (Data taken from Ref. [105])

It is seen that the π bonding and π* antibonding present on the clean Si(100)-2x1 surface vanishes after the NH_3 exposure (Figure 5-7 spectra B). A new peak appears in the dosed surface spectra at ~ 1.0 eV above the Fermi level. This peak is attributed to a

Si-H antibonding state, from the calculations by Ciraci et al [120] , and the EELS data by Maruno et al [121]. The two protrusions on each dimer in the STM images of Figure (6-7 c,d) can be assigned to hydrogen atoms bonding to silicon dangling bonds (Si-H antibonding) [105].

It can be concluded that the interaction of NH_3 on the Si(100)-2x1 surface is of a dissociative form. The hydrogen atoms dissociate from the ammonia molecule and bond to the dangling bonds present on the dimers after the weak π bond is broken. In STM images no feature was seen to be attributed to the subsurface nitrogen, nor NH_x fragments as the product of dissociation.

6.2.2 Dissociation of Methylchloride

Bronikowski et al [122] studied the interaction of methyl chloride (CH_3Cl) with Si(100). The methylchloride molecule is shown in Figure (6-7).

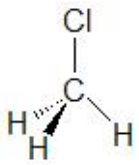

Figure 6-7 Methyl chloride molecule

Using STM they tried to identify the dissociated products on the surface. The EELS and Auger Electron Spectroscopy (AES) results by Brown et al [123] reported that methyl chloride dissociated upon interaction on the Si(100)-2x1 surface at room temperature.

The products of dissociation are chlorine and CH_3 species on the surface. Chlorine starts to etch the silicon surface around 823K (550ºC) [124, 125]. The studies on chemistry of methyl groups using High Resolution Electron Energy Loss Spectroscopy (HREELS) and TDS showed that CH_3 groups are stable up to 600K [126, 127].

By heating the dosed surface to 420K for 2 minutes, Bronikowski et al [122] reported that the chlorine atoms would form the "monochloride" structure reported by Boland [45]. This was confirmed by comparing the shape that monochloride has at negative sample bias, as was observed by Boland [45] (a minimum is present at the middle of the dimer, similar to the node seen on dimer at positive bias). The "monochloride" structure is formed when two chlorine atoms bond to a silicon dimer by breaking the weak π bond on the dimer. It was reported that at 420 K the chlorine atoms can migrate to their most stable binding site, which is to form monochloride structure.

The STM topographic image at -2.2 V sample bias is shown in Figure (6-8). In Figure (6-8) the monochloride structure is labeled "Cl_2". "I" is labeled when several of these structures form an island.

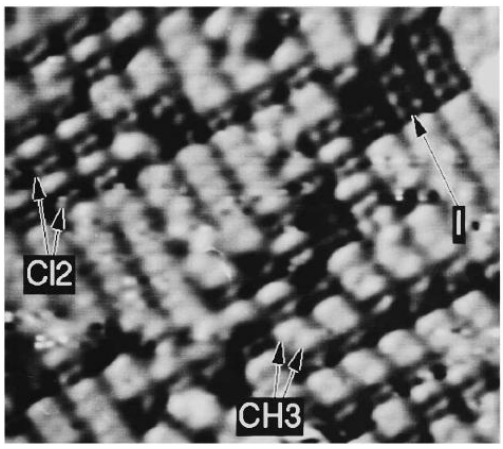

Figure 6-8 STM topographic image of Si(100)-2x1 surface after 0.3L methyl chloride dosed after heating to 420 K for 2 minutes, sample bias -2.2 V and 0.3 nA current (Figure taken from Ref. [122]).

Another feature that is observed on the surface after dosing is labeled by "CH_3". The CH_3 is identified based on their binding symmetry. This feature consists of a low protrusion sitting atop a Si dimer, displaced to one side of the dimer. The carbon in the CH_3 dissociated from the methyl chloride group needs one bond to achieve its four-fold coordination. This bond becomes available when the weak π bond on the Si-Si dimer is broken. The CH_3 group thus bonds to one of the atoms in the dimer. Figure(6-9) shows the binding configuration for the CH_3 group on a dimer [122].

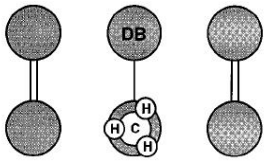

Figure 6-9 Binding configuration for the CH_3 group on the Si(100)-2x1 surface (Figure taken from Ref. [122])

The counting statistics of CH_3 and Cl_2 on the dosed surface (0.3L) that was heated briefly to 420K showed that the ratio of chlorine atoms to methyl groups was 2.0±0.2. This result shows that the adsorption of methyl chloride can occur in two pathways: one is Cl and CH_3 bound to the surface after dissociation. The other pathway is from Cl that dissociates from the methyl chloride and bonds to the surface while the methyl group is ejected (leaves) from the surface.

A recent study by Woelke et al [128] on the interaction of methyl chlorine with Si(100)-2x1 confirmed Bronikowski et al's [122] results. Their experiment was performed without heating the sample to 420K. They calculated the ratio of Cl to CH_3 species for a bigger range of exposures from about 0.0L to 2.0L. At all exposures the ratio was ~2.0. They described the dissociative adsorption of methyl chloride, via a precursor state:

$$CH_3Cl_{(precursor)} \rightarrow CH_{3\,(adsorbate)} + Cl_{(adsorbate)}$$

and

$$CH_3Cl_{(precursor)} \rightarrow CH_{3\,(gas)} + Cl_{(adsorbate)}$$

Woelke et al's [128] explanation and results agreed with the first principle calculations done for methyl chloride on Si(100)-2x1 [129].

6.2.3 Dissociation of Perchloroethylene

Zhou et al [81] studied the interaction of perchloroethylene (CCl_4) with the Si(100)-2x1 surface. The perchloroethylene molecule is shown in Figure (6-10).

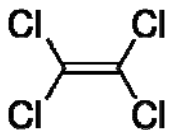

Figure 6-10 Perchloroethylene molecule

They studied this interaction by XPS, TDS and ab initio density functional calculations.

Figure (6-11) shows the XPS spectrum of the C 1s and Cl 2s regions for a 50 L exposure of perchloroethylene (PCE) on the Si(100)-2x1 surface.

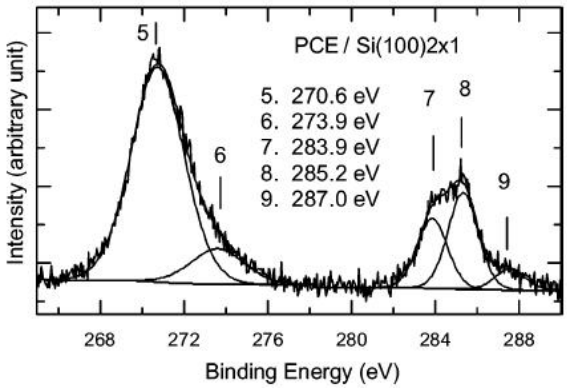

Figure 6-11 XPS spectrum of the Cl 2s and C1s region on the Si(100)-2x1 surface after 50L exposure to PCE at room temperature (Data taken from Ref. [80])

The feature for Cl 2s at 270.6 eV (feature 5) indicates that chlorines are present on the surface. In other words, chlorine atoms dissociate from the PCE molecule. The shoulder at 273.9 eV (Feature 6) is assigned to a Cl 2s shake-up (many body) process.

There exist three features for C 1s at 283.9 eV (feature 7), 285.2 eV (feature 8) and 287.0 eV (feature 9) corresponding to three different environments for carbon. To assign these features to specific environments for C, Leung's group performed hybrid density functional calculations. Possible structures for adsorption of PCE on the Si(100)-2x1 surface are shown in Figure(6-12).

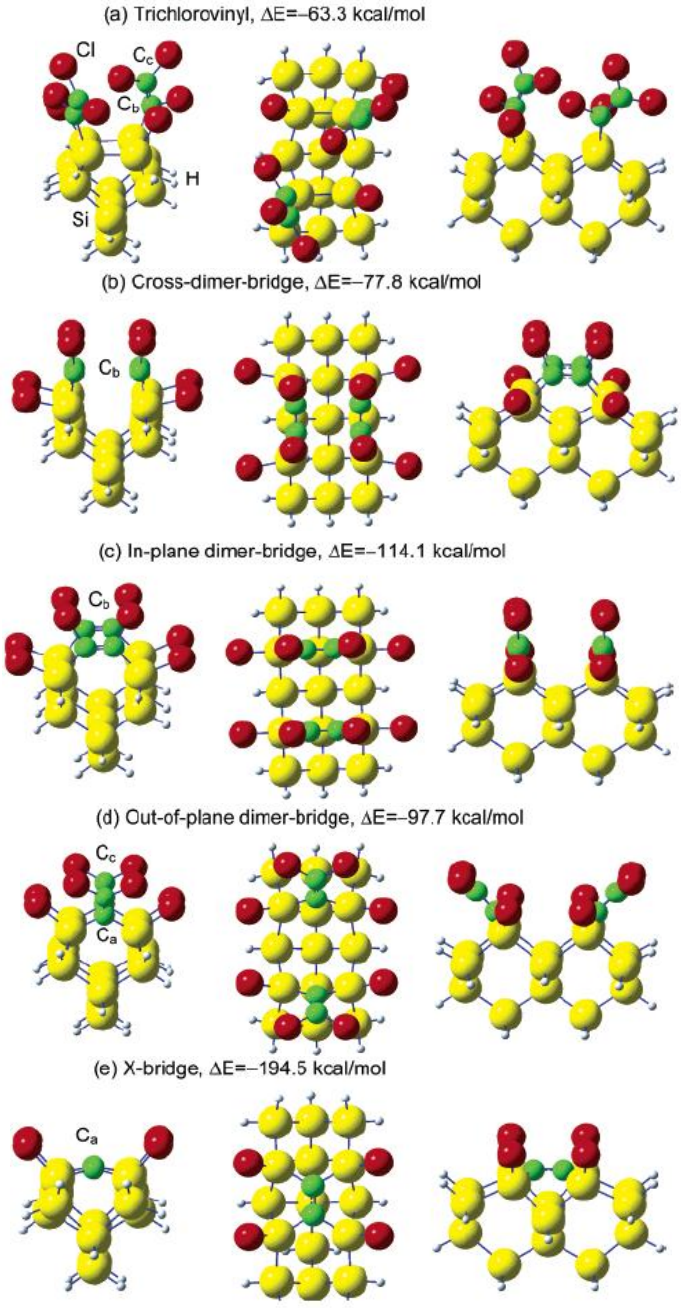

Figure 6-12 Schematic diagrams of the adsorption geometries of PCE on the Si(100)-2x1 surface. a) trichlorovinyl; b) cross-dimer-bridge; c) in-plane dimer-bridge; d) out-of-plane dimer bridge; e) X-bridge (Figure taken from Ref. [81])

Structures with mono (Figure 6-12 a), di (Figure 6-12 b,c,d) and tetra-σ (6-12 e) bondings are present on the surface. By comparing adsorption energy, the trichloroethylene (a structure with mono-σ bonded trichlorovinyl) has the least stable structure (Figure 6-12 a). From the same approach, the cross-dimer-bridge is the least stable of the three di-σ structures (Figure 6-12 b). The X-bridge structure with ΔE = 194.5 kcal/mol, has the most stable adstructure among other structures (Figure 6-12 e). This structure is achieved by full dechlorination of TCE and tetra-σ bonding of the ethenetetrayl (C_2 dimer) on the surface as shown in Figure (6-12 e).

From the possible adsorption structures of PCE on the Si(100)-2x1 surface, C_a, C_b and C_c were introduced. Considering the electronegativities of Si, C and Cl the features at 283.9 (feature 7), 285.2 (feature 8) and 287.0 eV (feature 9) are assigned to C_a 1s, C_b 1s and C_c 1s respectively. The ratio of the C_a to C_b to C_c was reported to be 4:5:1. The presence of C_c indicates structures with di-σ bond (Figure (6-12 d)) and mono-σ bond (Figure (6-12 a)). As discussed before the mono-σ structure is not a thermodynamically stable structure so the C_c feature is attributed to the di-σ bonded dichlorovinylidene adspecies. With the dichlorovinylidene being present on the surface the ratio of C_a to C_c should be 1:1. However the XPS data indicates that this ratio is 4:1. This indicates that the tetra-σ bonded ethenetetrayl (X-bridge) adspecies is present on the surface as shown in Figure (6-12 e).

The TDS profile of the parent mass for PCE did not show any features, indicating that the PCE does not desorb molecularly. No features were observed for the m/z of 47 (CCl^+), 82 (CCl_2^+), 94 ($C_2Cl_2^+$), 117 (CCl_3^+), 152 (CCl_4^+), 164 ($C_2Cl_4^+$) either.

In Figure (6-13) the XPS spectra of the Cl 2s and C 1s on the Si(100)-2x1 exposed to 50 L of PCE and annealed to different temperatures is shown.

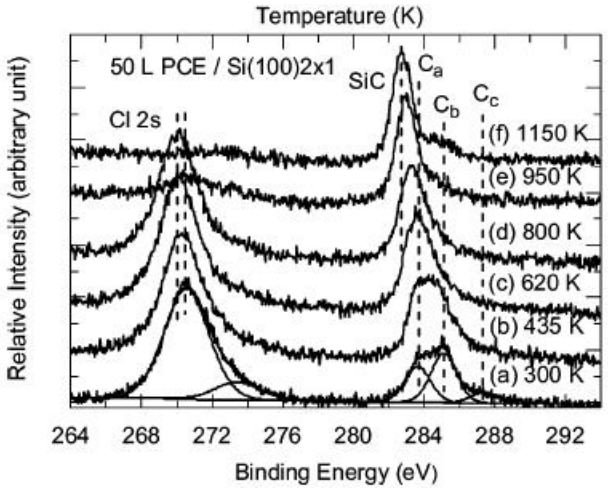

Figure 6-13 XPS spectra of a Cl 2s and C 1s on the Si(100)-2x1 surface after 50L exposure to PCE and annealing to different temperatures (Figure taken from Ref. [81])

It can be seen that the C_c feature disappears after annealing the surface to 435 K. The C_b feature diminishes after annealing to 620 K. The C_a feature reaches its maximum intensity after annealing the surface at 620 K. This information indicates dissociation of chlorine upon annealing the surface since C_b and C_c decrease. The increase for the

intensity of C_a indicates that the X-bridge structure is the favorable (more stable) structure after annealing the surface to higher temperature as well.

Comparing the interaction of ethylene with PCE on the Si(100)-2x1 surface it can be understood that the presence of chlorine changes the pathway and form of interaction. Because of the stronger bond strength of Si-Cl compared with C-Cl, as discussed in the Si(111)-7x7 surface, the interaction of PCE with this surface is of dissociative type.

6.3 Summary

In this chapter the reconstructed surface of Si(100)-2x1 was described. A review was given of various studies concerning the interaction of ammonia [119], methyl chloride [122] and perchloroethylene [81] with the Si(100)-2x1 surface. Using different surface analysis methods such as XPS, TDS, AES and STM it was found that these interactions were of a dissociative form on the Si(100)-2x1 surface.

Chapter 7

STM Studies of TCE on Si(100)-2x1

A detailed procedure for preparing a clean Si(100)-2x1 surface is described. A study of the interaction of trichloroethylene on the Si(100)-2x1 surface by STM is reported for the first time. Chlorine atoms as a product of dissociation are identified. From the observed STM images different bonding configurations for the TCE ($CHCl_3$) molecule on this surface are proposed.

7.1 Cleaning Procedure

Having a clean surface with low levels of surface contamination is a necessity for surface studies. Like the Si(111) surface, the Si(100) surface was RCA cleaned with the procedure described in section (5.2.1.1). This was done to eliminate organic contamination (especially carbon) and to form an oxide layer. The oxide layer protects the surface while mounting and transferring the sample to the UHV chamber and outgassing the sample and sample holder. As the Si(100) surface is more sensitive to maximum pressure of the chamber while annealing, the heating process was different for this surface compared to Si(111).

The Si(100)-2x1 surface has specific defects that have been studied in detail [130]. The three types of defect on this surface are called Type A, B and C defects.

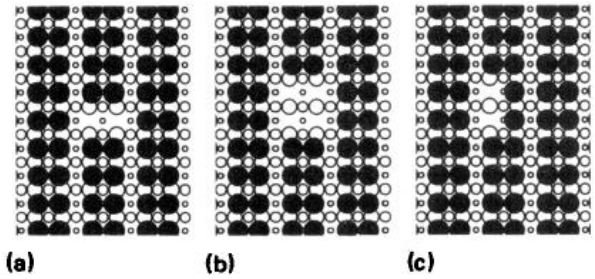

Figure 7-1 Structure of defects of Type a) A; b) B; c) C on the Si(100)-2x1 surface (from ref[130])

The Type A defect is a dimer vacancy, as shown in Figure (7-1a), in which both silicon atoms in one dimer are missing. The Type B defect is a double dimer vacancy, as shown in Figure (7-1b). These types of defects are observed as missing (dark) one dimer and two dimers respectively in the STM at occupied and unoccupied states (Figure (7-3)). Type A and B defects have mirror symmetry with respect to reflection in both <011> and $<0\bar{1}1>$ planes [130]. The Type C defect is defined as two adjacent atoms missing in the $<0\bar{1}1>$ plane. In STM it appears like two half dimers, as shown in Figure (7-2A) (and Figure (7-1C)). Type C defects are normally observed as protrusions at positive and negative sample bias. It should be noted that the Type C defect appearance in STM images is highly tip dependent, which means they are not always observed higher than unreacted dimers. Type C defects have only a <011> mirror plane symmetry. Type C defects are assigned to the interaction of water molecules with the surface. It has been shown that at low exposures of water on the Si(100)-2x1 surface, the molecular

adsorption of H_2O produces the Type C defects [131]. There is buckling observed near the C defects (in the same row), which can be explained by the lower symmetry of the C defects causing a strain effect on the surface as compared to A and B defects.

7.1.1 Annealing Process

Similar to the procedure used for Si(111), the sample was out-gassed overnight at 630°C. The high temperature annealing was used to eliminate the remaining carbon contamination on the surface. The sample was heated to 1220 °C for 5-6 sec while monitoring the pressure to ensure it does not exceed 3×10^{-10} Torr. As mentioned, the Si(100) is very sensitive to the maximum pressure of the chamber while annealing. It was found that the density of Type C defects was higher when the maximum attained pressure during the anneal process was higher. This result is consistent with those reported by Hata et al [132] and Ukraintsev et al [133]. The sample was repeatedly flashed at 1220 °C until it was observed that the maximum pressure of the chamber was not decreasing anymore. The typical maximum pressure of the chamber during flashing was 1.8×10^{-10} Torr. After cooling the stage (if the stage temperature was higher than 25 °C) and waiting for 10 minutes, the sample was flashed to 1165 °C for 10 seconds. This is done since at this low peak temperature the sample holder would not outgas much. Therefore, the maximum pressure of the chamber would be around 9×10^{-11} Torr (a lower maximum pressure results in fewer Type C defects) while still eliminating other contaminants such as oxygen, hydrogen and chlorine (other than carbon). This procedure

routinely results in clean Si(100) surfaces as confirmed by the STM images as shown in Figure (7-2 (A and B)). The defect density on this surface is 0.034, 0.011 and 0.004 (defects/nm^2) for Type C, A and B.

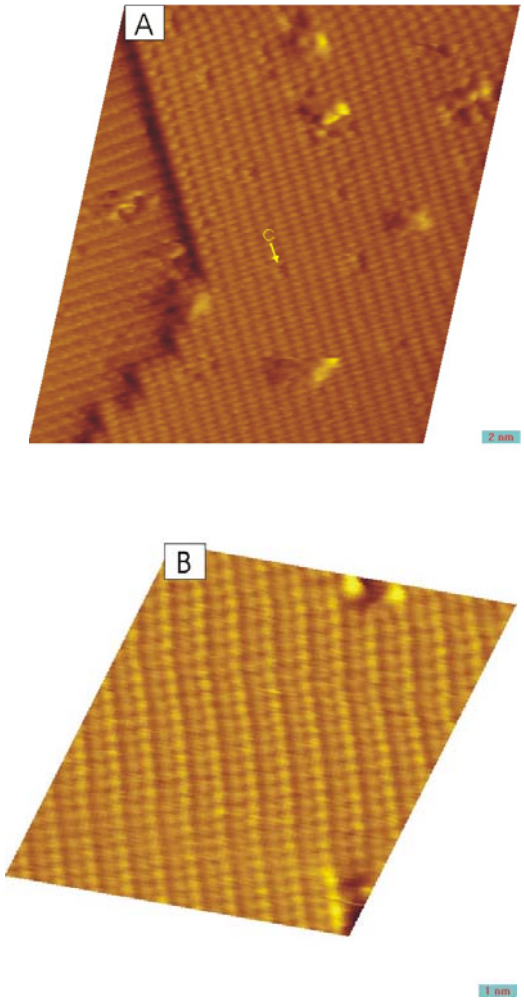

Figure 7-2 STM image of Si(100)-2x1 surface probing A) occupied states at bias -2.0 V; B) unoccupied states at bias +2.0 V of clean surfaces after the above mentioned cleaning procedure. In (A) a Type C defect is shown.

It should be mentioned than in the case where the sample was flashed to high temperatures, near 1270 °C, for 10 seconds, during which the maximum pressure of the chamber was ~1.7×10^{-10} Torr, a clean surface did not result. This is obvious by looking at Figure (7-3) which is the STM image of the Si(100)-2x1 surface prepared by the mentioned process. It can be seen that there are lots of Type A, Type B and Type C defects on the surface. With such a surface it is hard to study the surface after dosing it with molecules. This is because with such a high number of defects, distinguishing adsorbates from defects after dosing is almost impossible.

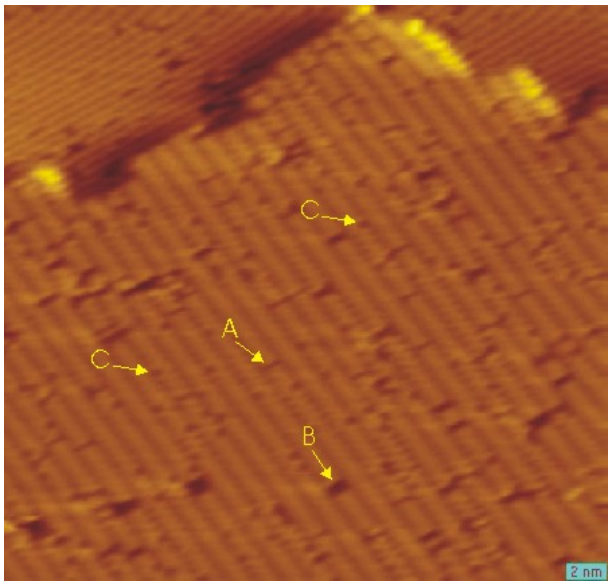

Figure 7-3 STM topography images of the Si(100)-2x1 surface at sample bias -2.0 V and set point current of 0.16 nA. A Type A (single missing dimer), Type B (two missing dimer) and Type C defects are shown. The large number of defects can be seen on the surface due to high maximum chamber pressure (1.7×10^{-10} Torr) while annealing and not being RCA cleaned.

The large number of defects, especially of Type C, shows the importance of keeping the maximum pressure of the chamber low during annealing. It should be noted that the surface shown in Figure (7-3) was not RCA cleaned.

7.2 STM Study of Trichloroethylene

The interaction of chlorinated unsaturated hydrocarbons is discussed in this section. As discussed in section 6.2.3 Leung's group performed XPS and TDS studies on these kinds of molecules on silicon surfaces [81].

The interaction of the simplest unsaturated hydrocarbon, ethylene, has been studied theoretically and experimentally by different surface analysis methods [134-137]. Ethylene bonds to the Si(100)-2x1 surface by forming a [2+2] cycloaddition structure [137-139]. The schematic of the binding configuration is shown in Figure (7-4).

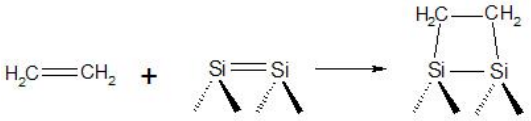

Figure 7-4 Schematic of interaction of ethylene with Si(100)-2x1

It should be noted that the interaction is not in the form of a dissociation process.

TCE is different from PCE by having one less chlorine. STM was used to observe the interaction of TCE on the Si(100)-2x1 surface at the atomic level. In the following

sections the products of dissociation are identified. The dissociated chlorine and the rest of the molecule, a dichlorovinyl, were identified by STM.

7.2.1 Chlorine on Si(100)-2x1

The interaction of chlorine on the Si(100) surface was studied with STM by Boland [45] and Lyubinetsky et al [94]. The stable bonding configuration has the chlorine atom bonded on the dimer as shown in Figure (7-5).

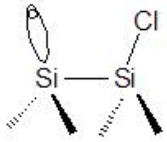

Figure 7-5 Chlorine bonded on a Si(100)-2x1 dimer

This happens when the dimer π bond is broken. This kind of dimer is observed bright at one side and dark on the other. The bright side is attributed to the unoccupied (dangling bond) bond since its energy level lies near the Fermi level [45, 94]. Figure (7-6) is a topographic STM image of the Si(100)-2x1 surface at bias -2.0 V after 0.01L of TCE exposure. After the TCE exposure the features similar to the above mentioned structure are pointed out by arrows. The arrows are pointing at the unoccupied bond on the dimer. The binding energy of Cl on the Si(100) dimer is ~5 eV which is far from the STM bias range [94]. Therefore the dark side of the dimer is attributed to the chlorine binding site.

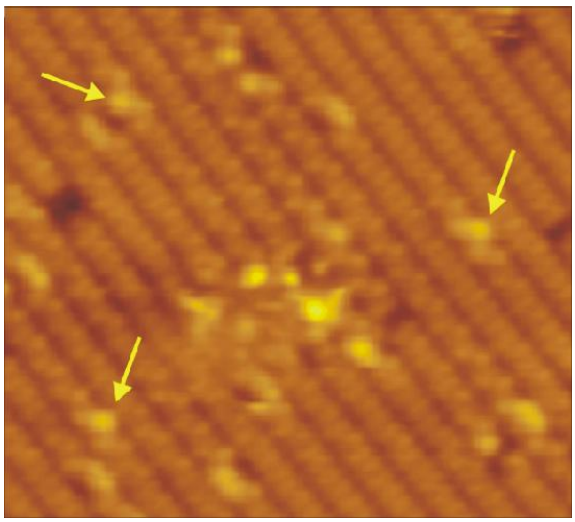

Figure 7-6 STM topographic image of the Si(100)-2x1 surface. Each arrows points at the unoccupied dangling bond of chlorine reacted dimer. Sample bias -2.0 V, current 0.3 nA

By looking at the bright dimers, it can be seen that the dimers around them in the same row are buckled (have zig-zag pattern). This is due to the freezing of the flip-flopping of the dimers because of the high electronegativity of the chlorines [122, 140].

There is another method for identifying chlorines on the surface. As reported by Boland [45] the hopping of chlorine atoms happens between two neighboring dangling-bonds sites of Si dimers on the Si(100)-2x1 surface. That is, the bright feature switches from one side of the dimer to the other. This process was further studied by Nakamura et al [140]. It was reported that no STM bias exists at which the chlorine hopping does not

occur. The maximum of hopping occurs at -0.75 and +1.25 V. Figure (7-7 A and B) shows two scans over the same area.

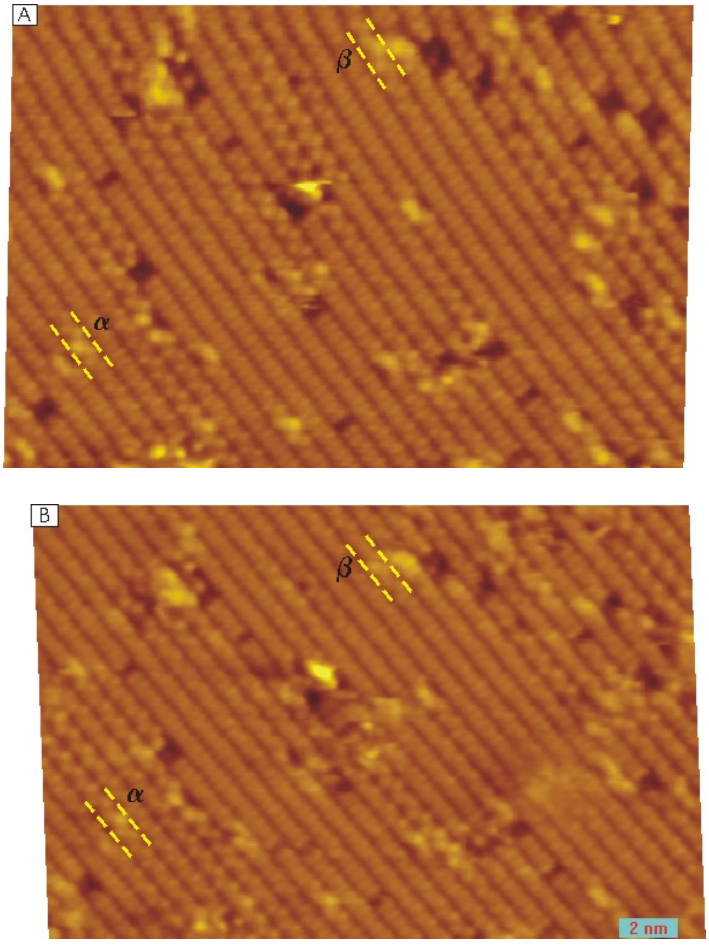

Figure 7-7 STM topographic images of the same area after exposure to 0.01L TCE at bias -2.0 V and 0.3 nA. One scan at -1.5 V was carried out in between these two images.

An area, common to both images, that contains a bound atom of chlorine has been labeled as α. In Figure (7-7 A) the chlorine atom is bound to the upper-right side of the dimer, leaving a bright feature associated with the Si dangling bond on the lower-left side

of the dimer. When the same area is scanned again, after a scan at -1.5 V, it can be seen that the chlorine (the dangling bond is circled) in α has hopped to the lower-left as seen in Figure (7-7 B). A similar hopping process is indicated with the label β as well.

With these pieces of evidence, the chlorines are identified by STM. This means that the chlorine dissociates from the TCE molecule showing that the TCE molecule upon interaction on the Si(100)-2x1 surface, dissociates just like the dissociation process on Si(111)-7x7.

As discussed before, the PCE molecule dissociates by dechlorination showing that the same process happens for the interaction of TCE on the Si(100)-2x1 surface. Dichloroethylene isomers (DCE) also dissociates upon interaction with the Si(100)-2x1 surface as reported by Leung's group [80, 81].

7.2.2 Chlorovinyl on Si(100)-2x1

The TCE molecule differs from the PCE molecule by having one less chlorine atom. As discussed earlier the TCE molecule undergoes dechlorination upon interaction with the Si(100)-2x1 surface.

The place where chlorine is bonded has been identified. The features are labeled in the Figure (7-8).

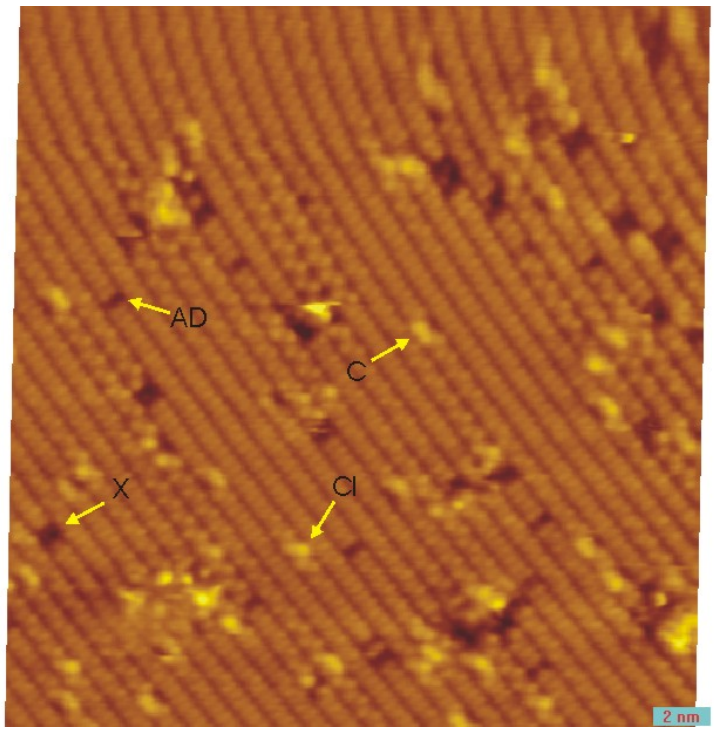

Figure 7-8 STM topographic image of the Si(100)-2x1 surface after 0.01L exposure to TCE. -2.0 V bias and 0.3 nA

Before dosing the surface with TCE, the surface was scanned and the cleanliness of the surface was checked. Clean and almost defect free surfaces were obtained after performing the cleaning procedure explained earlier. Using the defect density for Types A, B and C before dosing, the number of these defects can be estimated on the surface in Figure (7-8). The numbers for Type A, B and C defects on this surface are estimated as ~4, 1, and 12 respectively. The numbers of the Type A, B and C-like features in the Figure (7-8) are 10, 6, and 14 respectively. This indicates that the Type A-like features and Type B-like features are not defects as there are significantly more than what would

be expected from defects alone. The features on the surface are as follows. Cl feature is the chlorine binding site. C feature is the Type C defect explained in the section 6.1. AD is the "Asymmetric Dimer". This feature looks like a Type A defect with the difference that Type A defects are symmetric while this feature is asymmetric. X, is the feature which looks like a Type B defect.

Line scans have been performed on the AD features as shown in Figure (7-9). Line scans were used to extract cross-sections of data from the STM topographic images. Each line scan shows the topographic section of the line shown. Five nearest neighbors were involved in a weighted average to determine the section value at each pixel. Neighboring dimers (unreacted) show up as the high points on the far right and far left of each scan line.

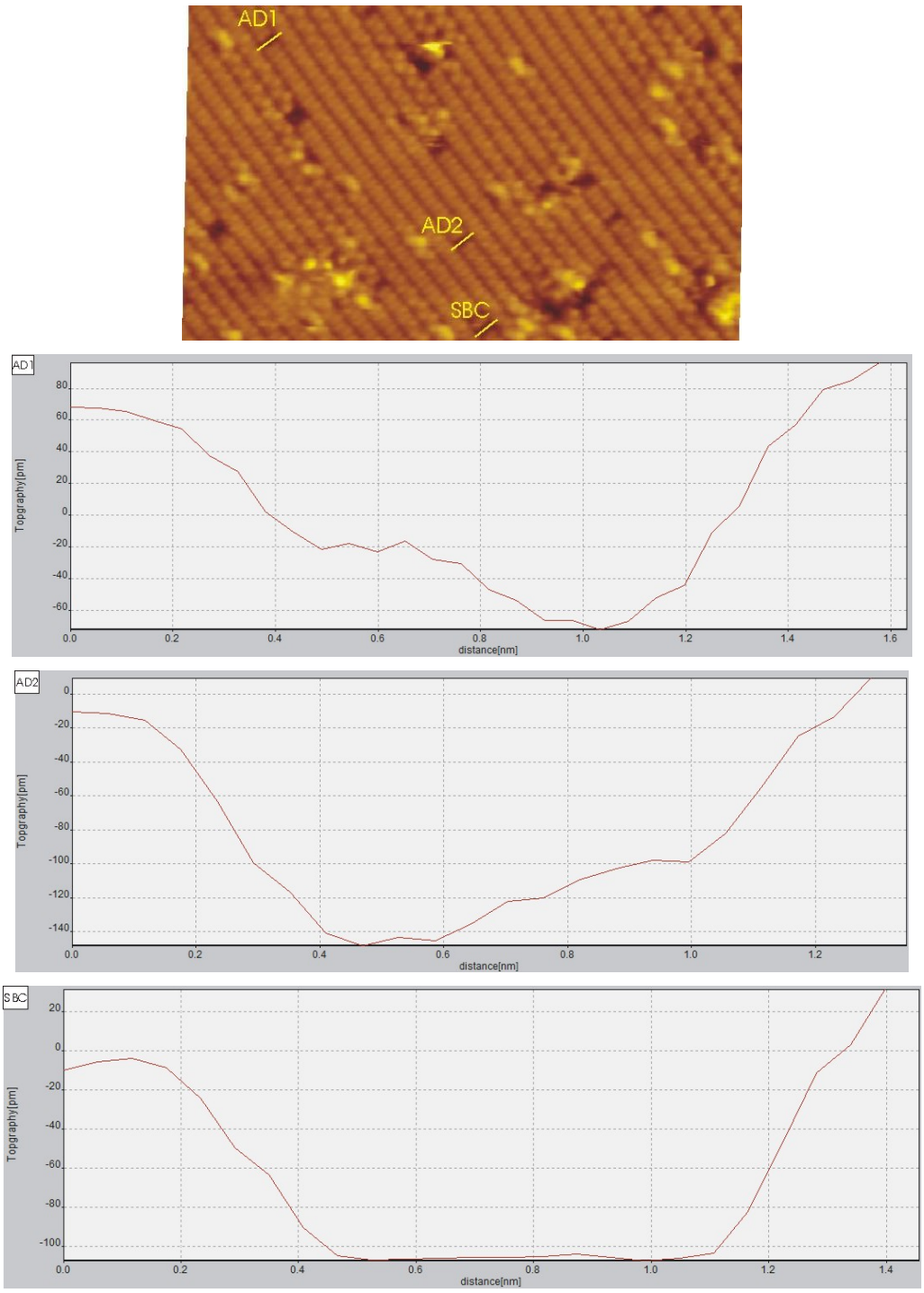

Figure 7-9 Scan lines on different dark (reacted) dimers. AD1,AD2 asymmetric; SBC symmetric dimer

The line scan for the AD1 feature is shown in Figure (7-9 AD1). As can be seen this dark dimer is not symmetric and it is higher on its middle left side. This asymmetry can be seen directly in the topographic image as well. The AD2 line is another asymmetric dark dimer, higher on the right side. These asymmetric dark dimers indicate that different types of binding exist on the two silicon atoms of the dimer. The proposed bonding configuration satisfying this condition is shown in Figure (7-10). This configuration is similar to one of Leung's proposed structures for PCE shown in Figure (6-10a). One TCE molecule dissociates and leaves a single-dimer footprint. Both of the original Si dangling bonds are saturated which leaves the dimer as a grey feature in STM topography. It is reasonable to assume that the brighter half of the reacted dimer is the side with the C_2HCl_2 product. The double bond on this product should contribute more tunnel current than the Si-Cl bond. It is well known that after benzene reacts with Si(100)-2x1 it forms a cyclohexadiene-like structure with two C=C double bonds that make the adsorbate very bright at -2.0 V bias [96-98]. The extreme brightness of this structure is attributed to the strain likely to be present in these C=C bonds. In the case of TCE the C=C bond is likely not very strained so a grey feature in STM seems reasonable.

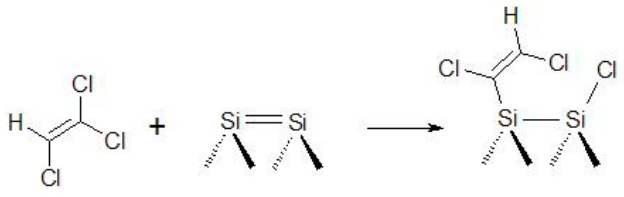

Figure 7-10 Schematic for the proposed binding configuration of TCE on Si(100)-2x1 forming an asymmetric dimer (AD1,AD2).

Line “SBC” is a line scan on a Symmetric Bonding Configuration. As can be seen in Figure (7-9 SBC) this feature is symmetric along the scanline. Corresponding to the symmetric dimers such as SBC, two proposed binding configurations are shown in Figure (7-11 I,II). Like the AD1 structure, the SBC structure has a one dimer footprint and leaves the Si-Si σ bond intact.

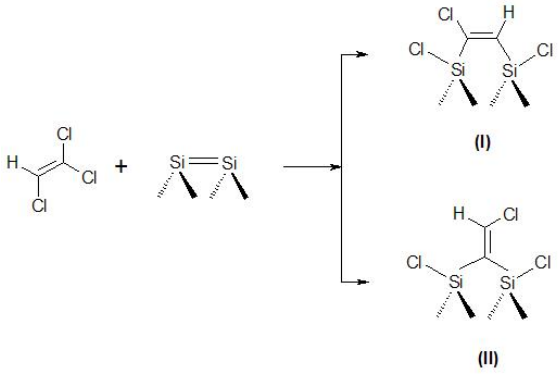

Figure 7-11 Schematic of binding configuration of TCE on Si(100)-2x1 surface forming a symmetric dimer

Both of the proposed structures I and II are symmetric and will saturate the Si dangling bonds. It is not clear if STM can distinguish which of the two structures are actually present. Ab initio density functional calculations could be performed to determine which structure is energetically favorable. It should be mentioned however that thermodynamically favorable structures are not always what result since kinetic barriers may dominate. Spectroscopic imaging may also shed light on this question.

X features resemble B defects, that is, they look like two dimer vacancies. As mentioned earlier the surfaces resulting from our cleaning procedure were very clean and no significant number of Type B defects were observed on the surface before exposure. For this reason it is tempting to attribute the X features to the X-bridge adstructure shown in Figure (6-10 e) for PCE. This PCE adstructure has a two dimer footprint with all four Si dangling bonds being saturated. Both Si-Si σ bonds are broken to facilitate this configuration. All four chlorines from the PCE must dissociate to form this X-bridge structure. This makes it difficult to form the analogous structure with TCE. Nevertheless the following adstructure for TCE is proposed (see Figure 7-12 A): The three chlorine atoms in the TCE dissociate from the molecule. On one of the dimers (lower one of Fig 7-12 A) both the π bond and the σ bond break, a carbon bonds to both silicon atoms and the two chlorine atoms bind to the two silicon atoms of that dimer. This dimer resembles that shown in Figure (7-11 II). The π bond breaks on the second dimer (upper one of Fig 7-12 A) while the σ bond stays intact. The carbon on the other side of the TCE binds to one of the silicon (dangling bond) on one side of the dimer and the dissociated chlorine bonds to the silicon (dangling bond) on the other side of the dimer (Figure (7-12 A)). Though this structure does saturate all the dangling bonds of two adjacent dimers, the structure is likely to be highly strained. In particular the top left adatom is not even close to being tetrahedrally bound.

One must consider the possibility that two TCE molecules form this X feature. A plausible configuration is shown in Figure 7-12 B. This resembles the configuration for

PCE shown in Fig 6-10 b). In one dimer the Si-Si σ bond is preserved while in the other dimer this bond is broken. Four of the six chlorines available dissociate. This adstructure would leave a two-dimer dark/grey feature in STM as observed.

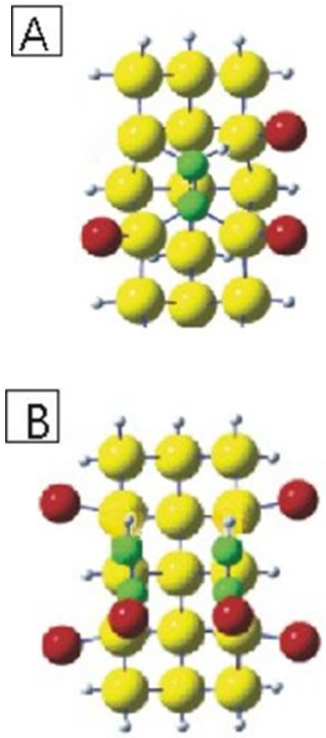

Figure 7-12 Schematic diagrams of the adsorption geometries of TCE on the Si(100)-2x1 surface. a) X-bridge; b) cross-dimer-bridge

Further studies are required to clarify whether the X feature contains one or two TCE molecules. One approach is to repeat these STM studies at lower TCE doses. At lower doses the frequency of observing two TCE molecules binding at the same point on the

surface will diminish greatly. If the double dimer features persist then we can safely conclude that they are due to single TCE molecule adsorption.

7.2.3 Summary

The procedure for cleaning the Si(100)-2x1 surface was explained. The atomic resolution capability of STM was used to determine the products of dissociation of TCE on the surface. The dissociation of chlorine was confirmed. From the STM images, different models for the various types of binding configurations were proposed.

Chapter 8

Summary, Conclusions and Future Work

8.1 Summary and Conclusion

In the category of molecular interaction of molecules with surfaces, dissociative interactions are one of the important types. It is of great importance to identify the products of dissociation. By studying the behavior, site preference and diffusion of the products of the dissociated molecule, one can take advantage of these properties for engineering devices of molecular size. For this to happen, one can use a variety of surface analysis techniques such as XPS, EELS, AES and TDS. The disadvantage of these methods is that the information obtained by these experiments is indirect and averaged over large surface areas. By probing the surfaces by the atomic-scale (real space) power of STM, information regarding the dissociation of molecules can be gained.

The first requirement for acquiring high quality images is to have sharp tips for the STM experiments. An easy and straightforward test, field emission, for testing the sharpness of STM tips was explained.

Careful optimization of the procedure for heating Si(111)-7x7 and Si(100)-2x1 was performed in order to obtain surfaces with low defect density. The procedure that resulted in the best surfaces for Si(111)-7x7 and Si(100)-2x1 was explained in detail.

Further, in this thesis the study of dissociation of molecules on silicon surfaces was reviewed. The interaction of ammonia and dimethylamine was explained on the Si(111)-

7x7 surface. The interaction of TCE on the Si(111)-7x7 surface was investigated using STM at the Surface Science Laboratory at the University of Lethbridge. The products of dissociation of TCE were identified. The dissociation of chlorine was confirmed. A strong site preference for chlorine on corner adatoms was found. Different types of binding configurations for the vinyl group and molecular adsorption was suggested by the observations done on the surface at the atomic level. No specific binding preference was observed for the dark features, though they are typically found well removed from the chlorine atoms. The result is a method for delivering atomic chlorine to the Si(111)7x7 surface suitable for basic studies.

The interaction of ammonia, methyl chloride and perchloroethylene was reviewed on the Si(100)-2x1 surface. The interaction of TCE on the Si(100)-2x1 surface was investigated using STM at the Surface Science Laboratory at the University of Lethbridge. The products of the dissociation of TCE were identified using STM. The dissociation of chlorine was confirmed. From the observations done on the surface at the atomic level, different types of binding configurations were suggested for the vinyl group.

8.2 Future Plans

8.2.1 Ordered Arrays on Silicon Surfaces

The high site selectivity of dissociated chlorine from a mobile molecular precursor onto the Si(111)7x7 surface allows for the potential in principle to deliver all kinds of atoms to

precise positions on a surface. This could result in the organized construction of templates that could be used for the fabrication of future integrated circuitry on the nanometer scale.

By further studying isomers of dichloroethylene on Si(100)-2x1, surface ordered arrays of vinylene and vinylidene proposed by Leung [80] can be confirmed by STM. By heating the TCE dosed Si(100)-2x1 surface, the vinyl group undergoes further dechlorination creating the interesting X-bridge structure. These structures can be used for fabricating templates on the Si(100)-2x1 surface for molecular electronics.

8.2.2 Spectroscopy Imaging on Dosed Surfaces

Using spectroscopy methods such as $(V/I)dI/dV$ and (dI/dZ) it might be possible to distinguish between the 1,2 dichlorovinyl and 2,2 dichlorovinyl groups bonded to the adatoms after the TCE exposure on the Si(111)-7x7 surface. Furthermore one can observe and verify whether the restatoms are involved in the interaction of TCE on Si(111)-7x7 surface as done for benzene and chlorobenzene on Si(111)-7x7 in our group[18].

Spectroscopic imaging can be used for better understanding of electronic structures of the asymmetric dimers on the Si(100)-2x1 surface as well.

Bibliography

1. Binning, G., H. Rohrer, C. Gerber, and E. Weibel, *Surface Studies by Scanning Tunneling Microscopy.* Physical Review Letters, 1982. **49**(1): p. 57-61.
2. Chen, C.J., *Introduction to Scanning Tunneling Microscopy*. 1993, New York: Oxford Univesity Press.
3. Schmid, M., 2005.
4. Hla, S.W., *Scanning tunneling microscopy single atom/molecule manipulation and its application to nanoscience and technology.* Journal of Vacuum Science & Technology B, 2005. **23**(4): p. 1351-1360.
5. Giambattista, B., C.G. Slough, W.W. McNairy, and R.V. Coleman, *Scanning tunneling microscopy of atoms and charge-density waves in T-TaS_2, T-$TaSe_2$, and T-VSe_2.* Physical Review B, 1990. **41**(14): p. 10082.
6. Coleman, R.V., B. Drake, B. Giambattista, A. Johnson, P.K. Hansma, W.W. McNairy, and G. Slough, *Applications of Scanning Tunneling Microscopy to the Study of Charge-Density Waves.* Physica Scripta, 1988. **38**(2): p. 235-243.
7. Kanai, T.K.a.M., *Superconductivity and scanning tunneling microscopy (STM) / spectroscopy (STS) of transition metal oxide artificial lattices.* Journal of Low Temperature Physics, 1996. **105**: p. 1349-1358.
8. Kacmarcik, J., P. Szabo, P. Samuely, J.G. Rodrigo, H. Suderow, S. Vieira, A. Lafond, and A. Meerschaut, *Scanning tunneling microscopy and spectroscopy of (LaSe)(1.14)(NbSe2) at very low temperatures and in magnetic field.* Czechoslovak Journal of Physics, 2004. **54**: p. D489-D492.
9. Feenstra, R.M., J.A. Stroscio, and A.P. Fein, *Tunneling Spectroscopy of the Si(111)2x1 Surface.* Surface Science, 1987. **181**(1-2): p. 295-306.
10. Feenstra, R.M., A.J. Slavin, G.A. Held, and M.A. Lutz, *Surface-Diffusion and Phase-Transition on the Ge(111) Surface Studied by Scanning Tunneling Microscopy.* Physical Review Letters, 1991. **66**(25): p. 3257-3260.
11. Berndt, R., J.K. Gimzewski, and R.R. Schlittler, *Enhanced Photon-Emission from the Stm - a General Property of Metal-Surfaces.* Ultramicroscopy, 1992. **42**: p. 355-359.
12. Barth, J.V., H. Brune, G. Ertl, and R.J. Behm, *Scanning Tunneling Microscopy Observations on the Reconstructed Au(111) Surface - Atomic-Structure, Long-Range Superstructure, Rotational Domains, and Surface-Defects.* Physical Review B, 1990. **42**(15): p. 9307-9318.
13. Grubb, M., H. Wackerbarth, J. Wengel, and J. Ulstrup, *Direct imaging of hexaamine-ruthenium(III) in domain boundaries in monolayers of single-stranded DNA.* Langmuir, 2007. **23**(3): p. 1410-1413.
14. Rogers, D.M., *Scanning Tunneling Microscopy Study of Surfaces in Ultra High Vaccum*, Ph.D. Thesis, 1994, Department of Physics, The University of British Columbia

15. Kubby, J.A. and J.J. Boland, *Scanning tunneling microscopy of semiconductor surfaces.* Surface Science Reports, 1996. **26**(3-6): p. 61-204.
16. Tersoff, J. and D.R. Hamann, *Theory of the Scanning Tunneling Microscope.* Physical Review B, 1985. **31**(2): p. 805-813.
17. Tersoff, J. and D.R. Hamann, *Theory and Application for the Scanning Tunneling Microscope.* Physical Review Letters, 1983. **50**(25): p. 1998-2001.
18. Horn, S.A., *Construction of an STM Capable of Precise Studies of Adsorbates on Silicon Surfaces*, M.Sc. Thesis, 2006, Department of Physics, University of Lethbridge.
19. Ibe, J.P., P.P. Bey, S.L. Brandow, R.A. Brizzolara, N.A. Burnham, D.P. Dilella, K.P. Lee, C.R.K. Marrian, and R.J. Colton, *On the Electrochemical Etching of Tips for Scanning Tunneling Microscopy.* Journal of Vacuum Science & Technology a-Vacuum Surfaces and Films, 1990. **8**(4): p. 3570-3575.
20. Neil W. Ashcroft and N.D. Mermin, *Solid State Physics*. 1976: Brooks Cole.
21. Fowler, R.H. and L. Nordheim, *Electron emission in intense electric fields.* Proceedings of the Royal Society of London Series a-Containing Papers of a Mathematical and Physical Character, 1928. **119**(781): p. 173-181.
22. Schottky, W., *Concerning cold and hot electron discharge.* Zeitschrift Fur Physik, 1923. **14**: p. 63-106.
23. Nordheim, L.W., *The Effect of the Image Force on the Emission and Reflexion of Electrons by Metals.* Proceedings of the Royal Society of London. Series A, Containing Papers of a Mathematical and Physical Character, 1928. **121**(788): p. 626-639.
24. R. H. Good jr. and E.W. Muller, *Field Emission*. Handbuch Der Physik, ed. S. Flugge. Vol. 21. 1956, Berlin: Springer-Verlag.
25. Dolan, W.W. and W.P. Dyke, *Temperature-and-Field Emission of Electrons from Metals.* Physical Review, 1954. **95**(2): p. 327-332.
26. Dolan, W.W., *Current Density Tables for Field Emission Theory.* Physical Review, 1953. **91**(3): p. 510-511.
27. K. C. Li and C.Y. Wang., *Tungsten: Its History, Geology, Ore-Dressing, Metallurgy, Chemistry, Analysis, Applications, and Economics*. 3rd edition ed. 1955: Reinhold Publishing Corporation.
28. Gomer, R., *Field Emission and Field Ionization*. Number 9 in Harvard Monographs in Applied Science. 1961: Harvard University Press.
29. Griffiths, D.J., *Introduction To Electrodynamics*. Second ed. 1989, New Jersey: Prentice Hall.
30. Binh, V.T., *Insitu Fabrication and Regeneration of Microtips for Scanning Tunnelling Microscopy.* Journal of Microscopy-Oxford, 1988. **152**: p. 355-361.
31. Binh, V.T. and J. Marien, *Characterization of Microtips for Scanning Tunneling Microscopy.* Surface Science, 1988. **202**(1-2): p. L539-L549.
32. Schirmeisen., A., Metallic Adhesion and Tunneling at the Atomic Scale, 1999, McGill University

33. Lucier, A.-S., *Preparation and Characterization of Tungsten Tips Suitable for Molecular Electronics Studies*, M.Sc. Thesis, 2004, Department of Physics, McGill University
34. Fursey, G.N. and D.V. Glazanov, *Deviations from the Fowler-Nordheim theory and peculiarities of field electron emission from small-scale objects.* Journal of Vacuum Science & Technology B, 1998. **16**(2): p. 910-915.
35. Takayanagi, K., Y. Tanishiro, M. Takahashi, and S. Takahashi, *Structural-Analysis of Si(111)-7x7 by UHV-Transmission Electron-Diffraction and Microscopy.* Journal of Vacuum Science & Technology a-Vacuum Surfaces and Films, 1985. **3**(3): p. 1502-1506.
36. Waltenburg, H.N. and J.T. Yates, *Surface-Chemistry of Silicon.* Chemical Reviews, 1995. **95**(5): p. 1589-1673.
37. Brommer, K.D., B.E. Larson, M. Needels, and J.D. Joannopoulos, *Modeling Large Surface Reconstructions on the Connection Machine.* Japanese Journal of Applied Physics Part 1-Regular Papers Short Notes & Review Papers, 1993. **32**(3B): p. 1360-1367.
38. Brommer, K.D., M. Needels, B.E. Larson, and J.D. Joannopoulos, *Abinitio Theory of the Si(111)-(7x7) Surface Reconstruction - a Challenge for Massively Parallel Computation.* Physical Review Letters, 1992. **68**(9): p. 1355-1358.
39. Brommer, K.D., M. Galvan, A. Dalpino, and J.D. Joannopoulos, *Theory of Adsorption of Atoms and Molecules on Si(111)-(7x7).* Surface Science, 1994. **314**(1): p. 57-70.
40. Hamers, R.J., R.M. Tromp, and J.E. Demuth, *Electronic and Geometric Structure of Si(111)-(7x7) and Si(001) Surfaces.* Surface Science, 1987. **181**(1-2): p. 346-355.
41. Hamers, R.J., R.M. Tromp, and J.E. Demuth, *Surface Electronic-Structure of Si(111)-(7 X 7) Resolved in Real Space.* Physical Review Letters, 1986. **56**(18): p. 1972-1975.
42. Hamers, R.J. and Y.J. Wang, *Atomically-resolved studies of the chemistry and bonding at silicon surfaces.* Chemical Reviews, 1996. **96**(4): p. 1261-1290.
43. Radny, M.W., P.V. Smith, and P.L. Cao, *An ab initio Hartree-Fock/density functional study of the cluster simulated Si(111)7x7:Cl adsorption system.* Surface Science, 1996. **365**(1): p. 15-28.
44. Whitman, L.J., S.A. Joyce, J.A. Yarmoff, F.R. McFeely, and L.J. Terminello, *The Chemisorption of Chlorosilanes and Chlorine on Si(111)7x7.* Surface Science, 1990. **232**(3): p. 297-306.
45. Boland, J.J., *Manipulating Chlorine Atom Bonding on the Si(100)-(2x1) Surface with the STM.* Science, 1993. **262**(5140): p. 1703-1706.
46. Villarrubia, J.S. and J.J. Boland, *Scanning-Tunneling-Microscopy Study of the Si(111)-7x7 Rest-Atom Layer Following Adatom Removal by Reaction with Cl.* Physical Review Letters, 1989. **63**(3): p. 306-309.

47. Baba, M. and S. Matsui, *Atomic Modification of an Si(111)7x7 Surface with Adsorbed Chlorine Atoms Using a Scanning Tunneling Microscope.* Applied Physics Letters, 1994. **65**(15): p. 1927-1929.
48. Boland, J.J. and J.S. Villarrubia, *Formation of Si(111)-(1x1)Cl.* Physical Review B, 1990. **41**(14): p. 9865-9870.
49. Schluter, M. and M.L. Cohen, *Nature of Conduction-Band Surface Resonances for Si(111) Surfaces with and without Chemisorbed Overlayers.* Physical Review B, 1978. **17**(2): p. 716-725.
50. Nakamura, Y., Y. Mera, and K. Maeda, *Diffusion of chlorine atoms on Si(111)-(7x7) surface enhanced by electron injection from scanning tunneling microscope tips.* Surface Science, 2001. **487**(1-3): p. 127-134.
51. Nakamura, Y., Y. Mera, and K. Maeda, *Chlorine atom diffusion on Si(111)-(7 x 7) surface enhanced by hole injection from scanning tunneling microscope tips.* Surface Science, 2002. **497**(1-3): p. 166-170.
52. Nakamura, Y., Y. Mera, and K. Maeda, *Nanoscale imaging of electronic surface transport probed by atom movements induced by scanning tunneling microscope current.* Physical Review Letters, 2002. **89**(26).
53. Stroscio, J.A. and D.M. Eigler, *Atomic and Molecular Manipulation with the Scanning Tunneling Microscope.* Science, 1991. **254**(5036): p. 1319-1326.
54. Avouris, P., R.E. Walkup, A.R. Rossi, H.C. Akpati, P. Nordlander, T.C. Shen, G.C. Abeln, and J.W. Lyding, *Breaking individual chemical bonds via STM-induced excitations.* Surface Science, 1996. **363**(1-3): p. 368-377.
55. Bartels, L., G. Meyer, K.H. Rieder, D. Velic, E. Knoesel, A. Hotzel, M. Wolf, and G. Ertl, *Dynamics of electron-induced manipulation of individual CO molecules on Cu(111).* Physical Review Letters, 1998. **80**(9): p. 2004-2007.
56. Patitsas, S.N., G.P. Lopinski, O. Hul'ko, D.J. Moffatt, and R.A. Wolkow, *Current-induced organic molecule-silicon bond breaking: consequences for molecular devices.* Surface Science, 2000. **457**(3): p. L425-L431.
57. Rezaei, M.A., B.C. Stipe, and W. Ho, *Inducing and imaging single molecule dissociation on a semiconductor surface: H2S and D2S on Si(111)-7x7.* Journal of Chemical Physics, 1998. **109**(14): p. 6075-6078.
58. Wolkow, R. and P. Avouris, *Atom-Resolved Surface-Chemistry Using Scanning Tunneling Microscopy.* Physical Review Letters, 1988. **60**(11): p. 1049-1052.
59. Avouris, P. and R. Wolkow, *Atom-Resolved Surface-Chemistry Studied by Scanning Tunneling Microscopy and Spectroscopy.* Physical Review B, 1989. **39**(8): p. 5091-5100.
60. Tanaka, S., M. Onchi, and M. Nishijima, *Amino Species on the Si(111)(7 X 7) Surface - Observation by Vibrational Eels.* Surface Science, 1987. **191**(1-2): p. L756-L764.
61. Bozso, F. and P. Avouris, *Photoemission-Studies of the Reactions of Ammonia and N-Atoms with Si(100)-(2x1) and Si(111)-(7x7) Surfaces.* Physical Review B, 1988. **38**(6): p. 3937-3942.

62. Bozso, F. and P. Avouris, *Thermal and Electron-Beam-Induced Reaction of Disilane on Si(100)-(2x1).* Physical Review B, 1988. **38**(6): p. 3943-3947.
63. Dufour, G., F. Rochet, H. Roulet, and F. Sirotti, *Contrasted Behavior of Si(001) and Si(111) Surfaces with Respect to NH_3 Adsorption and Thermal Nitridation - a N 1s and Si 2p Core-Level Study with Synchrotron-Radiation.* Surface Science, 1994. **304**(1-2): p. 33-47.
64. Wu, C.L., J.L. Hsieh, H.D. Hsueh, and S. Gwo, *Thermal nitridation of the Si(111)-(7X7) surface studied by scanning tunneling microscopy and spectroscopy.* Physical Review B, 2002. **65**(4).
65. Cao, X.P. and R.J. Hamers, *Molecular and dissociative bonding of amines with the Si(111)-(7 x 7) surface.* Surface Science, 2003. **523**(3): p. 241-251.
66. Cao, X.P. and R.J. Hamers, *Silicon surfaces as electron acceptors: Dative bonding of amines with Si(001) and Si(111) surfaces.* Journal of the American Chemical Society, 2001. **123**(44): p. 10988-10996.
67. Hansson, G.V. and R.I.G. Uhrberg, *Photoelectron-Spectroscopy of Surface-States on Semiconductor Surfaces.* Surface Science Reports, 1988. **9**(5-6): p. 197-292.
68. Bjorkqvist, M., M. Gothelid, T.M. Grehk, and U.O. Karlsson, *NH3 on Si(111)7x7: Dissociation and surface reactions.* Physical Review B, 1998. **57**(4): p. 2327-2333.
69. Uhrberg, R.I.G., T. Kaurila, and Y.C. Chao, *Low-temperature photoemission study of the surface electronic structure of Si(111)7x7.* Physical Review B, 1998. **58**(4): p. R1730-R1733.
70. Mortensen, K., D.M. Chen, P.J. Bedrossian, J.A. Golovchenko, and F. Besenbacher, *2 Reaction Channels Directly Observed for Atomic-Hydrogen on the Si(111)-7x7 Surface.* Physical Review B, 1991. **43**(2): p. 1816-1819.
71. Boland, J.J., *The Importance of Structure and Bonding in Semiconductor Surface-Chemistry - Hydrogen on the Si(111)-7x7 Surface.* Surface Science, 1991. **244**(1-2): p. 1-14.
72. M.B. Moran, L.F.J., Mater. Res. Soc. Sympos. Proc, 2000. **609**.
73. Huang, Q.A., J.N. Chen, H.Z. Zhang, and Q.Y. Tong, *Improvement of Bonded Silicon-on-Insulator Using TCE-Grown Oxide as Buried SiO_2.* Japanese Journal of Applied Physics Part 1-Regular Papers Short Notes & Review Papers, 1993. **32**(6A): p. 2854-2855.
74. Hochberg, A.K., A. Lagendijk, D.A. Roberts, R. Agny, B. Anders, R. Cotner, J. Jewett, J. Mulready, M. Tran, B.B. Triplett, and P. Wermer, *A New Liquid Chlorine Source for Silicon Oxidation.* Journal of the Electrochemical Society, 1992. **139**(12): p. L117-L118.
75. Grassian, V.H. and G.C. Pimentel, *The Structures of Cis-Dichloroethene and Trans-Dichloroethene Adsorbed on Pt(111).* Journal of Chemical Physics, 1988. **88**(7): p. 4478-4483.

76. Yang, M.X., P.W. Kash, D.H. Sun, G.W. Flynn, B.E. Bent, M.T. Holbrook, S.R. Bare, D.A. Fischer, and J.L. Gland, *Chemistry of chloroethylenes on Cu(100): Bonding and reactions.* Surface Science, 1997. **380**(2-3): p. 151-164.
77. Cassuto, A., M.B. Hugenschmidt, P. Parent, C. Laffon, and H.G. Tourillon, *A NEXAFS and UPS Study of the Adsorption of Tetrachloroethylene, Trichloroethylene, Iso-Dichloroethylene, Cis-Dichloroethylene, and Trans-Dichloroethylene on Platinum Surfaces at 95-K - Multilayers and Monolayers.* Surface Science, 1994. **310**(1-3): p. 390-398.
78. He, Z.H., Q. Li, and K.T. Leung, *Room-temperature chemisorption and thermal evolution of 1,1-dichloroethylene and monochloroethylene on Si(111)7x7: Formation of vinylidene and vinylene adspecies.* Journal of Physical Chemistry B, 2005. **109**(31): p. 14908-14916.
79. He, Z.H., Q. Li, and K.T. Leung, *Isomeric effects on room-temperature chemisorption and thermal evolution of iso-, cis- and trans-dichloroethylene on Si(111)7x7.* Surface Science, 2006. **600**(3): p. 514-526.
80. Zhou, X.J., Z.H. He, and K.T. Leung, *Formation of vinylidene and vinylene by selective reactivity of Si(100)2 x 1 towards iso, cis and trans isomers of dichloroethylene.* Surface Science, 2006. **600**(2): p. 468-477.
81. Zhou, X.J., Q. Li, and K.T. Leung, *Formation of C=C and Si-Cl adstructures by insertion reactions of cis-dichloroethylene and perchloroethylene on Si(100)2x1.* Journal of Physical Chemistry B, 2006. **110**(11): p. 5602-5610.
82. He, Z.H., X. Yang, X.J. Zhou, and K.T. Leung, *Room-temperature chemisorption of chloroethylenes on Si(111)7 x 7: formation of surface vinyl, vinylidene and their chlorinated derivatives.* Surface Science, 2003. **547**(1-2): p. L840-L846.
83. He, Z.H. and K.T. Leung, *Room-temperature chemisorption and thermal evolution of perchloroethylene and trichloroethylene on Si(111)7x7: Formation of chlorinated vinylene and vinylidene and acetylide adspecies, and thermal etching reactions.* Surface Science, 2005. **583**(2-3): p. 179-190.
84. Maraghechi, P., S.A. Horn, and S.N. Patitsas, *Site selective atomic chlorine adsorption on the Si(1 1 1)7 x 7 surface.* Surface Science, 2007. **601**(1): p. L1-L5.
85. Ukraintsev, V.A., Z. Dohnalek, and J.T. Yates, *Electronic characterization of defect sites on Si(001)-(2x1) by STM.* Surface Science, 1997. **388**(1-3): p. 132-140.
86. Kern, W. and D.A. Puotinen, *Cleaning Solutions Based on Hydrogen Peroxide for Use in Silicon Semiconductor Technology.* RCA Review, 1970. **31**(2): p. 187-&.
87. Faktor, J.I.C.a.M.M., *The Electrochemistry of Semiconductors*. 1962: P. J. Holmes, Ed., Academic Press.
88. Lander, J.J. and J. Morrison, *Low Voltage Electron Diffraction Study of Oxidation and Reduction of Silicon.* Journal of Applied Physics, 1962. **33**(6): p. 2089-&.
89. Shimada, W., H. Tochihara, T. Sato, and M. Iwatsuki, *Transformations of faulted halves of the DAS structure on quenched Si(111).* Surface Science, 1999. **423**(2-3): p. L291-L298.

90. Yan, C., J.A. Jensen, and A.C. Kummel, *The Effect of Incident Energy Upon Adsorbate Structure for Cl_2 Chemisorption onto Si(111)-7x7 Surfaces.* Journal of Chemical Physics, 1995. **102**(8): p. 3381-3390.
91. Sakurai, T., Y. Hasegawa, T. Hashizume, I. Kamiya, T. Ide, I. Sumita, H.W. Pickering, and S. Hyodo, *Atomic-Hydrogen Chemisorption on the Si(111)7x7 Surface.* Journal of Vacuum Science & Technology a-Vacuum Surfaces and Films, 1990. **8**(1): p. 259-261.
92. Rogers, D. and T. Tiedje, *Binding energies of hydrogen to the Si(111) 7x7 surface studied by statistical scanning tunneling microscopy.* Physical Review B, 1996. **53**(20): p. 13227-13230.
93. King, D.A. and M.G. Wells, *Reaction-Mechanism in Chemisorption Kinetics - Nitrogen on (100) Plane of Tungsten.* Proceedings of the Royal Society of London Series a-Mathematical Physical and Engineering Sciences, 1974. **339**(1617): p. 245-269.
94. Lyubinetsky, I., Z. Dohnalek, W.J. Choyke, and J.T. Yates, *Cl_2 dissociation on Si(100)-(2x1): A statistical study by scanning tunneling microscopy.* Physical Review B, 1998. **58**(12): p. 7950-7957.
95. Brown, D.E., D.J. Moffatt, and R.A. Wolkow, *Isolation of an intrinsic precursor to molecular chemisorption.* Science, 1998. **279**(5350): p. 542-544.
96. Lopinski, G.P., D.J. Moffatt, and R.A. Wolkow, *Benzene/Si(100): metastable chemisorption and binding state conversion.* Chemical Physics Letters, 1998. **282**(3-4): p. 305-312.
97. Wolkow, R.A., G.P. Lopinski, and D.J. Moffatt, *Resolving organic molecule silicon scanning tunneling microscopy features with molecular orbital methods.* Surface Science, 1998. **416**(3): p. L1107-L1113.
98. Hofer, W.A., A.J. Fisher, and R.A. Wolkow, *Adsorption sites and STM images of C_2H_2 on Si(100): a first principles study.* Surface Science, 2001. **475**(1-3): p. 83-88.
99. Schlier, R.E. and H.E. Farnsworth, *Structure and Adsorption Characteristics of Clean Surfaces of Germanium and Silicon.* Journal of Chemical Physics, 1959. **30**(4): p. 917-926.
100. Seiwatz, R., *Possible Structures for Clean, Annealed Surfaces of Germanium and Silicon.* Surface Science, 1964. **2**: p. 473-483.
101. Phillips, J.C., *Excitonic Instabilities, Vacancies, and Reconstruction of Covalent Surfaces.* Surface Science, 1973. **40**(3): p. 459-469.
102. Appelbaum, J.A., G.A. Baraff, and D.R. Hamann, *GaAs(100) - Its Spectrum, Effective Charge, and Reconstruction Patterns.* Physical Review B, 1976. **14**(4): p. 1623-1632.
103. Appelbaum, J.A., G.A. Baraff, D.R. Hamann, H.D. Hagstrum, and T. Sakurai, *Hydrogen Chemisorption on 100 (2x1) Surfaces of Si and Ge.* Surface Science, 1978. **70**(1): p. 654-673.

104. Chadi, D.J., *Atomic and Electronic-Structures of Reconstructed Si(100) Surfaces.* Physical Review Letters, 1979. **43**(1): p. 43-47.
105. Hamers, R.J., P. Avouris, and F. Bozso, *Imaging of Chemical-Bond Formation with the Scanning Tunneling Microscope - NH_3 Dissociation on Si(001).* Physical Review Letters, 1987. **59**(18): p. 2071-2074.
106. Wang, Y.J., M.J. Bronikowski, and R.J. Hamers, *Direct Dimer-by-Dimer Identification of Clean and Monohydride Dimers on the Si(001) Surface by Scanning-Tunneling-Microscopy.* Journal of Vacuum Science & Technology a-Vacuum Surfaces and Films, 1994. **12**(4): p. 2051-2057.
107. Appelbaum, J.A., G.A. Baraff, and D.R. Hamann, *Si (100) Surface .3. Surface Reconstruction.* Physical Review B, 1976. **14**(2): p. 588-601.
108. Flowers, M.C., N.B.H. Jonathan, Y. Liu, and A. Morris, *Temperature-Programmed Desorption of Molecular-Hydrogen from a Si(100)-2x1 Surface - Theory and Experiment.* Journal of Chemical Physics, 1993. **99**(9): p. 7038-7048.
109. Weast, R.C., *CRC Handbook of Chemistry and Physics*. 64th ed. 1983: CRC Press.
110. Dobbs, K.D. and W.J. Hehre, *Pi-Bond Strengths in Main-Group Olefin Analogs.* Organometallics, 1986. **5**(10): p. 2057-2061.
111. Levine, J.D., *Structural and Electronic Model of Negative Electron Affinity on Si-Cs-O Surface.* Surface Science, 1973. **34**(1): p. 90-107.
112. Hamers, R.J., R.M. Tromp, and J.E. Demuth, *Scanning Tunneling Microscopy of Si(001).* Physical Review B, 1986. **34**(8): p. 5343-5357.
113. Tromp, R.M., R.J. Hamers, and J.E. Demuth, *Si(001) Dimer Structure Observed with Scanning Tunneling Microscopy.* Physical Review Letters, 1985. **55**(12): p. 1303-1306.
114. Wolkow, R.A., *Direct Observation of an Increase in Buckled Dimers on Si(001) at Low-Temperature.* Physical Review Letters, 1992. **68**(17): p. 2636-2639.
115. Wang, Y.J., M.J. Bronikowski, and R.J. Hamers, *An Atomically Resolved Scanning-Tunneling-Microscopy Study of the Thermal-Decomposition of Disilane on Si(001).* Surface Science, 1994. **311**(1-2): p. 64-100.
116. Larsson, C.U.S. and A.S. Flodstrom, *Dissociative NH_3 Adsorption on the Si(100)2x1 Surface at 300-K.* Surface Science, 1991. **241**(3): p. 353-356.
117. Larsson, C.U.S., C.B.M. Andersson, N.P. Prince, and A.S. Flodstrom, *Si(100)2 X-1 - the Clean and Ammonia Exposed Surface Studied with High-Resolution Core-Level Spectroscopy.* Surface Science, 1992. **271**(3): p. 349-354.
118. Bozso, F. and P. Avouris, *Reaction of Si(100) with NH_3 - Rate-Limiting Steps and Reactivity Enhancement Via Electronic Excitation.* Physical Review Letters, 1986. **57**(9): p. 1185-1188.
119. Avouris, P., F. Bozso, and R.J. Hamers, *The Reaction of Si(100) 2x1 with NO and NH_3 - the Role of Surface Dangling Bonds.* Journal of Vacuum Science & Technology B, 1987. **5**(5): p. 1387-1392.

120. Ciraci, S., R. Butz, E.M. Oellig, and H. Wagner, *Chemisorption of Hydrogen on the Si(100) Surface - Monohydride and Dihydride Phases.* Physical Review B, 1984. **30**(2): p. 711-720.
121. Maruno, S., H. Iwasaki, K. Horioka, S.T. Li, and S. Nakamura, *Electronic-Structures of the Monohydride (2x1)-H and the Dihydride (1x1)-2H Si(001) Surfaces Studied by Angle-Resolved Electron-Energy-Loss Spectroscopy.* Physical Review B, 1983. **27**(7): p. 4110-4116.
122. Bronikowski, M.J. and R.J. Hamers, *Atomically Resolved Scanning-Tunneling-Microscopy Study of the Adsorption and Dissociation of Methylchloride on Si(001).* Journal of Vacuum Science & Technology A-Vacuum Surfaces and Films, 1995. **13**(3): p. 777-781.
123. Brown, K.A. and W. Ho, *The Interaction of Methyl-Chloride and Si(100)-2x1.* Surface Science, 1995. **338**(1-3): p. 111-116.
124. Gao, Q., C.C. Cheng, P.J. Chen, W.J. Choyke, and J.T. Yates, *Chlorine Bonding Sites and Bonding Configurations on Si(100)-(2x1).* Journal of Chemical Physics, 1993. **98**(10): p. 8308-8323.
125. Gao, Q., C.C. Cheng, P.J. Chen, W.J. Choyke, and J.T. Yates, *Comparison of Cl2 and Hcl Adsorption on Si(100)-(2 X-1).* Thin Solid Films, 1993. **225**(1-2): p. 140-144.
126. Colaianni, M.L., P.J. Chen, H. Gutleben, and J.T. Yates, *Vibrational Studies of CH_3 on Si(100)-(2x1) - Adsorption and Decomposition of the Methyl Species.* Chemical Physics Letters, 1992. **191**(6): p. 561-568.
127. Rueter, M.A. and J.M. Vohs, *Surface-Reactions in the Decomposition of Dimethylzinc on Si(100)-2x1.* Journal of Vacuum Science & Technology a-Vacuum Surfaces and Films, 1991. **9**(6): p. 2916-2922.
128. Woelke, A., S. Imanaka, S. Watanabe, S. Goto, M. Hashinokuchi, M. Okada, and T. Kasai, *Dissociative adsorption of methyl chloride on Si(001) studied by scanning tunneling microscopy.* Journal of Electron Microscopy, 2005. **54**: p. I21-I24.
129. Romero, A.H., C. Sbraccia, P.L. Silvestrelli, and F. Ancilotto, *Adsorption of methylchloride on Si(100) from first principles.* Journal of Chemical Physics, 2003. **119**(2): p. 1085-1092.
130. Hamers, R.J. and U.K. Kohler, *Determination of the Local Electronic-Structure of Atomic-Sized Defects on Si(001) by Tunneling Spectroscopy.* Journal of Vacuum Science & Technology a-Vacuum Surfaces and Films, 1989. **7**(4): p. 2854-2859.
131. Chander, M., Y.Z. Li, J.C. Patrin, and J.H. Weaver, *Si(100)-(2x1) Surface-Defects and Dissociative and Nondissociative Adsorption of H_2O Studied with Scanning-Tunneling-Microscopy.* Physical Review B, 1993. **48**(4): p. 2493-2499.
132. Hata, K., T. Kimura, S. Ozawa, and H. Shigekawa, *How to fabricate a defect free Si(001) surface.* Journal of Vacuum Science & Technology A-Vacuum Surfaces and Films, 2000. **18**(4): p. 1933-1936.

133. Ukraintsev, V.A. and J.T. Yates, *The role of nickel in Si(001) roughening.* Surface Science, 1996. **346**(1-3): p. 31-39.
134. Casaletto, M.P., R. Zanoni, M. Carbone, M.N. Piancastelli, L. Aballe, K. Weiss, and K. Horn, *Ethylene adsorption on Si(100)2x1: A high-resolution photoemission study.* Physical Review B, 2000. **62**(24): p. 17128-17133.
135. Clemen, L., R.M. Wallace, P.A. Taylor, M.J. Dresser, W.J. Choyke, W.H. Weinberg, and J.T. Yates, *Adsorption and Thermal-Behavior of Ethylene on Si(100)-(2x1).* Surface Science, 1992. **268**(1-3): p. 205-216.
136. Huang, C., W. Widdra, and W.H. Weinberg, *Adsorption of Ethylene on the Si(100)-(2x1) Surface.* Surface Science, 1994. **315**(1-2): p. L953-L958.
137. Mayne, A.J., A.R. Avery, J. Knall, T.S. Jones, G.A.D. Briggs, and W.H. Weinberg, *An STM Study of the Chemisorption of C_2H_4 on Si(001)(2x1).* Surface Science, 1993. **284**(3): p. 247-256.
138. Filler, M.A. and S.F. Bent, *The surface as molecular reagent: organic chemistry at the semiconductor interface.* Progress in Surface Science, 2003. **73**(1-3): p. 1-56.
139. Cheng, C.C., R.M. Wallace, P.A. Taylor, W.J. Choyke, and J.T. Yates, *Direct Determination of Absolute Monolayer Coverages of Chemisorbed C_2H_2 and C_2H_4 on Si(100).* Journal of Applied Physics, 1990. **67**(8): p. 3693-3699.
140. Nakamura, Y., Y. Mera, and K. Maeda, *Hopping motion of chlorine atoms on Si(100)-(2 x 1) surfaces induced by carrier injection from scanning tunneling microscope tips.* Surface Science, 2003. **531**(1): p. 68-76.
141. Robert L. Park and M.G. Lagally, *Methods of Experimental Physics*. 1985, Toronto: Academic Press.

Appendix A

Fermi-Dirac Distribution

Consider volume υ of a metal, which has n_i electrons that have energies ε_i distributed in g_i states. From Fermi-Dirac statistics it is known that n_i particles can be distributed in $\frac{g_i!}{n_i!(g_i - n_i)!}$ ways among g_i states. So the total number of ways that this system can be arranged is

$$\omega = \prod_i \frac{g_i!}{n_i!(g_i - n_i)!} \tag{A. 1}$$

Thermodynamically, the equilibrium is reached when ω (equivalent to maximizing ln ω) is maximized for changes in n_i (number of electrons), in other words

$$\frac{\delta \ln \omega}{\delta n_i} = 0 \tag{A. 2}$$

For a populated system where n is a large number, Stirling's approximation can be used:

$$\ln n! = n \ln n - n \tag{A. 3}$$

Using this approximation $\ln \omega$ can be written as

$$\ln \omega = \sum_i \ln(\frac{g_i!}{n_i!(g_i - n_i)!})$$

$$= \sum_i \left[g_i \ln g_i - n_i \ln n_i - (g_i - n_i) \ln(g_i - n_i) \right] \quad \text{(A.4)}$$

By applying the maximizing condition of $\ln \omega$ for n_i, it can be written

$$\delta \ln \omega = -\sum_i \left[\ln n_i - \ln(g_i - n_i) \right] \delta n_i = 0 \quad \text{(A. 5)}$$

By assuming that in this isolated volume υ, flow of particle and energy is steady (conservation of energy and particle), conditions below can be written.

$$\delta \sum_i n_i = \sum_i \delta n_i = 0 \quad \text{(A. 6)}$$

$$\delta \sum_i \varepsilon_i n_i = \sum_i \varepsilon_i \delta n_i = 0 \quad \text{(A. 7)}$$

By using Lagrange's undetermined multipliers for equations (A. 5), (A. 6) and (A. 7) the Equation (A.8) is resulted.

$$\sum_i \left(\ln \frac{n_i}{g_i - n_i} + \alpha + \beta \varepsilon_i \right) \delta n_i = 0 \quad \text{(A. 8)}$$

Having the above equation it can be written that:

$$\ln \frac{n_i}{g_i - n_i} + \alpha + \beta \varepsilon_i = 0 \quad \text{(A. 9)}$$

This leads to

$$n_i = \frac{g_i}{e^{\alpha+\beta\varepsilon_i}+1} \qquad \text{(A. 10)}$$

This is the well known Fermi-Dirac distribution.

Now, consider volume υ' which is neighboring υ and interacts with υ by flow of particles and energy. It is assumed that υ and υ' are isolated. As for υ, lets assume υ' has n_i' electrons having energies ε_i' and distributed in g_i' states. The total probability of arrangement of this system (υ') will be

$$\omega = \prod_i \frac{g_i'!}{n_i'!(g_i'-n_i')!} \qquad \text{(A. 11)}$$

Now for the compound system including υ and υ', the total number of probability of arrangements will be

$$\omega = \prod_i \frac{g_i!}{n_i!(g_i-n_i)!}\prod_j \frac{g_j'!}{n_j'!(g_j'-n_j')!} \qquad \text{(A. 12)}$$

For equilibrium condition of this compound system again ω (equivalently $\ln\omega$) should be maximized and since υ and υ' are isolated, the conservation of energy and particle is valid. So:

$$-\delta\ln\omega = -\sum_i \left\{\left[\ln n_i - \ln(g_i-n_i)\right]\delta n_i + \left[\ln n_i' - \ln(g_i'-n_i')\right]\delta n_i'\right\} = 0 \qquad \text{(A. 13)}$$

$$\delta\sum_i (n_i + n_i') = \sum_i (\delta n_i + \delta n_i') = 0 \qquad \text{(A. 14)}$$

$$\delta\sum_i(\varepsilon_i n_i+\varepsilon_i' n_i')=\sum_i(\varepsilon_i\delta n_i+\varepsilon_i'\delta n_i')=0 \tag{A. 15}$$

Again using Lagrange's undetermined multipliers (α, β) one results in:

$$n_i=\frac{g_i}{e^{\alpha+\beta\varepsilon_i}+1} \tag{A. 16}$$

$$n_i'=\frac{g_i'}{e^{\alpha+\beta\varepsilon_i'}+1} \tag{A. 17}$$

It can be seen that each system reaches the Fermi-Dirac equilibrium distribution with the same α and β parameters. By letting both systems exchange energy, the equilibrium distribution for both systems was a Fermi-Dirac distribution with the same β, indicating that β is associated with the temperature. By having both systems exchange particles the same distribution was reached with the same α, indicating that α is associated with the chemical potential.

Defining α and β as:

$$\alpha=-\frac{\zeta}{kT} \tag{A. 18}$$

$$\beta=\frac{1}{kT} \tag{A. 19}$$

where ζ is the chemical potential and k is the Boltzman constant and T is the absolute temperature.

Rewriting equation (A.16) will result in:

$$n_i = \frac{g_i}{e^{\frac{\varepsilon_i - \zeta}{kT}} + 1} \qquad \text{(A. 20)}$$

in this case ζ is the Fermi energy.

This is true for any volume υ of the metal and it tells us that T and ζ is the same everywhere in the metal (in equilibrium condition).

Appendix B

Surface Science Measurement Techniques

In surface science there are many surface measurement techniques. These techniques give thermodynamic, structural, electronic and dynamical information about the character of the surface species. Because of the complexity of chemical bonding effects on silicon surfaces, a combination of measurement techniques are usually used [36].

The list of all techniques employed by the referenced workers in this thesis is available in this appendix.

HREELS **High-Resolution Electron Energy Loss Spectroscopy**

In this technique, by using a monoenergetic electron beam, vibrational modes of the surface species are excited. The spectrum of reflected electron energies, from the surface, shows peaks at loss energies. These peaks are characteristic of the vibrational modes of the species on the surface.

PES **Photoelectron Spectroscopy**

In this technique, using ultraviolet (called UPS) or X-ray (called XPS) radiation the surface atoms are photoionized. By measuring the kinetic energy distribution of the photoelectrons the binding energies of the electronic levels are found. The binding

energies of the electronic levels depend on the chemical environment of the atoms in the surface (the presence of peaks at particular energies, indicates the presence of a specific element in the sample). In addition to this, the intensity of the peaks is related to the concentration of the element within the sampled region [141].

TDS Thermal Desorption Spectroscopy

In this technique, the sample is heated at a controlled rate and the desorbed species from the surface are detected by a mass spectrometer. This technique is also called Temperature-Programmed Desorption (TPD).

AES Auger Electron Spectroscopy

In the Auger process a high energy photon or electron ejects an electron from a core orbital of an atom. An electron from higher a energy state fills the vacancy created and thereby releases sufficient energy to eject a second photoelectron from one of the higher energy orbitals with the excess kinetic energy.

AES is based upon the measurement of the kinetic energies of the emitted electrons. The Auger electrons are emitted at discrete energies that are characteristic of the elements present on the sample surface. When analyzed as a function of energy, the peak positions are used to identify the elements and the chemical states present.

ISS Ion Scattering Spectrometry

In this technique, a monoenergetic beam of ions strikes the sample surface and is scattered back into the vacuum after one or more collisions with target atoms of the top few layers. Measurement of the energy of the backscattered particles can be used to identify the mass of surface atoms [36].